

Measurement of $K^\pm \rightarrow \pi^\pm \gamma\gamma$ Decays

Dissertation
zur Erlangung des Grades
„Doktor der Naturwissenschaften“
am Fachbereich Physik der
Johannes Gutenberg-Universität Mainz

Cristina Morales Morales
geboren in Valencia (Spanien)

Mainz 2008

Datum der mündlichen Prüfung: 21.07.2009

Contents

1	Abstract	1
2	Motivation	3
3	Theoretical Introduction	5
3.1	Standard Model of Particle Physics (SM)	5
3.2	Strong Interaction (QCD)	7
3.2.1	Chiral Perturbation Theory	8
3.3	$K^\pm \rightarrow \pi^\pm \gamma \gamma$ Decays	11
3.3.1	$O(p^4)$ Contributions	12
3.3.2	$O(p^6)$ Contributions	19
3.4	Previous Measurements	22
4	NA48/2 Experiment	23
4.1	Beam Line	23
4.2	Decay Volume	26
4.3	NA48/2 Detector	26
4.3.1	Anti Counters (AKL)	26
4.3.2	Magnetic Spectrometer (DCH)	28
4.3.3	Hodoscope for Charged Particles (HOD)	30
4.3.4	Liquid Krypton Electromagnetic Calorimeter (LKr)	31
4.3.5	Hodoscope for Neutral Particles (NHOD)	34
4.3.6	Hadron Calorimeter (HAC)	35
4.3.7	Muon Veto Counter (MUV)	37
4.4	Beam Monitors	37
4.5	Data Acquisition System	38
4.5.1	Run Control System	38
4.5.2	Subdetector Readout Systems	38
4.5.3	Online PC Farm	39
4.5.4	Central Data Recording (CDR)	39
4.5.5	Level 3 Trigger (L3)	39
4.5.6	Data Processing and Format	40
5	Trigger System	41
5.1	Charged Trigger Subsystem	42
5.1.1	Level 1 Trigger (L1C)	42

5.1.2	Level 1 Trigger Supervisor (L1TS)	43
5.1.3	Level 2 Charged Trigger (L2C or MassBoX)	43
5.2	Neutral Trigger Subsystem	45
5.2.1	Neutral Trigger (L2N)	45
5.3	L2 Trigger Supervisor (L2TS)	47
6	Data Taking in 2003	49
6.1	Level 1 Trigger (L1C)	50
6.2	Neutral Trigger (L2N)	50
6.3	Level 1 Trigger Supervisor (L1TS)	51
6.4	L2 Trigger	51
6.4.1	L2 MFAKE Trigger	52
6.5	Trigger Chain for the Selection of $K^\pm \rightarrow \pi^\pm \gamma \gamma$	55
7	The Monte Carlo Simulation	57
7.1	Simulation of Charged Kaons Spectra	57
7.2	Simulation of Decays	58
7.2.1	Simulation of Phase Space	59
7.2.2	Simulation of Signal and Normalization Channels	59
7.2.3	Simulation of the Background	60
7.3	Parameters of the Simulation	61
7.4	Radiative Corrections	61
8	Selection of Events	63
8.1	Pre-Selection of Events	64
8.1.1	Selection of the Pion Track	64
8.1.2	Selection of Photon Candidates	66
8.1.3	Selection of Pion Shower Clusters	69
8.2	Event Reconstruction	69
8.2.1	Energy Center of Gravity (COG)	69
8.2.2	Decay Vertex Position	70
8.2.3	Invariant Mass of the Di-Photon System	71
8.3	Decay Vertex Region	72
8.4	Background Sources	72
8.4.1	$K^\pm \rightarrow \pi^\pm \pi^0$	72
8.4.2	$K^\pm \rightarrow \pi^\pm \pi^0 \pi^0$	72
8.4.3	$K^\pm \rightarrow \pi^\pm \pi^0 \gamma$	73
8.5	Background Rejection	74
8.6	Corrections	78
8.7	Selection of $K^\pm \rightarrow \pi^\pm \gamma \gamma$ Decays	82
8.8	Selection of $K^\pm \rightarrow \pi^\pm \pi^0$ Decays	83
9	Trigger Efficiency	89

9.1	Measurement of Trigger Efficiencies	89
9.2	Trigger Efficiency of $K^\pm \rightarrow \pi^\pm \gamma \gamma$ Decays	90
9.2.1	NTPEAK Efficiency	90
9.2.2	$\frac{Q1}{10}$ Efficiency Measurement	95
9.2.3	LKrbias Efficiency Measurement	96
9.2.4	(Q1 + Q2) Efficiency	96
9.2.5	MFAKE Trigger Efficiency	97
9.3	Trigger Efficiency of $K^\pm \rightarrow \pi^\pm \pi^0$ Decays	100
9.4	Summary of Efficiencies	101
10	Data and Monte Carlo Comparison	103
10.0.1	$K^\pm \rightarrow \pi^\pm \gamma \gamma$ Decays	104
10.0.2	$K^\pm \rightarrow \pi^\pm \pi^0$ Decays	107
11	Measurement of $\text{BR}(K^\pm \rightarrow \pi^\pm \gamma \gamma, z \geq 0.2)$	111
11.1	Kaon Flux	111
11.2	Background Expectation	113
11.3	Measurement of $\text{BR}(K^\pm \rightarrow \pi^\pm \gamma \gamma, z \geq 0.2)$	116
11.3.1	Signal Acceptance	117
11.3.2	Trigger Efficiencies	118
11.3.3	Background Subtraction	119
11.3.4	Branching Ratio	120
11.4	Analysis of Systematic Uncertainties	120
11.4.1	Systematics from the Selection	120
11.4.2	Systematics from the Efficiency Measurement	124
11.4.3	Systematics from the Flux Measurement	126
11.5	Summary	127
12	Fit to $z = m_{\gamma\gamma}^2/m_K^2$	129
12.1	$O(p^6)$ ChPT Theory	129
12.1.1	Fit	129
12.1.2	Systematic Uncertainty on \hat{c}	132
12.2	$O(p^6)$ ChPT with $\eta - \eta'$ mixing	133
12.2.1	Fit	133
12.3	Determination of $\text{BR}(K^\pm \rightarrow \pi^\pm \gamma \gamma)$	134
13	Conclusions	137
13.1	Summary	137
13.2	Outlook	138
	List of Figures	139
	List of Tables	141

1 Abstract

The goal of this thesis was an experimental test of an effective theory of strong interactions at low energy, called Chiral Perturbation Theory (ChPT). Weak decays of kaon mesons provide such a test. In particular, $K^\pm \rightarrow \pi^\pm \gamma \gamma$ decays are interesting because there is no tree-level $O(p^2)$ contribution in ChPT, and the leading contributions start at $O(p^4)$. At this order, these decays include one undetermined coupling constant, \hat{c} . Both the branching ratio and the spectrum shape of $K^\pm \rightarrow \pi^\pm \gamma \gamma$ decays are sensitive to this parameter. $O(p^6)$ contributions to $K^\pm \rightarrow \pi^\pm \gamma \gamma$ ChPT predict a 30-40% increase in the branching ratio. From the measurement of the branching ratio and spectrum shape of $K^\pm \rightarrow \pi^\pm \gamma \gamma$ decays, it is possible to determine a model dependent value of \hat{c} and also to examine whether the $O(p^6)$ corrections are necessary and enough to explain the rate.

About 40% of the data collected in the year 2003 by the NA48/2 experiment have been analyzed and 908 $K^\pm \rightarrow \pi^\pm \gamma \gamma$ candidates with about 8% background contamination have been selected in the region with $z = m_{\gamma\gamma}^2/m_K^2 \geq 0.2$. Using 5,750,121 selected $K^\pm \rightarrow \pi^\pm \pi^0$ decays as normalization channel, a model independent differential branching ratio of $K^\pm \rightarrow \pi^\pm \gamma \gamma$ has been measured to be:

$$\text{BR}(K^\pm \rightarrow \pi^\pm \gamma \gamma, z \geq 0.2) = (1.018 \pm 0.038_{\text{stat}} \pm 0.039_{\text{syst}} \pm 0.004_{\text{ext}}) \cdot 10^{-6}.$$

From the fit to the $O(p^6)$ ChPT prediction of the measured branching ratio and the shape of the z -spectrum, a value of $\hat{c} = 1.54 \pm 0.15_{\text{stat}} \pm 0.18_{\text{syst}}$ has been extracted. Using the measured \hat{c} value and the $O(p^6)$ ChPT prediction, the branching ratio for $z = m_{\gamma\gamma}^2/m_K^2 < 0.2$ was computed and added to the measured result. The value obtained for the total branching ratio is:

$$\text{BR}(K^\pm \rightarrow \pi^\pm \gamma \gamma) = (1.055 \pm 0.038_{\text{stat}} \pm 0.039_{\text{syst}} \pm 0.004_{\text{ext}} \pm^{+0.003_{\hat{c}}} \mp_{-0.002_{\hat{c}}}) \cdot 10^{-6},$$

where the last error reflects the uncertainty on \hat{c} .

The branching ratio result presented here agrees with previous experimental results, improving the precision of the measurement by at least a factor of five. The precision on the \hat{c} measurement has been improved by approximately a factor of three. A slight disagreement with the $O(p^6)$ ChPT branching ratio prediction as a function of \hat{c} has been observed. This might be due to the possible existence of non-negligible terms not yet included in the theory. Within the scope of this thesis, $\eta - \eta'$ mixing effects in $O(p^4)$ ChPT have also been measured.

2 Motivation

Within the Standard Model (SM) of particle physics, interactions between elementary particles are described by the strong, weak and electromagnetic forces. The established theory of the strong interactions is Quantum Chromodynamics (QCD). Due to its asymptotic-free nature, perturbation theory can be applied at short distances, where the resulting predictions have achieved a remarkable success in explaining phenomena involving large momentum transfers. In the low-energy domain, the growing of the running QCD coupling and the associated confinement of quarks and gluons make it very difficult to perform a thorough analysis of the QCD dynamics in terms of these fundamental degrees of freedom. However, below the resonance region ($E < m_\rho$), the hadronic spectrum only contains an octet of very light pseudoscalar particles (π, K, η), whose interactions can be understood with global symmetry considerations. Chiral Perturbation Theory (ChPT) is an effective field theory which systematically analyzes the low-energy implications of the QCD symmetries, using the octet of pseudoscalar mesons as the asymptotic degrees of freedom of the theory. The information on the heavier degrees of freedom is then contained in the couplings of the resulting low-energy Lagrangian.

Kaon decays are an ideal framework to test ChPT predictions, since in kaon decays the only physical states which appear are pseudoscalar mesons, photons and leptons, with the characteristic momenta involved being small compared to the natural scale (≈ 1 GeV) of chiral symmetry breaking. In particular, rare kaon decays allow to observe deviations from predicted theoretical behaviors. This is especially the case for $K^\pm \rightarrow \pi^\pm \gamma \gamma$ decays, which have been studied in this thesis and allow to test up to higher order corrections of the theory. From the measurement of the branching ratio and spectrum shape of $K^\pm \rightarrow \pi^\pm \gamma \gamma$ decays, it is possible to extract information about the undetermined coupling constant \hat{c} , appearing already at the lowest order of the decay theory, and to determine whether the so far calculated higher order corrections are enough to explain the observed decay rate.

The NA48/2 experiment at CERN took data in the years 2003 and 2004, collecting the highest existing statistics of charged kaon decays. About 40% of the data collected in the year 2003 have been used for this thesis, and a total of 908 $K^\pm \rightarrow \pi^\pm \gamma \gamma$ candidates with about 8% background contamination have been selected in the region with $z = m_{\gamma\gamma}^2/m_K^2 \geq 0.2$; this means about 30 times more statistics than previous experiments. Using these data, a measurement of the branching ratio and a fit to the spectrum shape of the selected $K^\pm \rightarrow \pi^\pm \gamma \gamma$

decays has been possible, providing the most accurate results up to now on these subjects.

This thesis is structured as follows. In Chapter 3, an introduction to the SM, ChPT and, in particular, ChPT for $K^\pm \rightarrow \pi^\pm \gamma \gamma$ decays is presented. Chapters 4, 5 and 6 summarize the detector, trigger and data taking conditions of the NA48/2 experiment in the year 2003. The parameters of the Monte Carlo (MC) simulations used in this thesis are briefly described in Chapter 7. In Chapters 8, 9 and 10, the selection of the $K^\pm \rightarrow \pi^\pm \gamma \gamma$ candidates, the trigger efficiencies for these decays, and the comparison of the selected data with the MC simulation are presented. In Chapter 11, the measurement of the $K^\pm \rightarrow \pi^\pm \gamma \gamma$ model independent differential branching ratio for $z = m_{\gamma\gamma}^2/m_K^2 \geq 0.2$ is explained, together with the systematic uncertainties associated to this measurement. Chapter 12 contains the results of the fit to the spectrum shape of the data using different theoretical approaches, the determination of the \hat{c} parameter, and the total $K^\pm \rightarrow \pi^\pm \gamma \gamma$ branching ratio. Finally, the results and conclusions obtained from this thesis are summarized in Chapter 13.

3 Theoretical Introduction

3.1 Standard Model of Particle Physics (SM)

The Standard Model of particle physics is a theory which describes the strong, weak and electromagnetic forces, as well as the fundamental particles that make up all matter.

There are *four forces* in nature, characterized by very different ranges and strengths as measured at a typical scale of 1 GeV. The strong force has a range of about 10^{-15} m, and is responsible for the nuclear binding. The weak force, responsible among other processes for radioactive decays, has a range of 10^{-17} m, and is about 10^{-5} times weaker than the strong force. The electromagnetic force, which governs much of macroscopic physics, has infinite range, and its strength is determined by the fine structure constant $\alpha \approx 10^{-2}$. The fourth force, gravity, also has infinite range and a coupling constant of about 10^{-38} , too low to be observed in high energy physics experiments. An achievement of the Standard Model was the elaboration of a unified description of the strong, weak and electromagnetic forces in the language of quantum field gauge theories. Furthermore, the Standard Model combines the weak and electromagnetic forces into a single electroweak gauge theory.

The Standard Model contains both fermionic and bosonic **fundamental particles**. Fermions are particles which possess half-integer spin and obey the Pauli exclusion principle. Bosons possess integer spin. All the fundamental particles that compose matter are fermions, while particles which mediate the interactions are bosons. There are 12 different types, or *flavors*, of fermions (and their antiparticles). They are arranged in three families of quarks and leptons (see Tables 3.1 and 3.2) that are identical in every attribute except their masses. Their detectable differences are attributed to the breaking of a symmetry. The first family includes the up (*u*) and down (*d*) quarks which are the constituents of nucleons, pions and other hadrons. It also contains the lepton doublet formed by the electron and the neutrino. The quarks of the other families are constituents of heavier short-lived particles; they and their companion charged leptons rapidly decay via the weak force to the quarks and leptons of the first family. For each quark flavor there are, in addition, three different *colors*.

Spin-1 gauge bosons mediate interactions among fermions. The electromagnetic force is understood as a renormalizable quantum field theory known as **quantum electrodynamics** (QED). In QED, interactions among electrically charged

particles are due to the exchange of quanta of the electromagnetic field called photons (γ).

The strong force, described by **quantum chromodynamics** (QCD), is mediated by the exchange of eight different massless gluons (g) between quarks, that carry a quantum number called color. In contrast to the electrically neutral photon, gluons possess color charge and hence couple one to another. As a consequence, the color force between two colored particles increases in strength with increasing distance. Thus quarks and gluons cannot appear as free particles, but exist only inside composite particles, called hadrons, with no net color charge. This property is also known as *quark confinement*. A consequence derived from the fact that gluons are carriers of color, is that they spread out the effective color charge of a quark. As a result, the more we approach to the quark, the less color we feel. The resulting antiscreening of the quark color is called *asymptotic freedom*. The quark model was proposed by Gell-Mann and Zweig in 1964 [57, 110] to understand the hadronic spectrum, while the gauge theory of strong interactions was developed by Fritzsche, Gell-Mann and Leutwyler [53]. In 1974 Gross, Wilczek and Politzer [69, 70, 96] explained the property of asymptotic freedom.

The **weak force** is associated with the charged W and neutral Z bosons that mediate it. In distinction to γ 's and gluons, W 's couple only to left-handed fermions (with spin oriented opposite to the direction of motion). Since W particles carry electric charge, they must couple to the γ , suggesting a gauge theory that unites the weak and electromagnetic interactions. The unification of the weak and electromagnetic interactions was developed in the 1960s by Glashow, Weinberg and Salam [62, 103, 98].

The grouping of quarks and leptons into pairs of three families suggests that the quarks and leptons of each family are weak isospin doublets. The unification of the weak and electromagnetic interactions in the electroweak interaction is accomplished by combining the SU(2) weak isospin group with the U(1) singlet that represents quantum electrodynamics. The product SU(2) \times U(1) leads to the electroweak theory. Similarly, special unitary groups of dimension three, SU(3), are used to describe the symmetry based on the three quark flavors (as in the quark model and low-energy QCD) as well as on the three colors of the local gauge symmetry of QCD (ruling the strong interaction dynamics). In the language of group theory, the product SU(3) \times SU(2) \times U(1) represents the underlying symmetry of the Standard Model¹, which is equivalent to saying that the Standard Model incorporates the symmetries representing the electroweak theory (SU(2) \times U(1)) and quantum chromodynamics (SU(3)) [54, 68, 92, 42, 93].

¹The SU(2) \times U(1) symmetry is not manifest, since it involves gauge bosons, such as the W^\pm and Z^0 , that have masses of the order of 100 GeV/ c^2 . These bosons obtain their masses from the *Higgs mechanism* in the electroweak symmetry [76, 75].

	Family 1	Family 2	Family 3
	u	c	t
m [GeV/ c^2]	$(1.5 - 3)10^{-3}$	1.25	174.2
q [e]	$2/3$	$2/3$	$2/3$
	d	s	b
m [GeV/ c^2]	$(3 - 7)10^{-3}$	$95 \cdot 10^{-3}$	4.20
q [e]	$-2/3$	$-2/3$	$-2/3$

Table 3.1: Mass (m) and charge (q) of the quarks of the Standard Model. The masses correspond to the approximate rest mass energy of the quarks confined in hadrons [108].

	Family 1	Family 2	Family 3
	e	μ	τ
m [GeV/ c^2]	0.000511	0.106	1.77699
q [e]	-1	-1	-1
	ν_e	ν_μ	ν_τ
m [GeV/ c^2]	$< 2 \cdot 10^{-6}$	$< 0.19 \cdot 10^{-3}$	$< 18.2 \cdot 10^{-3}$
q [e]	0	0	0

Table 3.2: Mass (m) and charge (q) of the leptons of the Standard Model. For the neutrinos, the upper mass limits are given [108].

3.2 Strong Interaction (QCD)

The QCD Lagrangian density for N_f quark flavors can be written like,

$$\mathcal{L}_{QCD} = -\frac{1}{4}G_{\mu\nu}^{(a)}G^{(a)\mu\nu} + i \sum_{q=1}^{N_f} \bar{\Psi}_q^i \gamma^\mu (D_\mu)_{ij} \Psi_q^j - \sum_{q=1}^{N_f} m_q \bar{\Psi}_q^i \Psi_{qi} , \quad (3.2.1)$$

$$G_{\mu\nu}^{(a)} = \partial_\mu A_\nu^a - \partial_\nu A_\mu^a - g_s f_{abc} A_\mu^b A_\nu^c , \quad (3.2.2)$$

$$(D_\nu)_{ij} = \delta_{ij} \partial_\nu + ig_s \sum_a \frac{\lambda_{ij}^a}{2} A_\nu^a , \quad (3.2.3)$$

where g_s is the QCD coupling constant, and the f_{abc} are the structure constants of the SU(3) algebra. The $\Psi_q^i(x)$ are the 4-component Dirac spinors associated with each quark field of color i and flavor q , and the $A_\mu^a(x)$ are the Yang-Mills gluon fields [108]. The fact, that the strong interaction has different strength depending on the energy of the process involved is described in the running coupling constant of QCD, $\alpha_S(Q^2)$

$$\alpha_S(Q^2) = \frac{g_s^2(Q^2)}{4\pi} = \frac{12\pi}{(33 - 2N_f)\log(Q^2/\Lambda^2)} , \quad (3.2.4)$$

where Q^2 is the momentum transferred in the interaction, and Λ is the energy scale at which the effective coupling becomes large. For Q^2 values much larger than Λ^2 , the effective coupling is small (*asymptotic freedom*) and a perturbative description in terms of quarks and gluons interacting weakly is possible. For Q^2 of order Λ^2 , quarks and gluons *confine* themselves into strongly bound clusters (hadrons). The value of Λ , which is of order 1 GeV, cannot be predicted by the theory and needs to be measured in experiments [74].

3.2.1 Chiral Perturbation Theory

As explained above, the high energy regime of QCD is characterized by a small coupling constant which allows a perturbative treatment of the interaction. However, such a perturbative treatment is not possible when describing phenomena of energies of the order of a typical hadronic mass (≈ 1 GeV). Chiral Perturbation Theory is the effective field theory of QCD at low energies².

Chiral Symmetry

Chiral symmetry is a symmetry of the Lagrangian under which the left-handed and right-handed parts of the Dirac fields describing the fermions transform independently. The QCD Lagrangian has a chiral symmetry in the limit that the quark masses vanish³. The QCD Lagrangian density for the light quarks can be written as:

$$\mathcal{L}_{QCD}^0 = -\frac{1}{4}G_{\mu\nu}^{(a)}G^{(a)\mu\nu} + i \sum_{q=1}^{N_f} \bar{\Psi}_q^i \gamma^\mu (D_\mu)_{ij} \Psi_q^j. \quad (3.2.5)$$

Considering the chirality matrix decomposition as a function of the Dirac matrices: $\gamma_5 = \gamma^5 = i\gamma^0\gamma^1\gamma^2\gamma^3$, with $\{\gamma^\mu, \gamma_5\} = 0$ and $\gamma_5^2 = 1$ and introducing the projection operators

$$P_R = \frac{1}{2}(1 + \gamma_5) = P_R^\dagger, \quad P_L = \frac{1}{2}(1 - \gamma_5) = P_L^\dagger, \quad (3.2.6)$$

which act as $P_{R,L}\Psi_q = \Psi_{qR,qL}$ on the Dirac quark fields:

$$\mathcal{L}_{QCD}^0 = -\frac{1}{4}G_{\mu\nu}^{(a)}G^{(a)\mu\nu} + i \sum_{q=1}^{N_f} \bar{\Psi}_{qR}^i \gamma^\mu (D_\mu)_{ij} \Psi_{qR}^j + i \sum_{q=1}^{N_f} \bar{\Psi}_{qL}^i \gamma^\mu (D_\mu)_{ij} \Psi_{qL}^j. \quad (3.2.7)$$

²An effective field theory is an approximation of an underlying more fundamental field theory.

This new theory contains the appropriate degrees of freedom to describe the physical phenomena occurring at a chosen scale length. The substructure and degrees of freedom at shorter distances (high energies) are encoded in the couplings of the effective theory.

³It is conventional to call quarks heavy if $m > 1$ GeV and light if $m < 1$ GeV.

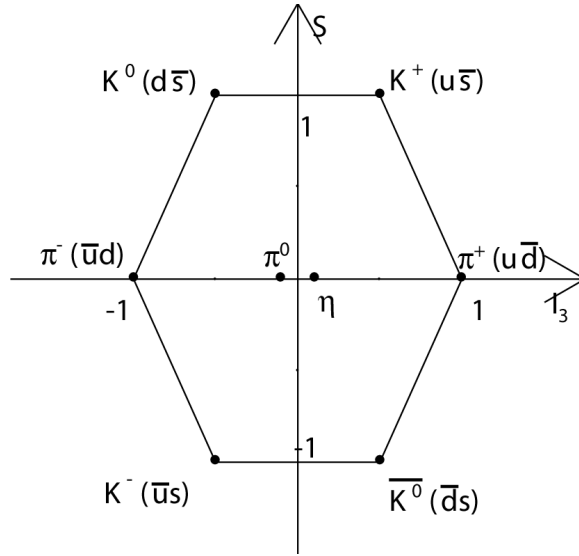


Figure 3.1: SU(3) octet $J^P = 0^-$ of the lightest mesons made of u , d and s quarks. On the horizontal axis units of the third component of isospin are considered, while on the vertical axis units of strangeness are plotted. The Gell-Mann-Nishijima equation for mesons $Q = I_3 + \frac{S}{2}$ relates these quantities with the corresponding meson charge.

This Lagrangian density is left unchanged under rotation of Ψ_{q_L, q_R} by any 3×3 unitary matrix $L(R)$. This property is called flavor symmetry or *chiral symmetry* and denoted as $U(3)_L \times U(3)_R$. The chiral symmetry transformation can then be divided into a component that treats the left-handed and right-handed parts equally (vector symmetry) and a component that treats them differently (axial component) [90]. The symmetry can then be decomposed into: $SU(3)_L \times SU(3)_R \times U(1)_V \times U(1)_A$. The vector symmetry $U(1)_V$ acts as $\Psi_{q_L, q_R} \rightarrow e^{i\theta} \Psi_{q_L, q_R}$ and corresponds to baryon number conservation. The axial symmetry $U(1)_A$ acts as $\Psi_{q_L} \rightarrow e^{i\theta} \Psi_{q_L}$ and $\Psi_{q_R} \rightarrow e^{-i\theta} \Psi_{q_R}$ and is violated⁴ (chiral anomaly). The remaining chiral symmetry $SU(3)_L \times SU(3)_R$ turns out to be spontaneously broken by quark condensate⁵ (the quark bilinear mean value in the vacuum) into the subgroup $SU(3)_V$, known as isospin [99, 43, 95].

Due to the spontaneous breaking of the theory and according to **Goldstone's theorem** [63, 64], a new massless (or light, if the symmetry is not exact) spin zero particle appears for each generator of the symmetry that is broken.

⁴Due to quantum effects, the conservation of the axial vector current in gauge theories is incompatible with gauge invariance (chiral anomaly) [93].

⁵Spontaneous symmetry breaking takes place when a system that is symmetric with respect to some symmetry group goes into some vacuum state which is not symmetric [90].

Goldstone Bosons

Experimentally, it is seen that the masses of the octet of pseudoscalar mesons (Figure 3.1) are very much lighter than the next heavier states. This octet of pseudoscalar mesons is interpreted as the 'would be' *Goldstone bosons* which arise in QCD from the spontaneous breaking of the chiral flavor symmetry into $SU(3)_V$ and can be collected in a unitary matrix field⁶ $U(\varphi)$,

$$U(\varphi) = \exp(i\lambda_a\varphi^a/F_\pi), \quad \frac{1}{\sqrt{2}}\lambda_a\varphi^a = \begin{pmatrix} \frac{\pi^0}{\sqrt{2}} + \frac{\eta}{\sqrt{6}} & \pi^+ & K^+ \\ \pi^- & -\frac{\pi^0}{\sqrt{2}} + \frac{\eta}{\sqrt{6}} & K^0 \\ K^- & K^0 & -\frac{2\eta}{\sqrt{6}} \end{pmatrix},$$

where $F_\pi = 92.4$ MeV is the pion decay constant in the chiral limit and $U(\varphi)$ transforms as $U(\varphi) \rightarrow g_R U(\varphi) g_L^{-1}$, $(g_L, g_R) \in G$ under chiral rotations.

Chiral Lagrangian

The most general chiral Lagrangian density describing the dynamics of the Goldstone bosons [104, 99, 42] is organized as an expansion of terms with an increasing number of derivatives and quark mass terms, $\mathcal{L} = \mathcal{L}_2 + \mathcal{L}_4 + \dots$. An index of 2 denotes either two derivatives or one quark mass term. For a global $SU(3)_L \times SU(3)_R$ symmetry, the most general chiral invariant effective Lagrangian density with the minimal number of derivatives is [99]:

$$\mathcal{L}_{strong} = \frac{F^2}{4} Tr(\partial_\mu U \partial^\mu U^\dagger) = \frac{1}{2} \partial_\mu \varphi^a \partial^\mu \varphi_a + \mathcal{L}_{int}, \quad (3.2.8)$$

with \mathcal{L}_{int} the interaction term generated by higher order terms. In order to incorporate all the interactions happening among the octet fields, one needs to add electroweak, scalar and pseudoscalar interactions [47, 55, 56]. The chiral invariant QCD Lagrangian can then be extended by coupling the meson fields to external hermitian matrix fields v_μ, a_μ, s, p representing the interactions and promoting the global chiral symmetry to a local one [87]. In this way, for the lowest order strong local chiral invariant Lagrangian density we obtain:

$$\mathcal{L}_2 = \frac{F^2}{4} Tr(D_\mu U D^\mu U^\dagger + \chi U^\dagger + \chi^\dagger U), \quad \chi = -2 \frac{\langle \bar{u}u \rangle}{F^2} (s + ip), \quad (3.2.9)$$

where the scalar and pseudoscalar fields s and p give rise to Green functions of (pseudo)scalar quark currents and incorporate explicit chiral symmetry breaking through the quark masses. The specific form of the various terms introduced in Eq. 3.2.9 can be found in [46]. Some of them are of special interest for the theoretical description of $K \rightarrow \pi\gamma\gamma$ decays and will be reproduced in the following sections.

⁶There are different parameterizations of $U(3)$ corresponding to different choices of coordinates of the coset space $SU(3)_L \times SU(3)_R/SU(3)_V$.

3.3 $K^\pm \rightarrow \pi^\pm \gamma \gamma$ Decays

An effective chiral perturbation theory formulation of the Standard Model is an ideal framework to describe Kaon decays, since in Kaon decays the only physical states which appear are pseudoscalar mesons, photons and leptons, and because the characteristic momenta involved are small compared to the natural scale (≈ 1 GeV) of chiral symmetry breaking.

The general form of the $K \rightarrow \pi \gamma \gamma$ amplitude is given by

$$M(K(p) \rightarrow \pi(p') \gamma(q_1, \epsilon_1) \gamma(q_2, \epsilon_2)) = \epsilon_\mu^*(q_1) \epsilon_\nu^*(q_2) M^{\mu\nu}(p, q_1, q_2), \quad (3.3.1)$$

where ϵ_1 and ϵ_2 are the polarization vectors of the photons (γ_1 and γ_2). Gauge invariance restricts the decay amplitude $M^{\mu\nu}$ to consist of four invariant amplitudes A , B , C and D , which are calculated in the framework of Chiral Perturbation Theory [47],

$$\begin{aligned} M^{\mu\nu}(p, q_1, q_2) = & \frac{A(y, z)}{m_K^2} (q_2^\mu q_1^\nu - q_1 \cdot q_2 g^{\mu\nu}) + \\ & \frac{B(y, z)}{m_K^4} (p \cdot q_1 q_2^\mu p^\nu + p \cdot q_2 p^\mu q_1^\nu - p \cdot q_1 p \cdot q_2 g^{\mu\nu} - q_1 \cdot q_2 p^\mu p^\nu) + \\ & \frac{C(y, z)}{m_K^2} (\epsilon^{\mu\nu\rho\sigma} q_{1\rho} q_{2\sigma}) + \\ & \frac{D(y, z)}{m_K^4} \{ \epsilon^{\mu\nu\rho\sigma} (p \cdot q_2 q_{1\rho} + p \cdot q_1 q_{2\rho}) p_\sigma + \\ & (p^\mu \epsilon^{\nu\alpha\beta\gamma} + p^\nu \epsilon^{\mu\alpha\beta\gamma}) p_\alpha q_{1\beta} q_{2\gamma} \}, \end{aligned} \quad (3.3.2)$$

where

$$y = \frac{p \cdot (q_1 - q_2)}{m_K^2}, \quad z = \frac{(q_1 + q_2)^2}{m_K^2}. \quad (3.3.3)$$

The variables y and z are dimensionless, and their allowed regions are

$$0 \leq |y| \leq \frac{1}{2} \lambda^{\frac{1}{2}}(1, r_\pi^2, z), \quad 0 \leq z \leq (1 - r_\pi)^2, \quad (3.3.4)$$

with

$$\lambda(a, b, c) = a^2 + b^2 + c^2 - 2(ab + bc + ca), \quad r_\pi = \frac{m_\pi}{m_K}. \quad (3.3.5)$$

From Eq. 3.3.2, the differential decay rate is expressed as

$$\frac{\partial^2 \Gamma}{\partial y \partial z} = \frac{m_K}{2^9 \pi^3} \left[z^2 (|A + B|^2 + |C|^2) + \left(y^2 - \frac{1}{4} \lambda(1, r_\pi^2, z) \right)^2 \cdot (|B|^2 + |D|^2) \right]. \quad (3.3.6)$$

The amplitudes A and B have opposite parity transformation properties to C and D . In the limit where CP is conserved, only the amplitudes A, B contribute to $K_L^0 \rightarrow \pi^0 \gamma \gamma$, whereas $K_S^0 \rightarrow \pi^0 \gamma \gamma$ involves only the other two amplitudes C, D [45]. Such a distinction does not apply to $K^\pm \rightarrow \pi^\pm \gamma \gamma$. It is a common feature of non-leptonic radiative K decays with at most one pion in the final state that the corresponding amplitudes vanish to the lowest non-trivial order in chiral perturbation theory, i.e. order p^2 . This is obviously the case for K^0 decays because the photon does not couple directly to neutral particles. It is less obvious for $K^\pm \rightarrow \pi^\pm \gamma \gamma$. As emphasized in [45], the vanishing of amplitudes in lowest order in chiral perturbation theory is due to a mismatch between the minimum number of powers of external momenta required by gauge invariance and the powers of momenta that the lowest order effective lagrangian can provide. This means, that the first contributions to the chiral lagrangian appear at $O(p^4)$. One should therefore in general expect a chiral suppression factor of order $m_K^2/16\pi^2 f_\pi^2 \approx 0.18$ for such amplitudes. In the following sections, only the decay $K^\pm \rightarrow \pi^\pm \gamma \gamma$ will be considered [37].

3.3.1 $O(p^4)$ Contributions

To lowest non-trivial order $O(p^4)$ in chiral perturbation theory, only the leading $\Delta I = 1/2$ invariant amplitudes $A(z)$ and $C(z)$ contribute, with no dependency on y [47]. The amplitudes B and D vanish due to the lack of enough powers of momenta in the lagrangian at this order. The differential decay rate can be obtained by integrating Eq. 3.3.6 over y :

$$\frac{d\Gamma}{dz}(K^\pm \rightarrow \pi^\pm \gamma \gamma) = \frac{m_K}{2^9 \pi^3} z^2 \lambda^{\frac{1}{2}}(1, z, r_\pi^2) (|A(z)|^2 + |C(z)|^2). \quad (3.3.7)$$

The amplitude A in equation 3.3.7 contains the *loop diagrams* contributions of this decay at $O(p^4)$ (see Fig. 3.2) and the *tree level counterterms* added to the lagrangian to absorb $O(p^4)$ divergences. The amplitude C contains the effects due to the presence of *poles and tadpoles*. Both contributions are described in the following sections.

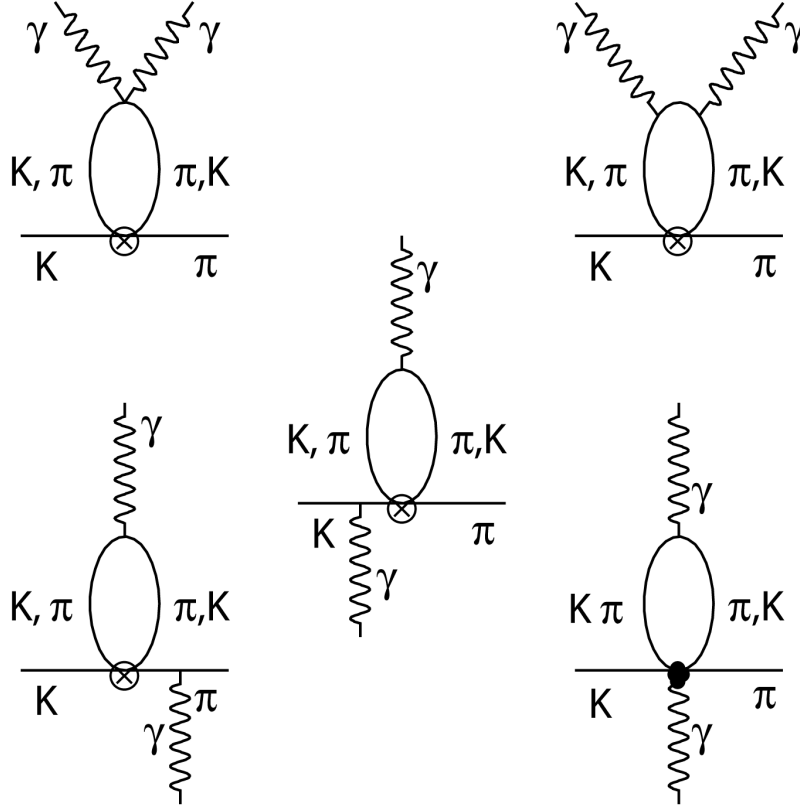


Figure 3.2: Some of the loop diagrams contributing to A in $O(p^4)$. Weak vertices are represented by circles with crosses inside, while the case of electromagnetic and weak vertices together is represented by a full circle.

Loop and Counterterms Amplitude

According to [47, 60], the resulting amplitude A reads:

$$A(z) = \frac{G_8 m_K^2 \alpha_{em}}{2\pi z} \left[(z + 1 - r_\pi^2 + z\delta_{27}^\pi) F\left(\frac{z}{r_\pi^2}\right) + (z + r_\pi^2 - 1 + z\delta_{27}^K) F(z) - \hat{c}z \right], \quad (3.3.8)$$

with

$$\delta_{27}^\pi = \frac{G_{27}}{G_8} \left(\frac{13r_\pi^2}{3z} + \frac{7}{3z} - \frac{13}{3} \right), \quad \delta_{27}^K = \frac{G_{27}}{G_8} \left(\frac{7r_\pi^2}{3z} + \frac{13}{3z} - \frac{13}{3} \right),$$

$$F(x) = \begin{cases} 1 - \frac{4}{x} \arcsin^2\left(\frac{\sqrt{x}}{2}\right), & x \leq 4, \\ 1 + \frac{1}{x} \left(\ln\left(\frac{1-\beta(x)}{1+\beta(x)}\right) + i\pi \right)^2, & x > 4, \end{cases} \quad (3.3.9)$$

$$\beta(x) = \sqrt{1 - \frac{4}{x}}$$

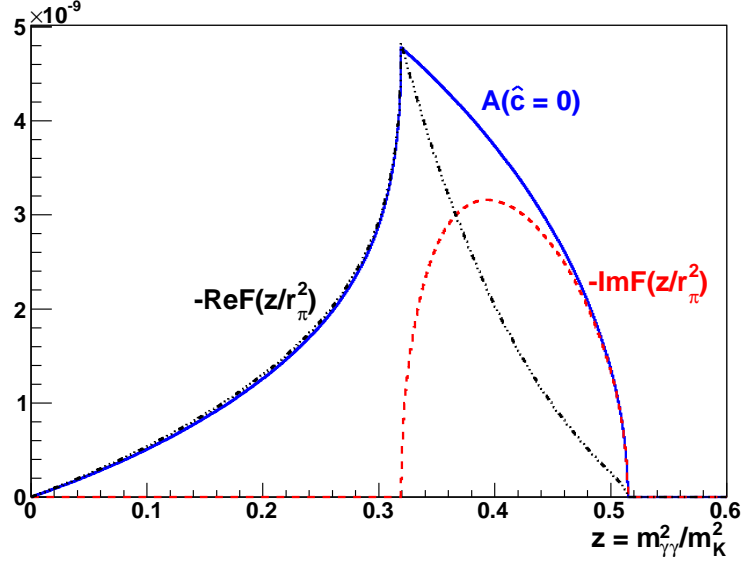


Figure 3.3: Behavior of the imaginary and real parts of the one-loop function $F(z/r_\pi^2)$ in the physical region of $K^\pm \rightarrow \pi^\pm \gamma\gamma$.

and where $|G_8| \approx 9.1 \times 10^{-12} \text{ MeV}^{-2}$ and $|G_{27}| \approx 5.3 \times 10^{-13} \text{ MeV}^{-2}$ are the effective weak-coupling constants⁷ as determined from $K \rightarrow \pi\pi$ decays at $O(p^2)$. The pion loop contribution $(r_\pi^2 - 1 - z)F(z/r_\pi^2)$ dominates over the kaon loop contribution $(1 - z - r_\pi^2)F(z)$. In addition, a cusp effect appears at the $\pi^+\pi^-$ threshold (see Fig. 3.3), when the invariant mass of the two final photons equals two times the mass of the charged pion exchanged in the loop, or equivalently $z = 4m_\pi^2/m_K^2$.

Only the two upper loop diagrams of Figure 3.2 contribute to the absorptive part of the A amplitude since they are the only ones which produce the tensor structures $q_{2\mu}q_{1\nu}$ and $q_1 \cdot q_2 g_{\mu\nu}$ necessary for this amplitude. The loop diagram with the full electroweak vertex gives a divergent constant of dimension mass squared times $g_{\mu\nu}$ which cancels with similar non-gauge invariant pieces from the other diagrams. The two loops with a radiated gamma produce a structure proportional to $p_\mu p'_\nu$ and are canceled by tadpole diagrams not shown in Figure 3.2 [47]. The amplitude A contains one undetermined parameter \hat{c} . This parameter, which must be renormalization scale invariant, is due to local electromagnetic and weak counterterms and reads [60],

⁷ G_8 and G_{27} are the effective realization of the four quark operators which under chiral rotations transform respectively as $(8_L, 1_R)$ and $(27_L, 1_R)$ (chiral representations of the group $SU(3)_L \times SU(3)_R$). The huge ratio of these couplings shows the enhancement of the octet $\Delta I = 1/2$ transitions in the non-leptonic $\Delta S = 1$ interactions.

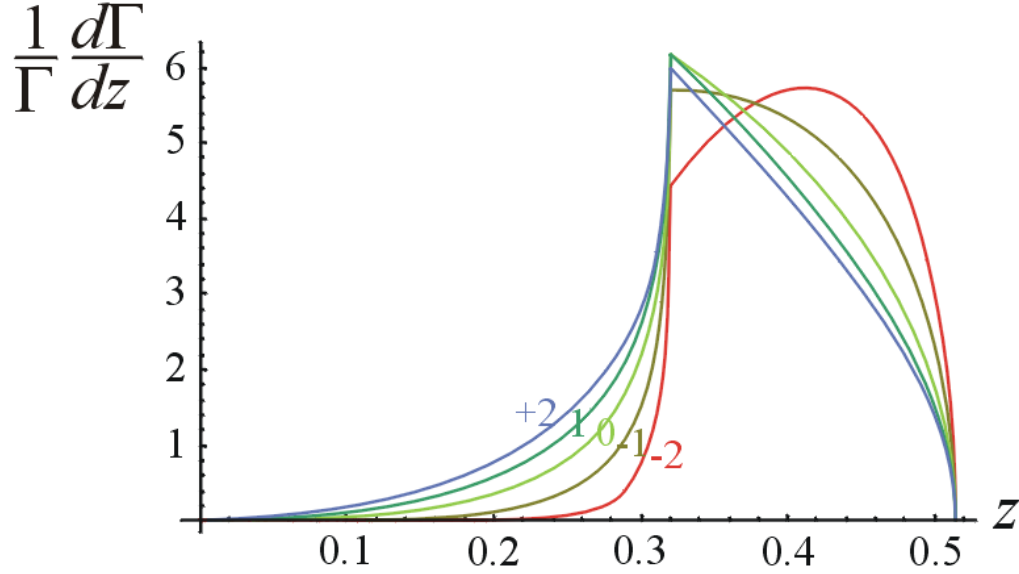


Figure 3.4: $K^\pm \rightarrow \pi^\pm \gamma \gamma$ normalized differential rate for $O(p^4)$ loop contribution as a function of z for different \hat{c} values [59].

$$\hat{c} = \frac{128\pi^2}{3} \left[3(L_9 + L_{10}) + N_{14} - N_{15} - 2N_{18} + \frac{2G_{27}}{3G_8}(3(L_9 + L_{10}) + D_i) \right],$$

where L_i are the local $O(p^4)$ strong couplings [55, 56], N_i are $O(p^4)$ weak couplings from the octet $|\Delta S = 1|$ [44] and D_i are the 27-plet counterterms [80, 49]. The parameter \hat{c} can only be computed in a model-dependent way, being predicted to be of $O(1)$ [48, 30, 26, 44]. Figure 3.4 shows the loop contribution to the $K^\pm \rightarrow \pi^\pm \gamma \gamma$ differential rate for different \hat{c} values.

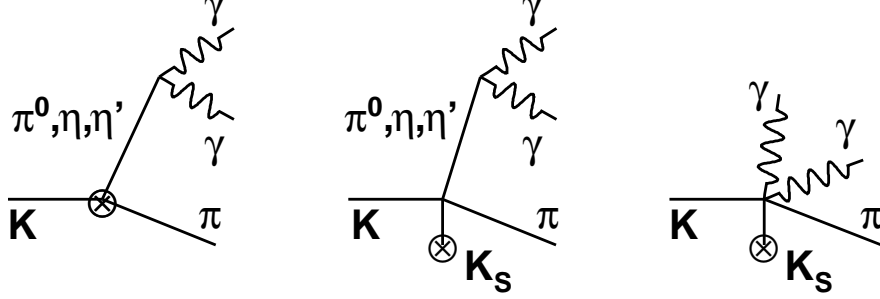
The A amplitude induces the following branching ratio for $z > 0.2$ [47]:

$$BR(K^\pm \rightarrow \pi^\pm \gamma \gamma)_{z>0.2}^{A, O(p^4)} = (5.77 + 1.64 \hat{c} + 0.29 \hat{c}^2) \times 10^{-7}. \quad (3.3.10)$$

Pole Amplitude

The amplitude C can be calculated from the diagrams with anomalies, also called pole and tadpole contributions (Fig 3.5) [105, 106]. There are two different approaches in $K^\pm \rightarrow \pi^\pm \gamma \gamma$ with respect to the importance of the pole contribution.

The **first approach** takes into account only the effects of the octet of pseudoscalar mesons (π^0 and η) in the Wess-Zumino-Term ($(\pi^0, \eta) \rightarrow \gamma \gamma$ through the sequence $K^\pm \rightarrow \pi^\pm(\pi^0, \eta) \rightarrow \pi^\pm \gamma \gamma$) [47]. This approximation provides a pole


 Figure 3.5: Pole and tadpole contributions to the process $K^\pm \rightarrow \pi^\pm \gamma \gamma$.

amplitude equal to:

$$C(z) = \frac{G_8 m_K^2 \alpha_{em}}{\pi} \left[\frac{z - r_\pi^2}{z - r_\pi^2 + i r_\pi \frac{\Gamma_{\pi^0}}{m_K}} - \frac{z - \frac{2+r_\pi^2}{3}}{z - r_\eta^2} \right], \quad (3.3.11)$$

where $r_\eta = m_\eta/m_K$. The first quotient is due to the pion pole⁸ and the second one is due to the η pole. Both terms give a contribution to the total branching ratio of:

$$BR(K^\pm \rightarrow \pi^\pm \gamma \gamma)_{z>0.2}^{Poles, O(p^4)} = 0.51 \times 10^{-7}, \quad (3.3.12)$$

which is much smaller than the contribution due to the loops.

A **second approach** by [60] shows that the G_{27} contribution cannot be neglected. Adding the G_{27} contribution increases the value quoted in Eq. 3.3.12 to:

$$BR(K^\pm \rightarrow \pi^\pm \gamma \gamma)_{z>0.2}^{Poles+G_{27}, O(p^4)} = 1.17 \times 10^{-7}, \quad (3.3.13)$$

In addition, a third weak operator Q_8^s is introduced to take into account the effects of the flavor-singlet meson η' ⁹. The corresponding coupling constant G_8^s is unknown and should be extracted from the experimental data together with \hat{c} . In this approach, the amplitude C is calculated from the anomalous diagrams of Figure 3.5. The leading order computation in U(3) ChPT gives for the C amplitude [60]

$$C(z) = \frac{8}{3(2\pi)} (m_K^2 - m_\pi^2) m_K^2 \alpha_{em} [G_8 C_8(z) + G_8^s C_8^s(z) + G_{27} C_{27}(z)], \quad (3.3.14)$$

⁸Due to the derivative couplings in the chiral vertices, there is a non vanishing contribution when the π^0 is off-shell [99, 100].

⁹In QCD the η' is associated with the axial U(1) which is broken through chiral anomaly and not by spontaneous symmetry breaking.

where the three pole functions C_8 , C_8^s and C_{27} are independent. This amplitude involves virtual $\eta - \eta'$ exchange.

Changing to the $\eta - \eta'$ base, the different coupling constants contributing to $C(z)$ can be written as [60]:

$$\begin{aligned}
 C_8(z) &= \frac{3}{4(m_K^2 - m_\pi^2)} + \frac{2m_K^2 + m_\pi^2 - 3m_K^2 z}{4(m_K^2 - m_\pi^2)} \left(\frac{c_\theta c_\eta}{m_K^2 z - m_\eta^2} + \frac{s_\theta c_{\eta'}}{m_K^2 z - m_{\eta'}^2} \right) - \\
 &\quad \frac{1}{\sqrt{2}} \left(\frac{s_\theta c_\eta}{m_K^2 z - m_\eta^2} - \frac{c_\theta c_{\eta'}}{m_K^2 z - m_{\eta'}^2} \right), \\
 C_8^s(z) &= -\frac{3}{2\sqrt{2}} \left(\frac{s_\theta c_\eta}{m_K^2 z - m_\eta^2} - \frac{c_\theta c_{\eta'}}{m_K^2 z - m_{\eta'}^2} \right), \\
 C_{27}(z) &= \frac{5m_K^2 - 7m_\pi^2 + 2m_K^2 z}{4(m_K^2 - m_\pi^2)(m_K^2 z - m_\pi^2)} + \frac{3m_K^2 - m_\pi^2 - 2m_K^2 z}{4(m_K^2 - m_\pi^2)} \\
 &\quad \left(\frac{c_\theta c_\eta}{m_K^2 z - m_\eta^2} + \frac{s_\theta c_{\eta'}}{m_K^2 z - m_{\eta'}^2} \right),
 \end{aligned} \tag{3.3.15}$$

being $c_\eta = c_\theta - 2\sqrt{2}s_\theta$ and $c_{\eta'} = s_\theta + 2\sqrt{2}c_\theta$ the mixing angle combinations for η and η' , respectively, with $c_\theta \equiv \cos\theta_P$ and $s_\theta \equiv \sin\theta_P$. The $\eta - \eta'$ mixing angle θ_P is an effective angle allowed to vary around -22° ¹⁰. In Equations 3.3.15, the imaginary parts of the poles have been neglected. This assumption is valid as long as the di-photon invariant mass is not close to the pole mass, which is always the case for the η and η' poles and is also valid for the π^0 pole for $z > 0.2$.

Figure 3.6 a), shows the $K^\pm \rightarrow \pi^\pm \gamma \gamma$ normalized differential rate for $O(p^4)$ loop + pole (plain), loop alone (dashed) and pole alone (dotted) contributions as a function of z for $\hat{c} = \pm 2$, $G_8^s/G_8 = +1/3$ and $\theta_P = -20^\circ$. Figure 3.6 b), contains the pole contribution to the rate as a function of G_8^s/G_8 . A positive sign for G_8^s/G_8 could account for an increase of the total rate by more than 20%. For a value of $G_8^s/G_8 \approx -1/3$, the pole contribution is completely suppressed (about 10^{-9}). An upper limit would in this case be:

$$G_8^s/G_8 = -0.38 \pm 0.12 \quad \rightarrow \quad BR(K^\pm \rightarrow \pi^\pm \gamma \gamma)_{z>0.2}^{C,O(p^4)} < 0.3 \times 10^{-7}, \tag{3.3.16}$$

which could go up by almost a factor 2 considering $O(p^6)$ effects [60].

¹⁰Note that while the angle θ_P used here describes the mixing in the SU(3) basis, the angle ϕ used also in the literature describes the same mixing in the quark flavor basis, taking different values than θ_P .

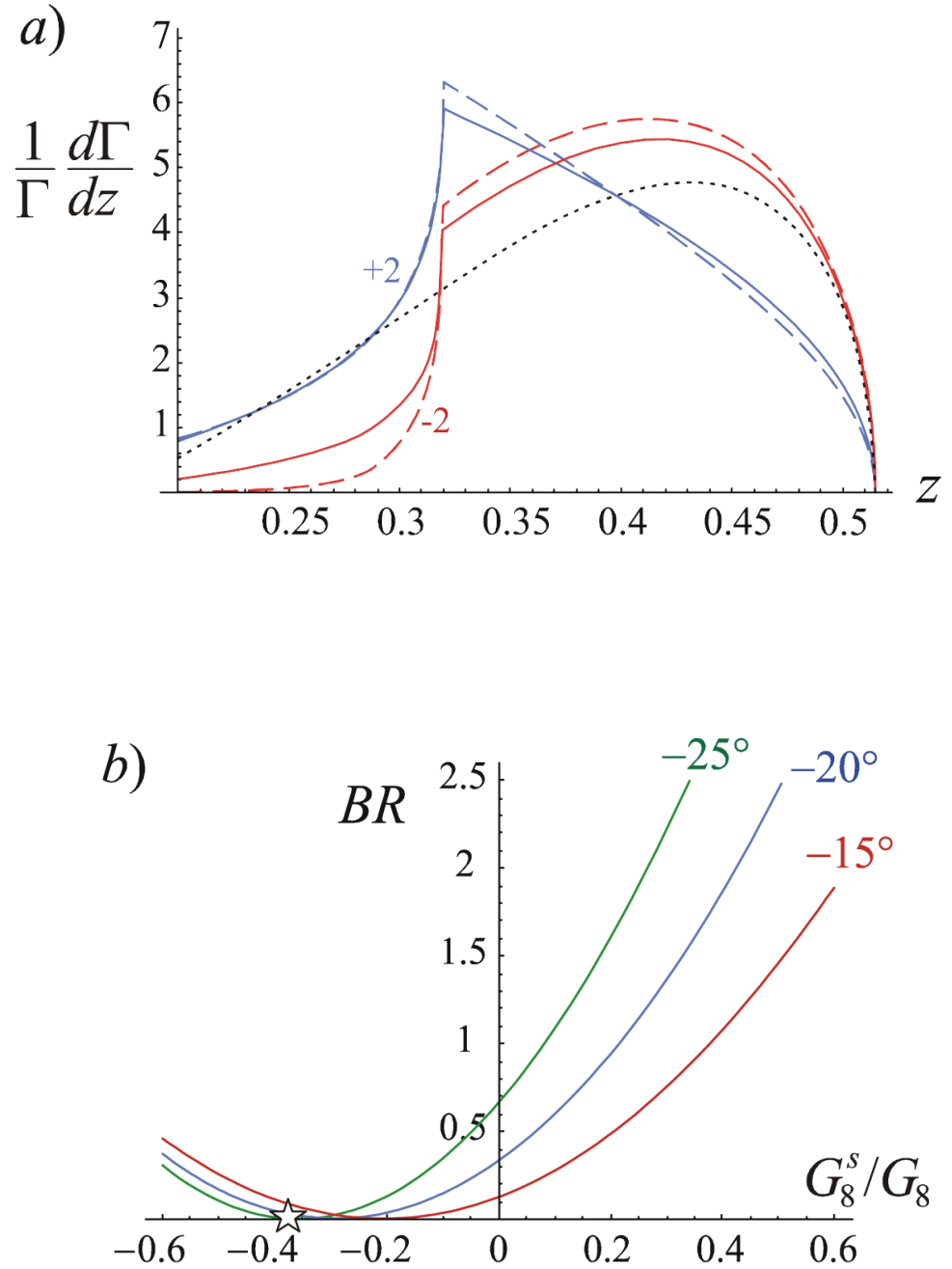


Figure 3.6: Figure a): $K^\pm \rightarrow \pi^\pm \gamma \gamma$ normalized differential rate for $O(p^4)$ loop + pole (plain), loop alone (dashed) and pole alone (dotted) contributions as a function of z for $\hat{c} = \pm 2$, $G_8^s/G_8 = +1/3$ and $\theta_P = -20^\circ$. Figure b): $BR(K^\pm \rightarrow \pi^\pm \gamma \gamma)^{C,O(p^4)} \times 10^7$, as a function of G_8^s/G_8 for $\theta_P = -15^\circ, -20^\circ, -25^\circ$. The star refers to $G_8^s/G_8 = -0.38 \pm 0.12$ [60].

3.3.2 $O(p^6)$ Contributions

The branching ratio for the neutral mode, $K_L \rightarrow \pi^0 \gamma \gamma$, measured in the early 1990s [14, 91], was a factor of two higher than predicted by ChPT, which was confirmed by new measurements by the KTeV and NA48 experiments [1, 86]. This indicated a necessity of next-to-leading order $O(p^6)$ contributions: *unitarity*¹¹ *corrections* obtained from an empirical fit to the decay amplitude of $K_L \rightarrow \pi^+ \pi^- \pi^0$ [34, 27], and *vector meson exchange* contributions. In the case of $K^\pm \rightarrow \pi^\pm \gamma \gamma$ decays, similar corrections are obtained from the $K^\pm \rightarrow \pi^\pm \pi^+ \pi^-$ decay amplitude, while the vector meson contributions are found to be negligible compared to the unitarity corrections [37, 38].

Unitarity Corrections

In the same way as the lowest order decay amplitude of $K^\pm \rightarrow \pi^\pm \pi^+ \pi^-$ generates the $O(p^4)$ loop contribution to $K^\pm \rightarrow \pi^\pm \gamma \gamma$ decays, $K^\pm \rightarrow \pi^\pm \pi^+ \pi^- \rightarrow \pi^\pm \gamma \gamma$, also $O(p^6)$ contributions to $K^\pm \rightarrow \pi^\pm \gamma \gamma$ are induced by $O(p^4)$ corrections to $K^\pm \rightarrow \pi^\pm \pi^+ \pi^-$. Neglecting small phase shifts and up to quartic terms, the isospin decomposition of the decay amplitude of $K^\pm(p) \rightarrow \pi^\pm(p_1) \pi^+(p_2) \pi^-(p_3)$ decays reads [109, 40, 89, 81]

$$\begin{aligned}
 A(K^\pm \rightarrow \pi^\pm \pi^+ \pi^-) &= 2\alpha_1 - \alpha_3 + (\beta_1 - \frac{1}{2}\beta_3 + \sqrt{3}\gamma_3)Y \\
 &\quad - 2(\zeta_1 + \zeta_3)(Y^2 + \frac{1}{3}X^2) - (\xi_1 + \xi_3 - \xi'_3)(Y^2 - \frac{1}{3}X^2) ,
 \end{aligned}
 \tag{3.3.17}$$

where the subscripts 1 and 3 refer to $\Delta I = 1/2, 3/2$ transitions, respectively, and the coefficients are obtained from a fit to the experimental data. The Dalitz variables: $X = \frac{s_2 - s_1}{m_{\pi^+}^2}$, $Y = \frac{s_3 - s_0}{m_{\pi^+}^2}$ are used, with $s_i = (p - p_i)^2$ for $i = 1, 2, 3$ and $s_0 = (s_1 + s_2 + s_3)/3$, where the subscript 3 indicates the odd pion.

The $O(p^6)$ contributions to $K^\pm \rightarrow \pi^\pm \gamma \gamma$ are obtained by considering 3.3.17 as an effective $K^\pm \rightarrow \pi^\pm \pi^+ \pi^-$ vertex, replacing the kinematic variables by covariant derivatives and adding the QED scalar vertices. As a result, the amplitudes A and B are reintroduced, the amplitude C remains unchanged, and D can be neglected compared to B . The following results are obtained [37]:

¹¹Unitarity means that the sum of probabilities of all possible outcomes of an event is always one, which means that all possible intermediate states starting from an initial condition and leading to the same result must be considered. In $K^\pm \rightarrow \pi^\pm \gamma \gamma$ decays, unitarity is obtained perturbatively by considering also two pions intermediate states.

$$\begin{aligned}
 A(z, y) = & \frac{\alpha_{em}}{2\pi} \times \\
 & \left\{ \left[2(2\alpha_1 - \alpha_3) + \left(1 + \frac{1}{3r_\pi^2} - \frac{z}{r_\pi^2} \right) \left(\beta_1 - \frac{1}{2}\beta_3 + \sqrt{3}\gamma_3 \right) \right] \times \right. \\
 & \frac{1}{z} F\left(\frac{z}{r_\pi^2}\right) - \frac{8}{3r_\pi^4} (2\zeta_1 - \xi_1) \times \\
 & \left[r_\pi^2 \left(\ln\left(\frac{m_\pi^2}{\mu^2}\right) - 1 \right) + \frac{1}{18} (1 + 6(r_\pi^2 - z) + 9(r_\pi^2 - z)^2) \frac{1}{z} F\left(\frac{z}{r_\pi^2}\right) \right] - \\
 & \frac{8}{3r_\pi^4} (4\zeta_1 + \xi_1) \left[-\frac{1}{12} (1 + 6r_\pi^2) \ln\left(\frac{m_\pi^2}{\mu^2}\right) + \frac{r_\pi^2}{2} - \right. \\
 & \frac{1}{36} (9r_\pi^2 - 5 - 3(1 + 3r_\pi^2)(r_\pi^2 - z)) \frac{1}{z} F\left(\frac{z}{r_\pi^2}\right) + \\
 & \frac{y^2}{z} \left(\frac{1}{12} + 3R\left(\frac{z}{r_\pi^2}\right) + \frac{1}{2} \left(1 + \frac{2r_\pi^2}{z} \right) F\left(\frac{z}{r_\pi^2}\right) \right) - \frac{(1 - r_\pi^2 + z)^2}{4z} \times \\
 & \left(\frac{1}{12} + R\left(\frac{z}{r_\pi^2}\right) + \frac{1}{2} \left(1 + \frac{2r_\pi^2}{z} \right) F\left(\frac{z}{r_\pi^2}\right) \right) + (1 - r_\pi^2 + z) \times \\
 & \left. \left(\frac{1}{24} + \frac{z}{72r_\pi^2} + \frac{1}{12} \left(1 + \frac{2r_\pi^2}{z} \right) \left(\frac{z}{r_\pi^2} R\left(\frac{z}{r_\pi^2}\right) + 3F\left(\frac{z}{r_\pi^2}\right) \right) \right) - \right. \\
 & z \times \left(\frac{1}{36} - \frac{r_\pi^2}{24z} + \frac{z}{72r_\pi^2} + \frac{1}{12} \left(\frac{z}{r_\pi^2} + 1 - \frac{r_\pi^2}{z} \right) R\left(\frac{z}{r_\pi^2}\right) + \right. \\
 & \left. \frac{r_\pi^2}{2z} \left(1 - \frac{r_\pi^2}{z} \right) F\left(\frac{z}{r_\pi^2}\right) \right) \left. \right] + \\
 & G_8 M_{K^+}^2 \left[(z + r_\pi^2 - 1) \frac{1}{z} F(z) - \hat{c} + 2(r_\pi^2 - z)\eta_1 + 2\eta_2 \right] \left. \right\}
 \end{aligned}$$

and

$$\begin{aligned}
 B(z, y) = & \frac{\alpha_{em}}{\pi} \times \left\{ \frac{1}{3r_\pi^4} (4\zeta_1 + \epsilon_1) \left[-\frac{1}{6} \left(1 + 2\ln\left(\frac{M_{\pi^+}^2}{\mu^2}\right) \right) + \frac{z}{18r_\pi^2} - \right. \right. \\
 & \left. \left. \frac{2r_\pi^2}{z} F\left(\frac{z}{r_\pi^2}\right) + \frac{1}{3} \left(\frac{z}{r_\pi^2} - 10 \right) R\left(\frac{z}{r_\pi^2}\right) \right] + G_8 M_{K^+}^2 \eta_3 \right\}, \quad (3.3.18)
 \end{aligned}$$

with

$$R(x) = \begin{cases} -\frac{1}{6} + \frac{2}{x} - \frac{2}{x} \sqrt{\frac{4}{x} - 1} \cdot \arcsin\left(\frac{\sqrt{x}}{2}\right), & x \leq 4, \\ -\frac{1}{6} + \frac{2}{x} - \frac{\beta(x)}{x} \left(\ln\left(\frac{1-\beta(x)}{1+\beta(x)}\right) + i\pi \right), & x > 4, \end{cases}$$

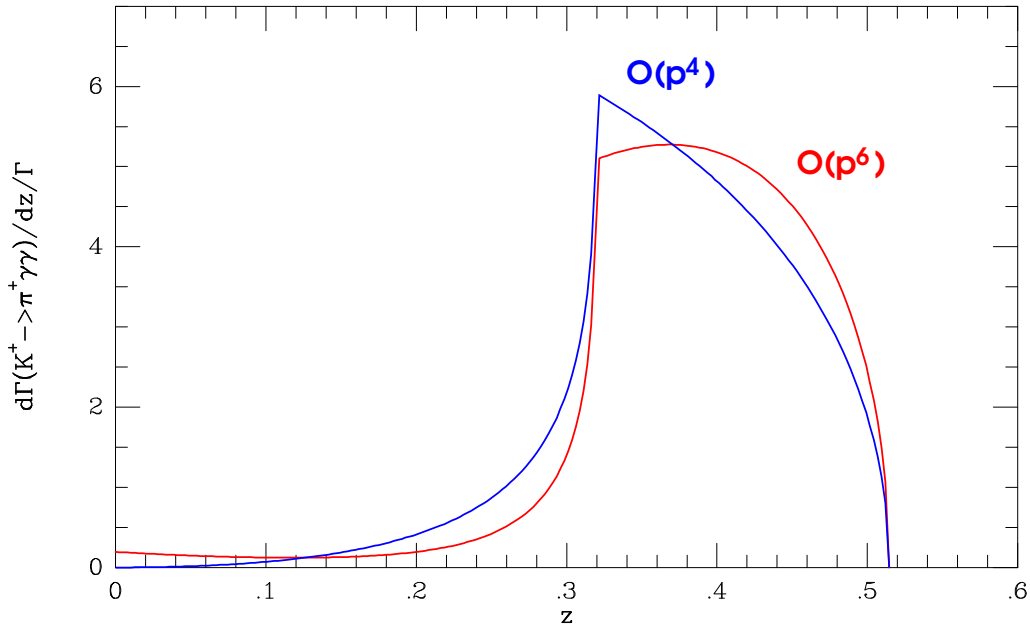


Figure 3.7: Comparison of the normalized $z = m_{\gamma\gamma}^2/m_K^2$ distribution for $K^\pm \rightarrow \pi^\pm \gamma\gamma$ at $O(p^4)$ (blue line) to $O(p^6)$ (red line) [37].

and the functions $F(x)$ and $\beta(x)$ as defined in equation 3.3.9. The counterterms η_i in the previous equations represent the effects of all the resonances and are negligible in comparison with unitarity corrections as computed in [37]. The above results for A , B and C summarized, do not contain the non-negligible G_{27} contributions and G_8^s effects mentioned in Section 3.3.1.

The use of $O(p^6)$ corrections changes both the $m_{\gamma\gamma}$ spectrum and the total branching ratio. A comparison between the $z = m_{\gamma\gamma}^2/m_K^2$ spectrum for $O(p^4)$ and the same spectrum including $O(p^6)$ corrections for $\hat{c} = 0$ can be found in Fig. 3.7. $O(p^6)$ corrections predict a nonzero amplitude at the low kinematic end point. The total branching ratio as a function of \hat{c} is shown in Fig. 3.8. The $O(p^6)$ corrections can increase the branching ratio by up to 30 – 40% compared to $O(p^4)$ for given \hat{c} values. Note that the $O(p^6)$ in the theory has not been fully computed, only the contributions of local $O(p^6)$ amplitudes generated by vector meson exchange and one-loop unitarity corrections from $K^\pm \rightarrow \pi^\pm \pi^\pm \pi^\mp$ decays have been computed to this date [37, 38].

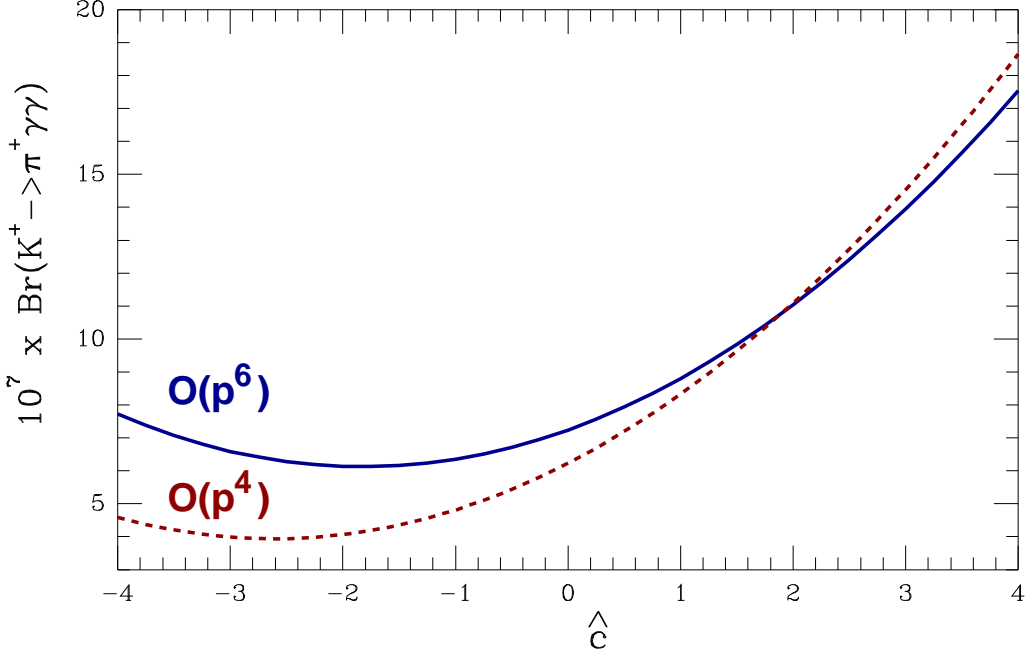


Figure 3.8: $BR(K^\pm \rightarrow \pi^\pm \gamma \gamma)$ as a function of \hat{c} . The dashed line corresponds to $O(p^4)$, and the full line to $O(p^6)$ including unitarity corrections both with $\hat{c} = 0$ [37].

3.4 Previous Measurements

The first observation of the $K^\pm \rightarrow \pi^\pm \gamma \gamma$ decay channel was performed by the E787 experiment at BNL [82]. It was based on 31 event candidates with an estimated background of 5.1 ± 3.3 events, selected in the pion momentum range in the kaon rest frame of $100 \text{ MeV}/c < p_{\pi^\pm}^{CM} < 180 \text{ MeV}/c$, i.e. $0.16 < z = m_{\gamma\gamma}^2/m_K^2 < 0.38$. The corresponding partial branching ratio obtained was $BR(K^\pm \rightarrow \pi^\pm \gamma \gamma, 100 \text{ MeV}/c < p_{\pi^\pm}^{CM} < 180 \text{ MeV}/c) = (6.0 \pm 1.5_{\text{stat}} \pm 0.7_{\text{sys}}) \cdot 10^{-7}$. No $K^\pm \rightarrow \pi^\pm \gamma \gamma$ decay was observed in the π^+ momentum region greater than $215 \text{ MeV}/c$. From the fit to the spectrum shape to ref. [37], a value of $\hat{c} = 1.8 \pm 0.6$ was obtained and the total branching ratio was estimated to be $BR(K^\pm \rightarrow \pi^\pm \gamma \gamma) = (1.10 \pm 0.32) \cdot 10^{-6}$.

The experiment E949 at BNL searched for the $K^\pm \rightarrow \pi^\pm \gamma \gamma$ decay in the kinematic region close to the endpoint. No events were observed and a 90% confidence level upper limit on the partial branching ratio $BR(K^\pm \rightarrow \pi^\pm \gamma \gamma, p_{\pi^\pm}^{CM} > 213 \text{ MeV}/c) < 8.3 \times 10^{-9}$ [9] was obtained using ref. [37].

4 NA48/2 Experiment

The NA48/2 experiment was a collaboration between institutes and universities from Cambridge, CERN, Dubna, Chicago, Edinburgh, Ferrara, Firenze, Mainz, Evanston, Perugia, Pisa, Saclay, Siegen, Torino and Wien. It was the 48th experiment in the North Area of the SPS (Super Proton Synchrotron) at CERN (European Center for Particle Physics) in Geneva.

The NA48 experiment was primarily designed to measure the value of $\frac{\epsilon'}{\epsilon}$, the parameter of direct CP violation, from two-pion decays in simultaneous K_L and K_S beams produced at two different targets. Data for this measurement were taken from 1997 to 2001 and the result of the measurement was $\text{Re}\left(\frac{\epsilon'}{\epsilon}\right) = (14.7 \pm 2.2) \times 10^{-4}$ [19]. The beam configuration was modified in special run periods and in particular in 2002 (NA48/1) in order to measure rare decays of the K_S meson and hyperon decays. During these periods there was only one beam which was produced at the K_S target [17].

The NA48/2 experiment searched for direct CP violation in K^\pm decays to three pions. The experiment used simultaneous K^+ and K^- beams with a momentum of 60 GeV/ c propagating along the same beam line. Data were collected in 2003 and 2004, providing samples of 4×10^9 fully reconstructed $K^\pm \rightarrow \pi^\pm \pi^+ \pi^-$ and 10^8 $K^\pm \rightarrow \pi^\pm \pi^0 \pi^0$ decays [21]. The high statistics study of charged kaon decays with correspondingly high systematic accuracy could also address other questions such as the existence of the postulated quark condensate of the QCD vacuum, the measurement of Chiral Perturbation Theory (ChPT) parameters and the detection of possible deviations from the V-A theory of weak interactions and from Standard Model predictions [18].

4.1 Beam Line

The beam line used in the NA48/2 data taking was specifically designed to transport simultaneously positive and negative particles with a central momentum of 60 GeV/ c [36].

The setup is described in a right-handed orthogonal coordinate system with the z -axis directed downstream along the beam, and the y -axis directed vertically up (see Fig. 4.1). The positive and negative beams were produced with 400 GeV/ c primary protons from the SPS accelerator with a nominal intensity on target of 7×10^{11} protons per 4.8 s duration spill, also called burst, every 16.8 s which impinged on a beryllium target of 40 cm length and 2 mm diameter at zero

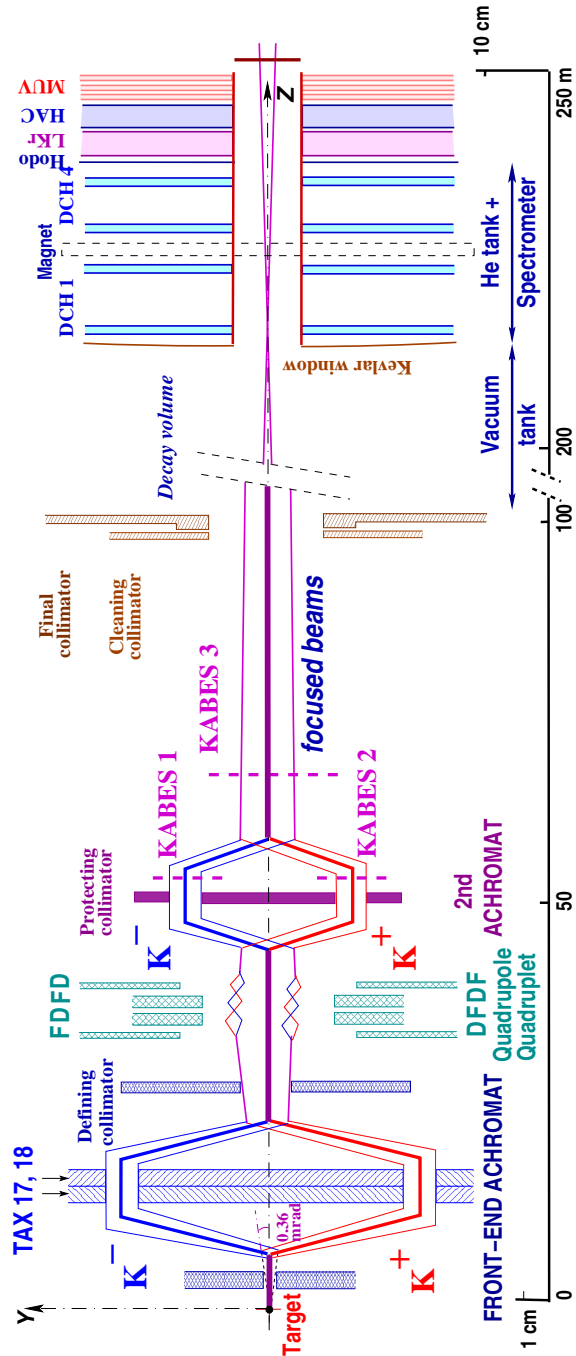


Figure 4.1: Schematic vertical section of the simultaneous K^+ and K^- beam line (not to scale). Outside the dipole magnets the lower and upper envelopes, respectively, of the K^+ and K^- beams are shown. Their axes are steered to coincide to a precision of ≤ 0.3 mm [36].

incidence angle. The angle of incidence of the protons onto the target was selected such that it absorbed large-angle secondary particles.

A central momentum and momentum bite of (60 ± 3) GeV/ c was selected symmetrically for both positively and negatively charged particles by their passage through two vertical deflection magnets with opposite-sign field and a pair of dump collimators with variable but similar openings for each of the two beams. Following these dump collimators, which also served to absorb the remaining primary protons, two further vertical deflection magnets returned the beams onto a common axis. The beams were then again split and recombined in a second achromat. This second achromat was composed of four dipole magnets, incorporated a 'neutron collimator', and was also used as a kaon beam spectrometer (KABES) [94], accommodating position sensitive detectors to determine the momentum of individual beam particles. The KABES spectrometer made use of two stations separated by 8 m along the beam line, each of them measuring the transverse coordinates and the time of the charged tracks. The upstream station, which contained two doublets of detectors, KABES-1 (up) and KABES-2 (down) (see Fig. 4.1), were located at the position where the K^+ and K^- beams were separated and nearly parallel in the achromat and allowed to identify the sign of the charged tracks. The downstream station, KABES-3, used only one doublet of detectors and was positioned where the positive and negative particles were already collinear. This configuration with only two longitudinal positions relied on the focusing properties of the beams to obtain the momentum of individual K^+ and K^- particles from the distance between the vertical coordinates recorded in KABES-1/2 and KABES-3.

The 'neutron collimator' had openings for each of the charged beams and served to block the passage of particles produced on previous collimators. The detectors of the experiment were further protected against background around the beams by a cleaning collimator and a final collimator ending at 102 m from the target.

Just upstream of the last collimator, small steering dipole magnets allowed the two beams to be perfectly aligned in both planes as they entered the decay region pointing towards the detector. The beams were selected with the same geometrical acceptance and directed along a common line. Both beams were focused to similar and small spot sizes (≈ 5 mm r.m.s.) at the spectrometer position, so as to minimize the transverse scale of any structure within the beam spots. Any structure remaining inside the beam spots was naturally exchanged between K^+ and K^- by regular inversions of the achromat polarities. After passing the cleaning and final collimators, the beams entered the decay volume.

During 2003 data taking, the positive beam flux at the exit of the final collimator was estimated to be 3.8×10^7 particles per pulse (of which 2.2×10^7 were K^+). The negative beam flux was 2.6×10^7 ppp (1.3×10^6 K^-).

4.2 Decay Volume

The decay volume of the experiment consisted of a 114 m long cylindrical vacuum tank (10^{-4} mbar of pressure) [18]. This volume was divided into two sections with different diameters. The first section had a diameter of 1.92 m and 39 m of length. The second section had 2.4 m of diameter in order to contain the decay products with larger angles.

The decay region, also called 'blue tube' because its walls were painted in blue, housed a magnetic field composed of the earth magnetic field contribution and a remanent magnetic field. The magnetic field in this tube was called 'blue tube field'. This field was not negligible and needed to be taken into account in the event reconstruction. The effects of this field were mainly important when studying asymmetries in charged kaon decays, since this field could not be reversed like the other fields in the apparatus. The measured field was found to be non-homogeneous in the decay volume, reaching values up to $200 \mu\text{T}$. This non-uniformity could be due to magnetization of the tank itself prior to installation in the NA48 experiment. The measured maps were used at the reconstruction stage and as an input in the Monte Carlo simulations. For a charged particle of $20 \text{ GeV}/c$ momentum crossing the whole length of the vacuum tank along the central axis, the transverse coordinate deflection would be of approx 1.5 mm [66].

The decay volume was terminated by a 0.9 mm thick concave Kevlar window (0.003 interaction lengths) followed by a helium tank at atmospheric pressure containing the magnet spectrometer.

4.3 NA48/2 Detector

The layout of the main components of the detector can be seen in Figure 4.2.

4.3.1 Anti Counters (AKL)

The design of the large-angle anti counters (AKL) was optimized to detect photons outside the electromagnetic calorimeter acceptance [73]. The AKL consisted of scintillation counters of dimension $2000 \times 250 \text{ mm}^2$ arranged in seven pockets of steel placed along the decay tube and the magnet spectrometer. The counters, trapezoidal or rectangular shape, were 10 mm thick NE110 scintillator plates and had 35 mm thick steel plates in front, which acted as photon converters.

Each counter was connected to photomultipliers at its two ends. A mean timer (MT) was implemented at the hardware stage to average the time between the signals at these ends. The digitizations of the MT and of the signal amplitude were done by the pipeline memory board specs (PMB) system [84], also used for other detectors in the experiment.

The AKL time resolution was measured to be $\approx 2 \text{ ns}$ with an efficiency of 97%.

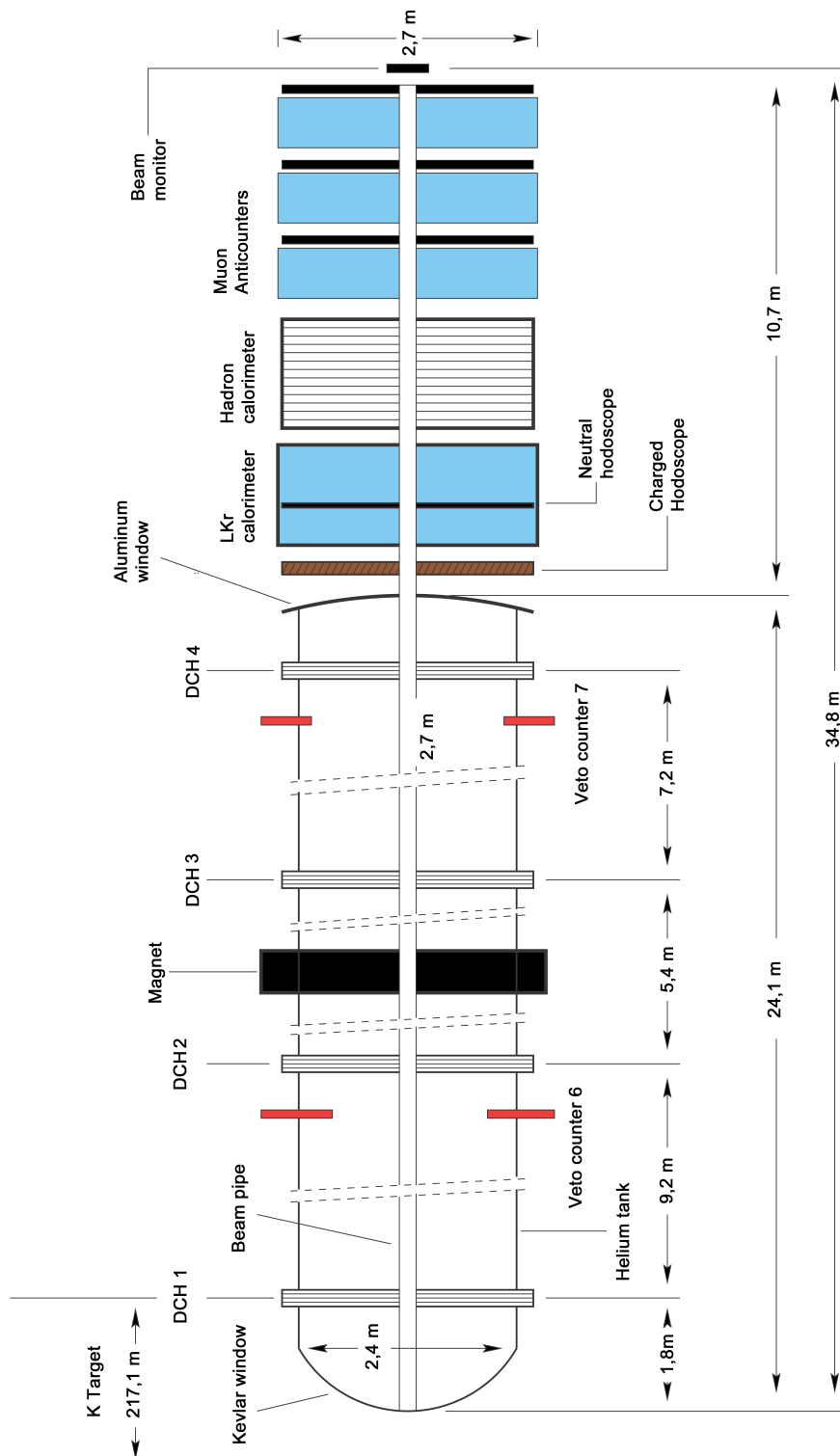


Figure 4.2: Layout of the main detector components of the NA48 detector [85].

4.3.2 Magnetic Spectrometer (DCH)

Momenta and vertex from charged particles from K^\pm decays were reconstructed by a magnetic field spectrometer. The magnetic spectrometer of the NA48/2 experiment consisted of four drift chambers, two upstream and two downstream of a dipole magnet (Figure 4.3) [23, 12].

The value of the magnetic field of the dipole magnet was chosen to optimize the acceptance of the detector and its polarity was regularly alternated. The integral of the magnetic field provided 120 MeV/ c transverse momentum kick.

The drift chambers had an octagonal shape with a transverse width of 2.9 m. Their fiducial area was about 4.5 m². Each chamber contained eight planes of grounded sense wires oriented in four different directions orthogonal to the beam axis: 0° (X, X'), 90° (Y, Y'), -45° (U, U'), 45° (V, V'). Each so defined view contained two staggered planes shifted by half the sense wire pitch to resolve left-right ambiguities and increase the resolution of the reconstructed space points. The maximum drift distance was 5 mm (corresponding to a drift time of 100 ns). The chambers were filled with a mixture of Argon (50%) and Ethane (50%). Sense-wire spacing was 1.0 cm; one wire plane extended over 2.40 m and had 256 sense wires. The drift velocity in the 50/50 mixture of Ar/Ethane was 50 $\mu\text{m}/\text{ns}$. The chambers were normally operated with a gas amplification of 2×10^4 at 2.25 kV between potential and sense wires [12].

The spectrometer was located in a tank filled with helium at atmospheric pressure to minimize the multiple scattering. A 16 cm diameter vacuum tube centered on the beam axis ran the length of the spectrometer through central holes in the Kevlar window, drift chambers and calorimeters.

The momentum resolution of the spectrometer was $\sigma_p/p = 1.02\% \oplus 0.044\% p$ (with p in GeV/ c). The position resolution of the space points was $\leq 100 \mu\text{m}$. The fast rise time of the pulses and the response of the time-to-digital converter were such to allow a time resolution of 0.7ns [20].

Reconstruction of the DCH Information

The reconstruction of the drift chambers information was done in two parts [11, 31]. In the first part, tracks were built without using the drift time information. In the second part drift times were used to refine the tracks.

As a first step, hits in the A and B planes of each view were grouped together to clusters. Two clusters in different plane projections defined a space point. The planes had two hits so that a cluster consisted of 1, 2 or even 3 hit wires. Clusters made of two hits (one on each plane) were called doublets. If the plane was not fully efficient, some doublets could be reconstructed as only singlets (clusters with one hit only). Clusters made of three hits were called triplets. Track segments were formed from the clusters of identical views in chamber one and two. A segment was defined as the projection of a track in one of the views. The angle of one

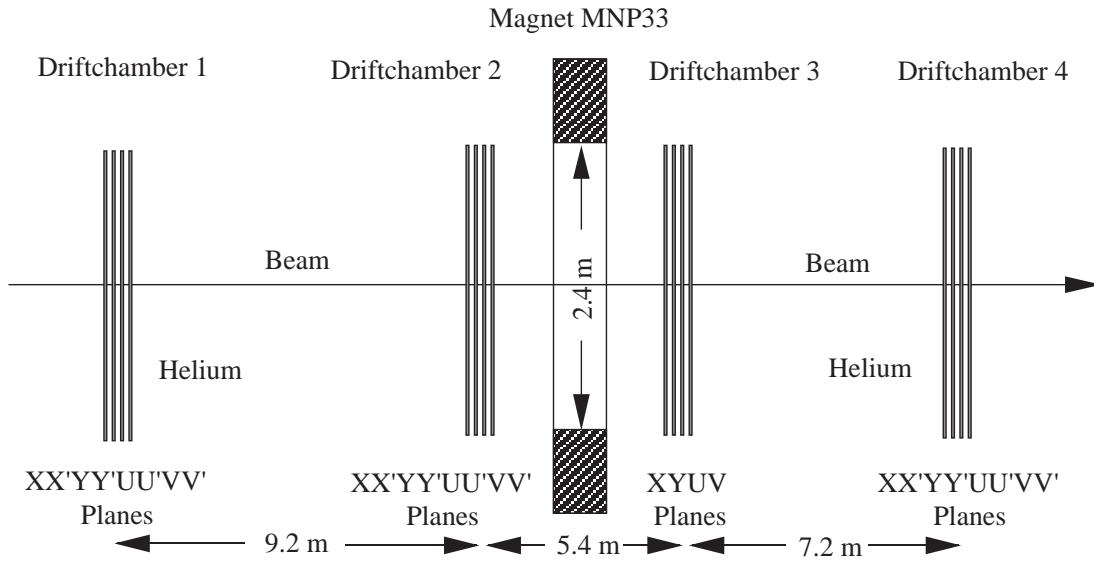


Figure 4.3: The Magnetic Spectrometer [12].

segment with respect to the beam direction had to be smaller than 20 mrad. The four segments of the views together formed one track. In order to reduce the number of tracks, the segments were divided into two groups according to their quality¹. A track was accepted when at least three of the four segments were included in the 'best quality' group (quality close to 1). In addition, the tracks were not allowed to have any space point in common. The accepted tracks were then extrapolated to chamber four. In chamber four space points were built from the clusters. If a space point was found in a certain search region around the extrapolated intersection point of a track with drift chamber number four, this point was associated to the track. The search region condition was equivalent to a requirement on the bending angle of the track.

In the second part, the drift time information was used to increase the accuracy of the track information. The intersection points were then exactly resolved and formed mini-tracks. The mini-tracks were selected with a χ^2 test (the mini-tracks from the first two drift chambers were combined in drift chamber number four with the new space points, the 'real' tracks were then obtained by means of χ^2 tests). For each of the selected tracks the time information was stored. A track was rejected if the hits drift times were too far from each other, or if the coordinates of the hits in a cluster were not compatible anymore after correcting the position for the drift time.

The track momentum and the sign of the charge were determined using the

¹The quality variable was defined as the number of hits belonging to doublets and triplets divided by the total number of hits belonging to the track.

measured space points and the integral of the magnetic field along the track. A map of the magnetic field was determined using a Hall probe.

The magnitude of the momentum of a charged particle was evaluated by considering the deviation of the track due to the magnetic field with the following parametrization:

$$\begin{aligned}x &= x(0) + \frac{dx}{dz}(z - z(0)) + \frac{C_x}{p}, \\y &= y(0) + \frac{dy}{dz}(z - z(0)) + \frac{C_y}{p},\end{aligned}\tag{4.3.1}$$

with C_x and C_y the integrated magnetic field components between z_0 and z in the y - and x -direction, p the momentum, and x and y the space coordinates for a given z . The space components of the momentum are then:

$$p_x = \frac{dx}{dz} \cdot p \cdot N; \quad p_y = \frac{dy}{dz} \cdot p \cdot N; \quad p_z = p \cdot N;\tag{4.3.2}$$

with $\frac{dx}{dz}$ and $\frac{dy}{dz}$ the slopes of the track in the x - and y -direction before passing through the magnet and N the z -component of the normal vector in the z -direction,

$$N = \frac{1}{\sqrt{(dx/dz)^2 + (dy/dz)^2 + 1}}.\tag{4.3.3}$$

4.3.3 Hodoscope for Charged Particles (HOD)

A hodoscope for charged particles was used to measure the event time of charged decay products and to generate a fast trigger signal. The hodoscope was built of vertical and horizontal planes which were located between $z = 119.5$ m and $z = 120.3$ m. Each plane was divided into four quadrants with 16 plastic scintillators each of which was read out by photo-multipliers (see Fig. 4.4). The thickness of the scintillators was 2 cm and the width varied from 6.5 cm in the region close to the beam pipe to 9.9 cm in the outer part. The radius of the central hole crossed by the beam pipe was 12.8 cm. The total amount of detector material along the beam direction was $\approx 0.1 X_0$. Used for trigger purposes, the hodoscope allowed to get fast information about the number of charged decay products and the topology of the event according to the quadrants which were hit by the tracks [29]. In the 2003 data taking period, trigger inefficiencies due to the hodoscope were measured to be below 10^{-4} and the time resolution after the offline reconstruction was about 250 ps.

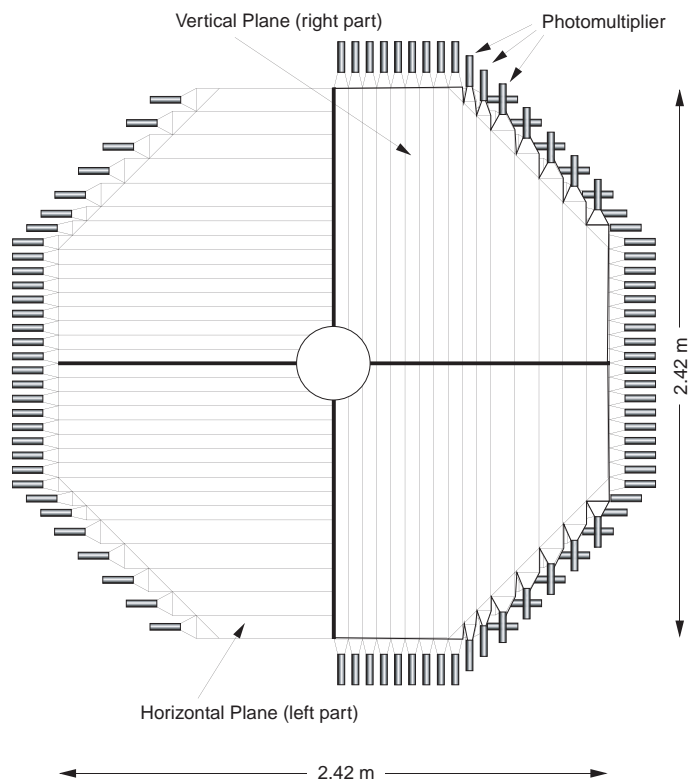


Figure 4.4: View of the two planes of the hodoscope for charged particles [71].

4.3.4 Liquid Krypton Electromagnetic Calorimeter (LKr)

The electromagnetic calorimeter was an almost homogeneous ionization chamber with an active volume of about 10 m^3 of liquid krypton. Liquid krypton has a Molière radius of 4.7 cm and a radiation length X_0 of 4.76 cm. The calorimeter had an octagonal shape with the radius of the inscribed circle being 125 cm. It was segmented transversely into 13248 cells with a cross section of $2 \times 2 \text{ cm}^2$ and a length of 127 cm, which corresponded to $27 X_0$. A 2 mm gap separated vertically two cells. A section of a quadrant of the calorimeter is shown in Figure 4.5.

Each cell consisted of three Cu-Be ribbons, two cathodes and one anode, which were guided by five spacer plates and the back and the front plates (see Fig. 4.6), and were set in zig-zag with an angle of 48 mrad, running almost parallel to the beam. This configuration allowed to reduce non-uniformities coming from the relative position of the shower within the cell, minimizing the region where the shower core could cross the anode. The central anode was kept at high voltage while the cathodes on either side were grounded, forming a drift gap of approximately 1 cm. The cathodes were shared between horizontally adjacent cells. The electrode structure was housed in a vacuum insulated cryostat. The gap stability between cells was enforced by 5 spacer planes spaced every 20.8 cm

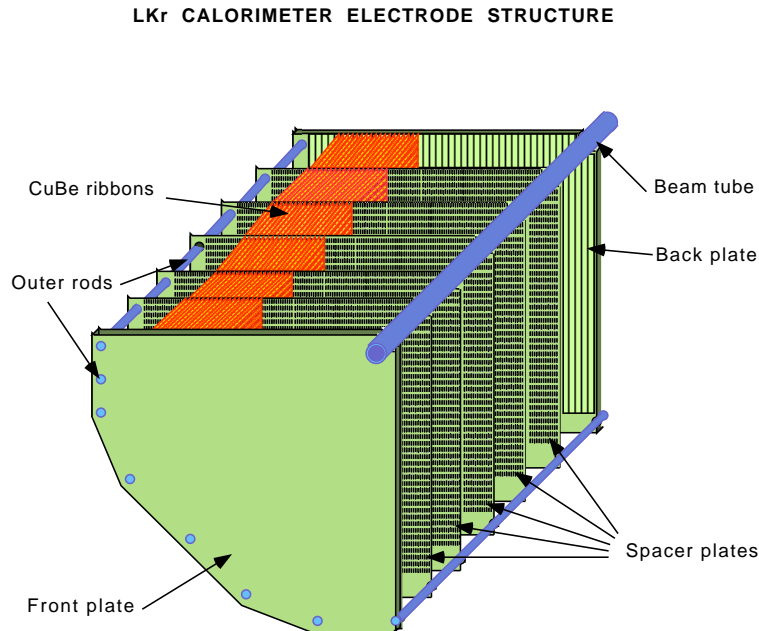


Figure 4.5: Quarter of the electromagnetic calorimeter with 5 spacer plates. The total active front surface extends from the beam pipe to an octagonal outer boundary with an inscribed circle of 128 cm radius [35].

longitudinally. The read-out cells were arranged in a tower geometry [16].

The total number of free electrons resulting from the development of a shower fully contained in the liquid krypton provided a direct measure of the energy of the incoming photon or electron. The lateral distribution of the electro-magnetic showers was strongly peaked transversely to the direction of the photon or electron and up to about 40% of its total energy was deposited in a single cell. The calorimeter had an energy resolution $\sigma_E/E = 0.032/\sqrt{E} \oplus 0.09/E \oplus 0.0042$ (E in GeV). The space resolution for a single electromagnetic shower was $\sigma_x = \sigma_y = 0.42/\sqrt{E} \oplus 0.06$ cm for each transverse coordinate x , y . The time resolution was better than 300 ps at an energy of 50 GeV [78, 20].

Reconstruction of the LKr Electromagnetic Calorimeter Information

The first step of the LKr calorimeter reconstruction was to convert the ADC counts into energy for each cell. The pedestals were continuously monitored by special triggers and were subtracted at the end of each burst. The conversion factor (energy scale) was obtained from the electronic calibration. After this, the reconstruction process followed several steps [101, 102]:

- All cells above an energy threshold of 100 MeV were treated as possible cluster candidates (seed cells).

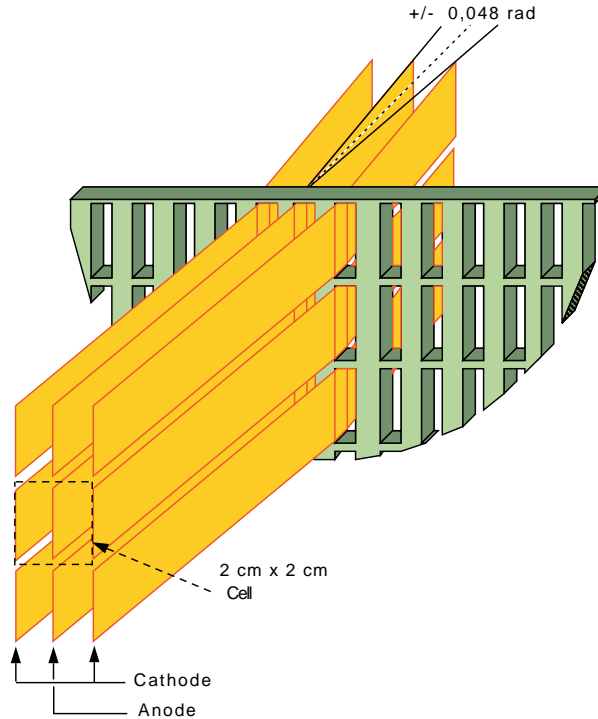


Figure 4.6: Cell structure of the electromagnetic calorimeter [35].

- The cells surrounding the seed cells were read. A cluster was defined once the energy of a seed cell was bigger than the energy seen in the surrounding 8 cells. In addition the energy was compared to the average energy of the surrounding cells and it had to be bigger than this average energy: $E_{seed} > \sum E_{neighbors}$ and $E_{seed} > 1.8 \cdot \overline{E}_{neighbors}$. In case a dead cell was found within the group of cells under study then the neighbors of the dead cell were used to get a reasonable average value for the dead cell.
- Once a cluster was found, its position, time and energy were measured to first order: the position was given by the center of energy of a 3×3 cell box with the seed cell in its center (in case a dead cell was involved 5×5 cells were used instead). The center cell gave a first approximation for the energy and the time of the cluster.
- Afterwards it was checked whether a cell really belonged to a cluster. Two requirements needed to be fulfilled:

- The energy measured by the cell had to belong to the same time window as the cluster: $|t_{cell} - t_{cluster}| < 20$ ns.
- The distance of the cell to the center of the cluster had to be less than 11 cm.
- To be able to deal with overlapping clusters created by particles that hit the detector very close to each other, the energy of all cells had to be distributed between the different clusters found for the event.
 - If a cell belonged only to one cluster (its distance to all other clusters in this event had to be bigger than 11 cm), its energy was added directly to the cluster energy.
 - If the cell belonged to two or more clusters, its energy was distributed among the clusters depending on its distance to each of them, their energy and some expected shower profile (GEANT).
- Afterwards, the total energy of the cluster was calculated by summing up the energy of all corresponding cells. Also the position (x and y) was recalculated using the center of energy. In addition energy corrections due to variations of the electric field were applied.
- The shower width (RMS) was then calculated:

$$RMS_x = \sqrt{\frac{\sum_C (x_C - x_S)^2 E_C}{\sum_C E_C} - \left(\frac{\sum_C (x_C - x_S) E_C}{\sum_C E_C} \right)^2}, \quad (4.3.4)$$

with C the cell index and S the index of the seed cell. A similar expression was used for the y -direction.

- Finally the position of the cluster was corrected in x and y ². The correction of the impact point then lead to a correction in the shower width.

4.3.5 Hodoscope for Neutral Particles (NHOD)

The hodoscope for neutral particles consisted of a plane of scintillating fibers (see Figure 4.7) installed in the liquid krypton calorimeter at a depth of $9.5 X_0$. At this position, the electromagnetic shower was expected to have its maximum for the average energies of the former NA48 experiment.

The hodoscope was divided into 4 quadrants. Each quadrant had 8 read-out channels for a total of 32 channels. The four channels closest to the beam pipe of each quadrant were 10 cm wide and the remaining four 22 cm. Each

²The formula for the x -correction is quite complicated since it has to deal with the zig zag structure of the electrodes and with correction parameters measured in electron runs.

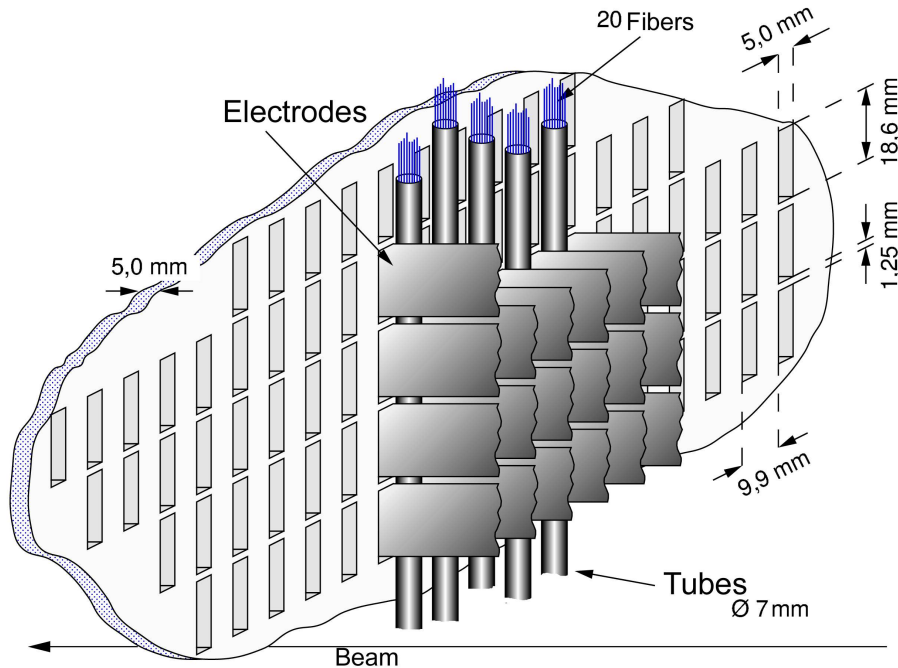


Figure 4.7: Setup of the fiber-bundles at the first spacer plate in the LKr [72].

channel collected signals from bundles of scintillating fibers. The hodoscope was positioned at the second spacer plate of the calorimeter; the bundles (5.5 cm diameter, ≈ 20 fibers per bundle) were inserted in fiberglass tubes, with inner and outer diameter being 7 and 8 mm respectively, that were fixed to the spacer plate, between planes of ribbons. Fiber bundles were then grouped together and sent to photomultipliers located on the calorimeters front plate, inside the liquid krypton, but outside of its active volume [79].

The read-out was based on the PMB system [84]. The detector provided a fast time measurement independent from the time obtained by the calorimeter for events containing electromagnetic showers in the final state. The signal, called T0N, was then sent to a pre-trigger system and was a loose coincidence between opposite halves of the NHOD. The event time resolution from the NHOD was of the order of 260 ps. An efficiency of 95% was reached for energies above 25 GeV and 99% above 35 GeV [88].

4.3.6 Hadron Calorimeter (HAC)

The Hadron Calorimeter (HAC) was used to measure the energies and positions of particles showering in its material. The HAC was mainly used as a trigger device. It provided energy sums which were used in the fast pre-trigger and as a veto in the trigger for neutral particles.

The HAC consisted of an iron-scintillator sandwich of 1.2 m total iron thickness

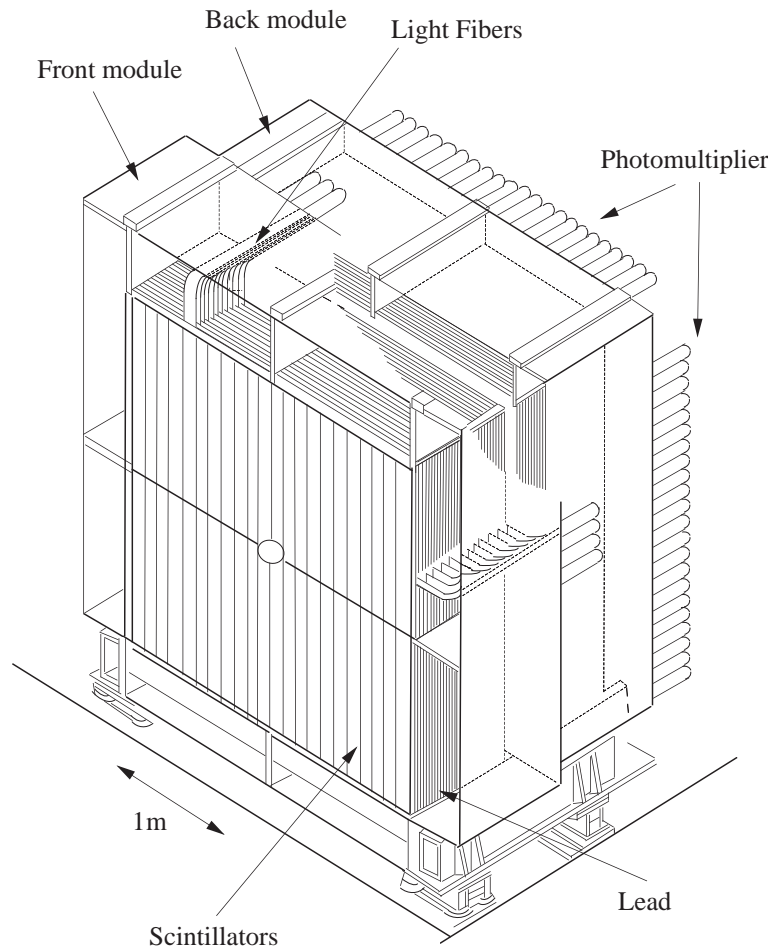


Figure 4.8: The Hadron Calorimeter [50].

(6.7 nuclear interaction lengths). It was divided longitudinally into two separate modules (front and back), each consisting of 24 iron plates, 25 mm thick, of dimensions $2.7 \times 2.7 \text{ m}^2$ (see Figure 4.8). Each scintillator plane inserted between the steel plates consisted of 44 strips. Each strip spanned only half of the calorimeter so that each plane was comprised of two half planes. Around the beam hole the two central strips of each half-plane were 108 mm wide and 1142 mm long. In the back module the two outer strips in each half-plane were 1150 mm long and 108 mm wide. All other strips were 1300 mm long and 119 mm wide. The thickness of each scintillator was 4.5 mm. There were 24 planes in the front module and 25 in the back. In consecutive planes the planes were alternately aligned in the horizontal and vertical directions. In each module the strips with the same longitudinal position were coupled to the same photomultiplier using a light guide. In total there were 176 channels, 88 for each module.

The 176 channels were split in four groups of 44 channels. Each group was connected to one calorimeter pipelined digitizer (CPD) specially made for the

readout of the electromagnetic calorimeter. To be able to use the same unmodified CPDs the photomultiplier signals had to be shaped in order to get a signal form which was comparable to the electromagnetic calorimeter's signals. Therefore, each photomultiplier pulse with a rise-time of ≈ 10 ns and a fall-time of ≈ 50 ns was modified to obtain a signal with a rise-time of ≈ 50 ns and a fall-time of ≈ 2.5 μ s. These signals were shaped again and digitized in the CPDs.

During a test beam in 1995, the energy resolution was determined to be $\frac{\sigma(E)}{E} = \frac{0.69}{\sqrt{E}}$ for hadronic showers, and $\frac{\sigma(E)}{E} = \frac{0.23}{\sqrt{E}}$ for electromagnetic showers.

4.3.7 Muon Veto Counter (MUV)

The muon veto subdetector consisted of three planes of plastic scintillators [24]. The first two were 10 mm thick and the third one 6 mm. These planes were separated from each other by 0.8 m of iron, which was sufficient to stop all particles except for muons from penetrating and triggering the detector. The first plane consisted of eleven horizontal strips, the second one had eleven vertical strips. The strips overlapped by 3 mm on average to ensure full efficiency over the whole area of 2.7 m \times 2.7 m. Light guides and photomultiplier tubes were attached to each of the strips for readout.

The half-strips had only one photomultiplier per strip. In the principal planes an arrangement consisting of an 11 \times 11 matrix of approximately 25 cm \times 25 cm coincidence boxes, builds hits in which produce a trigger. The third plane was also horizontal. It consisted of 6 wider strips giving approximately the same overall area of 2.7 m \times 2.7 m and was used mainly for efficiency calculations of the principal planes.

4.4 Beam Monitors

Two beam monitors were used during the NA48/2 data taking. A beam intensity monitor was used to measure beam profiles right before the beam dump and to generate a trigger of uncorrelated events. It was made of a matrix of scintillating fibers with an active area of 1.8 \times 1.8 cm² read out by 16 photomultipliers. A newer beam monitor consisted of two 8 \times 8 matrices of scintillators, each 6 \times 6 mm² in the transverse direction and 9 mm thick for a total area of $\approx 50 \times 50$ mm², wide enough to fully contain the beams (radial r.m.s. ≈ 6 mm at the end of the experiment). The scintillator blocks were separated by aluminium foils in order to keep the optical cross talk to a minimum level. The two matrices were placed with their centers about 8 mm apart, corresponding to the separation of the two beams at the end of the beam line. The beam monitors served to detect displacements of the beams within the burst and to check the profiles of the beams online and provide feedback for their steering.

4.5 Data Acquisition System

The NA48 data acquisition (DAQ) system was organized as a series of data-push links connected to a PC farm which merged event fragments from the various subdetectors into complete events. To transmit data, a switched Fast Ethernet Network was used. In the farm, data were then stored on local disks. From there they were transferred to the CERN computer center. The third-level filtering, tape recording and online reconstruction were then performed.

4.5.1 Run Control System

The Run Control system controlled the subdetectors and grouped the data into periods of data taking under constant physical conditions, the so-called 'runs'. An online data base managed the subdetector and trigger configurations and kept track of which configuration was used for which time periods. Data were also collected from the beam instrumentation, summary scalers and equipment that did not participate in the data flow and sent along with the burst data.

The Run Control system viewed the experiment as a set of finite state machines which were controlled by the run control program (RCP). The participating computers communicated via the Control Host message passing package. For each state transition the RCP sent the respective command to all subscribed single board computers (SBC) of the different subdetectors. On these computers a standardized 'harness' program interpreted the commands and steered the readout systems correspondingly to the required transitions. The user tasks reported success or failure to the harness via an exit code which was then forwarded to the RCP. The RCP considered a state transition as globally successful when subscribed systems had reported successful completion.

4.5.2 Subdetector Readout Systems

Each subdetector readout system contained a volatile memory (ring buffer) which was able to store the digitized information for all channels for a duration of 200 μ s before it was overwritten. To reduce the data rate the different systems performed a data reduction by doing a zero suppression (e.g. channels without activity were not transmitted).

After some upgrades during the run time of NA48, the readouts of the subdetectors were able to stand a trigger rate of about 15 kHz. Each readout was driven by a Read Out Controller (ROC) which received the triggers (including a time stamp) from the trigger supervisor (see Section 5.1.2). According to the time stamp, the address in the ring buffer was calculated and the corresponding data were sent to a connected subdetector PC which collected all data during the in burst period. The whole systems were steered by the previously mentioned single board computers (SBC) responsible for the slow control.

4.5.3 Online PC Farm

During the inter-burst period, the data of each subdetector PC were moved to the Event Builder PCs [107] (EB). In the EB PCs, all the events were grouped together detector by detector. Events were completely assembled and then written out to local disks, managing a continuous data flow. From the disks these data were transferred to the CERN computer center through 4 additional PCs acting as routers which connected the experimental area via a GBit Ethernet Link with the computer center. As soon as a burst fragment (burstlet) was successfully transferred, it was deleted from the EBPC disk buffer.

4.5.4 Central Data Recording (CDR)

The CDR (Central Data Recording) system at the CERN computing center checked that all the 8 burstlets were transferred, put them together in a complete burst and filled a database of the stored bursts. When a new burst was inserted into the database, it was also added to the list of bursts to be processed by the level 3 software trigger, and fed to the online reconstruction program. Raw data and/or filtered burst files as well as the results of reconstruction were written to tape using a computing center tape robot.

4.5.5 Level 3 Trigger (L3)

Before the data were stored, they were classified and filtered using the information from the reconstruction of charged and neutral particles in the software level 3 filter and real-time reconstruction, running on the CERN batch system. The program read raw data files, one for each burst, called a set of decoding and reconstruction routines and performed a series of cuts and splitting or copying of events to different output streams. The parameters of the routines, cuts, and output streams were dynamically chosen based on the properties of the event, e.g. the trigger information collected online (see Chapter 5). They could be modified as the event was being processed. In this way, only the routines needed to classify the event were called. The information on the desired handling of the events as well as some general parameters to control the program were stored in the online database using an ASCII configuration file.

The L3 acted as a filter using coarse and fast selection algorithms to reject quickly some classes of unwanted events. The purpose was to decrease the amount of data that was stored and that had to be handled in future reconstruction passes. It also loosened the time restrictions on the full real time reconstruction. For each cut, events were appropriately downscaled in order to measure offline the efficiency of the cut. During the 2003 and 2004 data taking periods the L3 was not applying any cut on the events, writing all available data for the later offline analysis.

4.5.6 Data Processing and Format

In order to decrease the data volume and increase accessibility, the L3 produced at least two additional output formats, namely COMpACT (COMpACT Optimized Program to Access Countless Tera Bytes) and superCOMpACT from the raw data obtained from the subdetectors.

The typical size of the raw-data of one burst was ≈ 500 MB; while a typical COMpACT file size was ≈ 10 MB. The main advantage of COMpACT format was that, instead of the low level information of the raw data, it contained valuable reconstructed information and physical variables. SuperCOMpACT files had essentially the same physical information that was contained in the COMpACT files, with the exclusion of some variables not needed for an offline analysis and the advantage of reduction of a factor of 10 in the data files size with respect to COMpACT. Both COMpACT and raw files went to tape.

After the data taking period, all the raw data stored on tape were reprocessed again by the L3, which was configured not to reject events and to write different COMpACT data streams.

To read the COMpACT and superCOMpACT files, the COMpACT program was used. It provided a framework that allowed users to write their analysis code within predefined functions.

5 Trigger System

In NA48/2, the trigger was set up in three trigger levels:

- A very fast level 1 trigger, which used only energy sums, fast track information and signals from the veto systems and the hodoscopes to generate a pre-trigger signal for the more sophisticated level 2 trigger stage.
- The level 2 trigger stage, where the information of different subdetectors was combined and a fast reconstruction was performed to gain real physics information on momentum, mass and charge of the decay products and the initial particle. This process was done in two different subsystems, one for the charged decay products (charged trigger) and one for the neutral decay products (neutral trigger).
- The level 3 trigger stage, a software trigger, was running on fully reconstructed data samples to reduce the amount of data to be stored on tape and to perform first splits by writing data to different output streams.

The information from all channels of all subdetectors was continuously digitized at a frequency of 40 MHz. The produced data were stored locally in temporary circular buffers that were able to record the data of the previous 200 μ s. The detector was sampled every 25 ns (1 time slice) and samples were recorded in time windows of 200 ns.

The trigger system was implemented as a chain of different pipelined electronic systems. Every stage of the chain elaborated the information and reduced the amount of data to pass to the next stage. The process terminated with the generation of a trigger word in the trigger supervisor.

A trigger decision was produced every clock cycle. In case of a positive decision, the acquisition system of each subdetector recorded the digitized information. These data were then stored in local buffers of each subdetector, big enough to keep the data of a whole burst. During the time between the bursts, the PC-farm collected the data from the various subdetectors and built complete events and bursts. Afterwards, these raw data were sent to the CERN Computing Center and processed by the level 3 trigger/real time reconstruction program (L3). Figure 5.1 gives an overview over the whole trigger system. In the following sections the different stages of the trigger will be described in more detail.

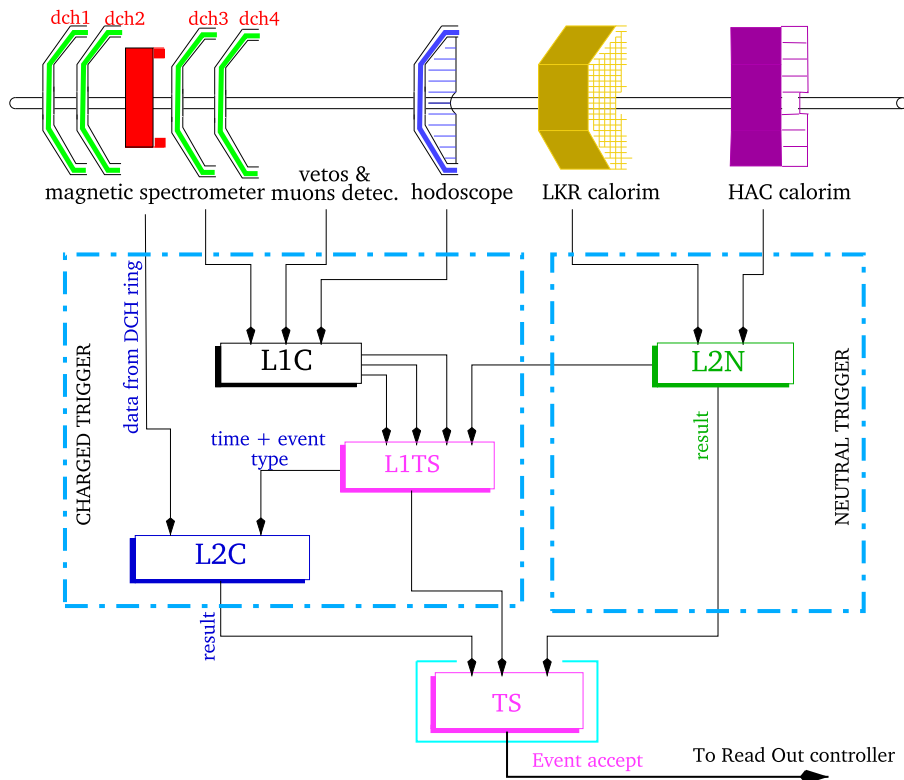


Figure 5.1: Scheme of the NA48/2 trigger levels 1 and 2 [51].

5.1 Charged Trigger Subsystem

The charged trigger subsystem consisted of three layers: the level 1 pre-trigger (L1C), the trigger supervisor of level 1 (L1TS) and the mass box (MBX or L2C).

5.1.1 Level 1 Trigger (L1C)

The L1C was the lowest level of the charged trigger system. This trigger reduced the input rate to the next stage to about 100 kHz. It provided a set of triggers to select decays by combining the various inputs:

- From the hodoscope, a simple information on the topology of the event was obtained. Coincidences of the first and the second plane permitted to know in which quadrant the charged particles hit.
 - Q1:** at least one time coincidence of one horizontal and one vertical channel in the same quadrant, which means at least one charged track in a quadrant.
 - Q2:** at least two coincidences between the horizontal plane and the vertical plane.

- The NHOD provided only the information of the presence of any kind of shower in the LKr to the trigger system. The signal, called **T0N**, was useful as a minimum bias trigger for efficiency studies.
- The MUV provided information on the compatibility of the hits in the scintillators with one muon: 1μ by requiring at least one signal from the μ -veto scintillators.
- The coincidences made within each pocket of the AKL were summed to obtain a trigger condition that was used as a veto. An **!AKL** signal vetoed on a time coincidence between the two layers of at least one AKL pocket.

An additional system for the L1C was the DCH multiplicity box. It counted the hits in DCH1 and issued different signals depending on whether the hit counts were compatible with one or more tracks.

5.1.2 Level 1 Trigger Supervisor (L1TS)

The L1TS [8] had to decide within $5\ \mu\text{s}$ whether a trigger condition was fulfilled. It combined the signals from the L1C, the DCH multiplicity logic, calibration pulsers and the neutral trigger (Sec. 5.2.1), all synchronized to the common NA48 clock. The signals were shaped to fit in one cycle of the 40 MHz clock (one time slice¹) and were stored in the so called pattern units.

According to the output of the L1TS (associated to a time stamp), data from the end buffers of the DCHs were retrieved and transferred to the L2C input queue. A 3 bit code (strobe) identifying the topology of the events was produced. Two more time stamp bits (the fine time) obtained from the hodoscope signals were also provided.

5.1.3 Level 2 Charged Trigger (L2C or MassBoX)

The L2C [5] was a mixed hardware and online software system, which used mainly the information from the magnetic spectrometer. It asynchronously handled events on the base of the 3 bit identification code of the DCH multiplicity box and produced an answer within $100\ \mu\text{s}$. It was doing a fast online reconstruction of the events using the data sent from the DCHs which allowed it to perform complicated algorithms like vertex reconstruction and the computation of invariant masses.

The L2C was made of 5 subsystems: the coordinate builders (CB), the event builder and dispatcher (EBD), the event workers (EW), the monitoring and interface service cards (MISC), and the control workstation. The L2C was fed with drift chamber data (hits) selected by the L1TS at a rate of 170 kHz. The

¹To increase the efficiency of the coincidences, the signals could be widened up to three time slices.

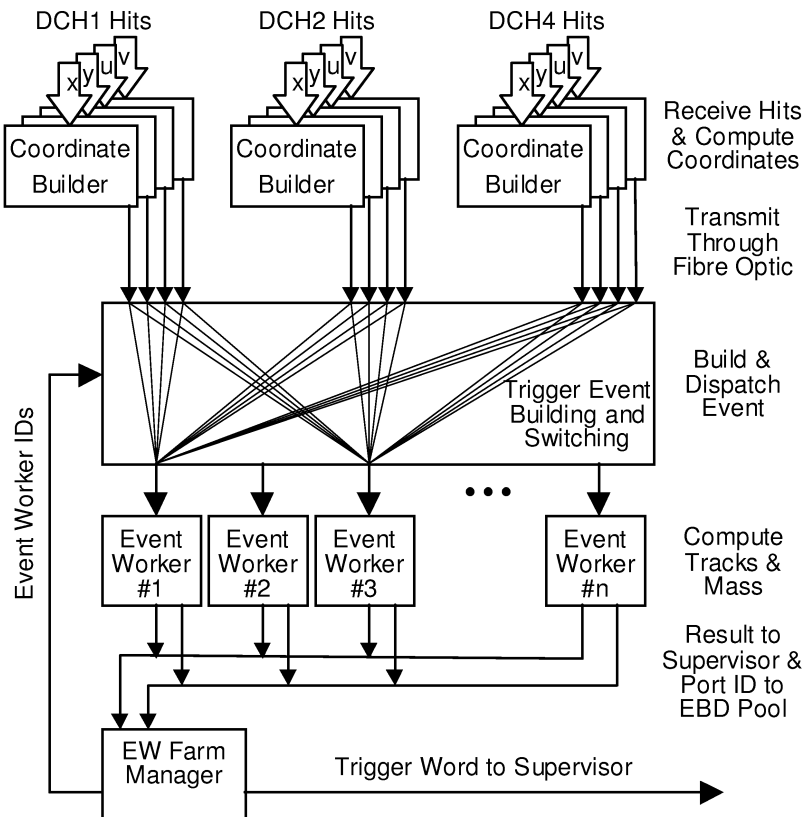


Figure 5.2: The L2C was an asynchronous queued system. The requests of the L1TS were first queued inside the magnetic spectrometer readout, then fed into the coordinate builders, which calculated the coordinates and sent the results into the event builder dispatcher (EBD). The role of the EBD was to pack together the coordinates lists coming from coordinate builders and send them to an available event worker [5].

CB received the data of the hits in the two planes of a view. There were two CB (A and B) for each view of the chambers 1, 2 and 4. Putting together the raw data coming from the two planes of a view, the CB processed them through a 40 MHz pipelined algorithm to obtain a pair of indexes that fed a 2-dimensional look up table which gave the corresponding coordinate value. The coordinates of the hits were sent to the EBD that routed them to the first available event worker. There, the coordinate packets were used to build the particle space points, tracks and magnetic deflections and then from this information vertices, momenta and invariant masses were calculated. Afterwards, the EW issued a trigger word which contained the time stamp at which the L1C request was issued and summarized basic properties of the event. The word was sent to the monitoring and interface service cards (MISC) which transmitted it to the general trigger supervisor (TS). The whole process is schematized in Figure 5.2.

5.2 Neutral Trigger Subsystem

The NA48/2 level 2 neutral trigger was a dead-time free fully pipelined trigger. Its primary purpose was to monitor the $K^\pm \rightarrow \pi^\pm \pi^0 \pi^0$ L2C trigger, and also provided calorimeter signals to the L1TS.

5.2.1 Neutral Trigger (L2N)

The neutral trigger [52, 15, 33] (NT) was a 40 MHz dead-time free pipeline which provided trigger information based on a large number of digitized sum signals, obtained from the cells of the LKr calorimeter. It reconstructed the number of showers seen in each projection of the calorimeter, the total energy, the energy center of gravity, and the neutral vertex. The full NT chain produced a trigger decision every 25 ns after a fixed delay of 3.2 μ s from the event time.

Figure 5.3 gives an overview of the full system. It also shows schematically the reduction of the data size after each step. The information provided by the Peak Sum System [13] was sent to PMBs, for monitoring, and to the Look-Up Table system [15] (LUT), where they were merged to obtain the needed physical quantities and the trigger cuts were applied. The LUT calculated also the sum of LKr and HAC energies and sent all the information to the trigger supervisor and the charge trigger chain.

Algorithms

The information complexity (about 13500 cells from the LKr calorimeter) was reduced by summing the LKr cell pulses into 64 vertical and 64 horizontal strips. That means dividing the calorimeter in rows and columns 4 cm wide. To calculate physical quantities quickly, the information of the single cells of the LKr were summed in horizontal and vertical projections in two steps:

- In the first step the cells were summed in groups of 16 (2×8) cells (supercells) with analog circuits. For the two views (x and y), the supercells were oriented in the two different directions. The signal of each cell was used twice in the analog-sum procedure.
- Afterwards, the 128 rows and 128 columns were grouped in 64 ($128/2$) rows and 64 columns with a maximum of 16 ($128/8$) supercells each. The signals of the supercells entered the Vienna Filter Module (VFM).

The obtained pulses were then digitized and sent to the neutral trigger (NUT) computing chain. Four quantities were reconstructed every clock cycle by the trigger electronics and used to perform cuts and make a decision:

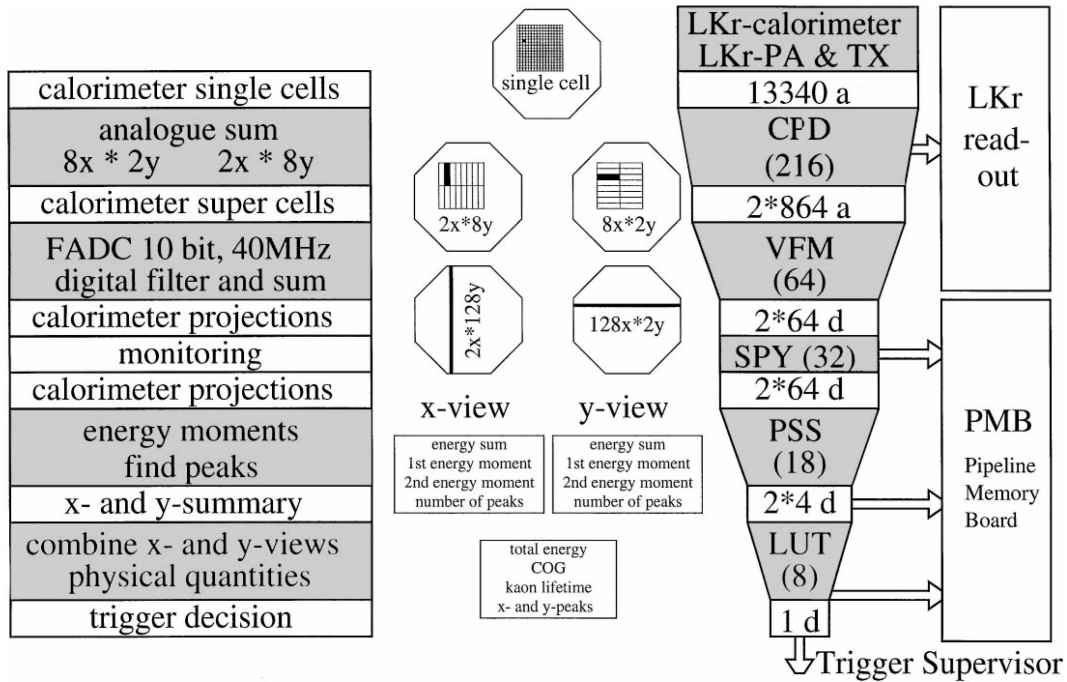


Figure 5.3: Details of the trigger for neutral particles (Neutral Trigger) [33]. The complete trigger chain of the neutral trigger consisted of several subsystems and operated in the following way: the Vienna Filter Module (VFM) system processed the analogue signals from the Calorimeter Pipelined Digitizers (CPD) modules and produced digitized, filtered and summed outputs; the SPY system provided a complete self-testing and online monitoring facility for the downstream components of the chain; the Peak Sum System (PSS) was the stage of the neutral system pipeline chain where the total energy and the weighted energy sums (moments) were computed from the individual strip energies, and where clusters were detected; the look-up tables (LUT) system implemented the final part of the computation, performed event selection and defined the trigger time; the PMB system was finally used to read out the data from the SPY, PS and LUT modules.

- The number of 1-dimensional clusters (peaks) in the calorimeter (both in X- and Y-view). To reduce background or to select a signal, cuts on the maximum or minimum number of clusters in both views were applied.
- The total energy E_{LKr} measured by the LKr calorimeter. The system summed the strip energy information independently for x - and y -view. The total energy was then defined as the mean of the two values obtained by the two views. This reconstructed energy was required to be above a threshold. At this stage, also the total energy deposited in the hadron calorimeter (E_{HAC}) and the sum of the energy in the two calorimeters ($E_{TOT} = E_{LKr} + E_{HAC}$) were computed.

- The center of gravity of the energy distribution $COG = \sqrt{M1_x^2 + M1_y^2}$, with

$$M1_x = \frac{\sum_i x_i E_{x_i}}{\sum_j E_{x_j}}, \quad M1_y = \frac{\sum_i y_i E_{y_i}}{\sum_j E_{y_j}} \quad (5.2.1)$$

the first momenta of the energy. The sum extends over all clusters. E_{x_i} and E_{y_i} represent the energy reconstructed from the i^{th} horizontal and vertical strip, and x_i and y_i the strip center coordinates). This quantity was used to cut away decays of scattered kaons in collimators and cases where one or more of the decay products missed the calorimeter.

- For kaons with the full energy reconstructed in the LKr, the decay position as a function of the nominal kaon mass (m_K) is given by:

$$z_{vertex} = z_{LKr} - \frac{1}{m_K} \cdot \sqrt{E_{LKr} \cdot (M2_x + M2_y) - (M1_x^2 + M1_y^2)}, \quad (5.2.2)$$

where $M1_x$, $M1_y$, $M2_x$ and $M2_y$ are the x - and y -components of the first and second moments of the energies of the clusters in the calorimeter, and z_{LKr} is the z -position of the calorimeter.

All the cuts on the above listed variables were programmable, providing the possibility of adapting the trigger selection criteria to different categories of events. All the cuts were performed in parallel.

5.3 L2 Trigger Supervisor (L2TS)

The decisional system of the NA48 trigger, the trigger supervisor [7] (L2TS or simply TS), collected the information from L1TS, L2C, L2N, and L1C and took the final decision whether the event should be recorded or not. It also provided the final trigger word and time-stamp and sent the command to record the event information before the end of the $\approx 200 \mu\text{s}$ data persistence time to the Read Out Controllers (ROC).

6 Data Taking in 2003

The main run of NA48/2 in 2003 was scheduled from June the 12th to September the 8th, including ≈ 8 days of machine development (MD). The first ten days of the run were devoted to understanding and tuning the new beams, analyzing the recorded data, investigating background conditions, optimizing triggers and setting up the detector.

Since June the 22nd, the data taking proceeded under nominal conditions. In order to minimize systematic uncertainties related to the detector asymmetry and beam structure, the magnetic fields in the spectrometer and beam line magnets were alternated regularly. The spectrometer magnet current was alternated on a daily basis, and all the beam line magnets were cycled and inverted once per week during the MD pauses. Thus a self-complete data set, called super sample, was accumulated over a two-week period. The chosen cycle provided stability of running conditions within these two-week periods.

Two complete super samples (SS1 and SS2) and a partial one (SS3) were accumulated under relatively stable conditions in the latter part of the run, from August the 6th to September the 7th. These are the data which were used in this thesis. The data amount collected during 2003 is summarized in Table 6.1.

The trigger conditions of the data taking period during 2003 are briefly described in this chapter.

total number of triggers	7×10^9
Number of bursts	2.2×10^5
Raw Data Total Size	80 TB
Compact Data Total size	20 TB
Calibration Data Total Size	3.5 TB

Table 6.1: Data volume collected during the 2003 data taking period [67].

6.1 Level 1 Trigger (L1C)

The signals that the L1C was sending to the level 1 trigger supervisor during the 2003 are summarized in Section 5.1.1.

6.2 Neutral Trigger (L2N)

The following bits and requirements were provided by the L2N in 2003 (the signs '·', '+' and '!' stand for the logic 'and', 'or' and 'not'):

- **COG**, Center of gravity at the position of the LKr calorimeter:
 $COG \leq 30$ cm
- **LKRmbias**, Minimum energy in the LKr calorimeter:
 $E_{LKr} \geq 10$ GeV
- **NTPEAK**, Number of peak clusters in at least one of the LKr projection:
 $(n_x > 2) + (n_y > 2)$
- **E_{TOT}**, Total energy reconstructed in both calorimeters:
 $E_{TOT} \geq 30$ GeV
- **KMU3PRE**, Pre-trigger for $K^\pm \rightarrow \pi^0 \mu^\pm \nu$ events:
 $E_{LKr} \geq 15$ GeV
- **KMU2PRE**, Pre-trigger for $K^\pm \rightarrow \mu^\pm \nu$ events:
 $(E_{LKr} \leq 10 \text{ GeV}) \cdot (E_{HAC} \leq 10 \text{ GeV})$
- **KE2PRE**, Pre-trigger for $K^\pm \rightarrow \pi^0 e^\pm \nu$ events:
 $(M0T^1 < 2400) \cdot (E_{HAC} \leq 10 \text{ GeV}) \cdot (E_{LKr} \geq 15 \text{ GeV})$
- **ZVTX**, z vertex: $z_{vertex} \leq 9500$ cm
- **NTNOPEAK**, 'Neutral pre-trigger':
 $(z_{vertex} \leq 9500 \text{ cm}) \cdot (E_{LKr} \geq 15 \text{ GeV}) \cdot (COG \leq 30 \text{ cm})$

¹ $M0T = M0 \times M2 - M1^2$, where $M0$ is the total energy measured in the LKr calorimeter and $M1$ and $M2$ the first and second energy momentum as defined in Section 5.2.1.

Bit	Trigger condition
bit 0	$(\text{NTPEAK} + \frac{Q1}{10} \cdot \text{LKrbias} + Q1 \cdot !Q2 \cdot 1\mu \cdot \frac{!AKL}{100} \cdot \text{KMU3PRE}) \cdot (Q1 + Q2)$
bit 1	$(Q1 \cdot !Q2 \cdot 1\mu \cdot \frac{!AKL}{100} + Q1 \cdot !Q2 \cdot 1\mu \cdot \frac{!AKL}{100} \cdot \text{KMU2PRE} + \frac{Q1}{100}) \cdot (Q1 + Q2)$
bit 2	$(Q2 \cdot !AKL + \frac{Q1}{100} + \text{random}) \cdot (Q1 + Q2)$

Table 6.2: The L1TS trigger bits. Fractions appear when a signal trigger is downscaled. 'random' is a random trigger given by the beam monitor. The $(Q1 + Q2)$ requirement provided a fine time to the L2C processors.

Code	Name	Trigger	D
bit 0	MB-2VTX	2-vertex	1
bit 1	MB-1VTX	1-vertex with mass cut	1
bit 3	CPRE	$Q2 \cdot !AKL + Q1/100$	100
bit 4	MB-1TRK-P	anti $\pi^\pm\pi^0$ cut	1
bit 5	MB-1TRK-3	anti K_{l2} cut	20
bit 6	MB-1TRK-2	K_{l2} cut	20
bit 8	NTNOPEAK	$z_{vertex} \leq 95\text{m} \cdot E_{LKr} \geq 15\text{GeV} \cdot COG \leq 30\text{cm}$	80
bit 9	NMBIAS	T0N	200
bit 10	NTPEAK	$(n_x > 2) + (n_y > 2)$	50

Table 6.3: L2 default trigger word used for data analysis during 2003. The last column contains the different downscaling factors applied by the trigger supervisor.

6.3 Level 1 Trigger Supervisor (L1TS)

As a result from the signals received from the L1C and the L2N, the L1TS issued the three bits listed in Table 6.2.

6.4 L2 Trigger

The default L2 trigger word configuration collecting data for analysis purposes is shown in Table 6.3. The first two trigger bits from the table were devoted to the collection of 'charged' decays of the kaon (decays into several charged tracks). The next trigger bit, CPRE (charged pre-trigger), selected one-track events through the Q1 condition, and was strongly downscaled² not to saturate the bandwidth. The MB-1TRK-P or MFAKE trigger computed an effective 'missing mass' of the event (Section 6.4.1), rejecting $K^\pm \rightarrow \pi^\pm\pi^0$ decays. The trigger bits MB-1TRK-3 and MB-1TRK-2 were used for semi-leptonic decays. The last two trigger bits came from the neutral trigger branch (L2N). T0N was used as a minimum bias trigger and the NTPEAK trigger condition was downscaled by a factor of 50.

²A downscaling factor 'D' means that only one event out of 'D' triggered events is accepted.

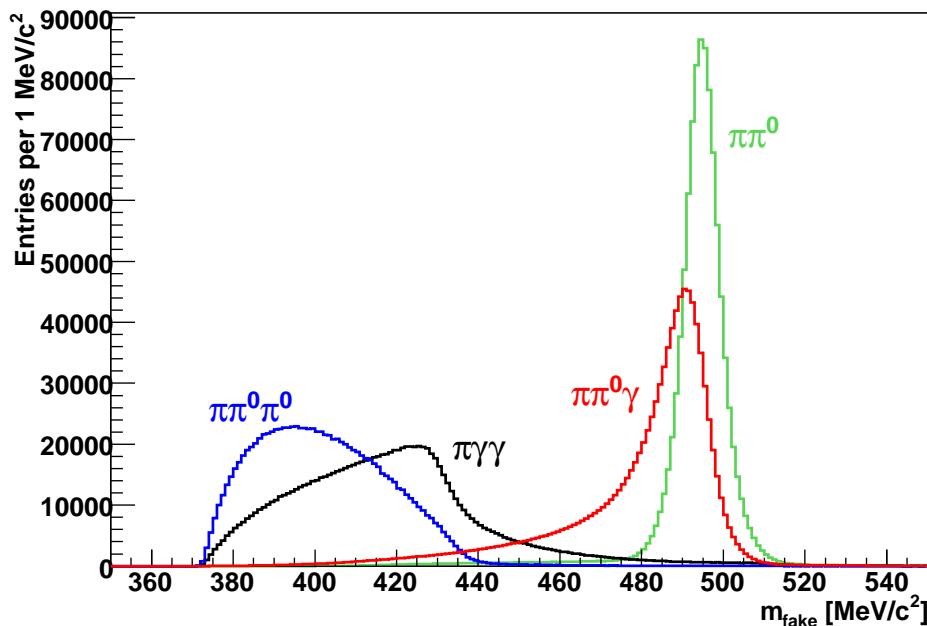


Figure 6.1: m_{fake} distribution for different Monte Carlo simulated events. MC $K^\pm \rightarrow \pi^\pm \gamma \gamma$ decays are generated according to [37] and with $\hat{c} = 2$. The histograms are normalized to each other.

6.4.1 L2 MFAKE Trigger

In 2003, the L2C algorithms needed to allow for a highly efficient selection of $K^\pm \rightarrow \pi^\pm \pi^0 \pi^0$ events necessary for charged asymmetry measurements [18], rejecting the dominant $K^\pm \rightarrow \pi^\pm \pi^0$ background. In order to do that, a track was introduced in the algorithms to fake the kaon if it had not decayed. The trigger, called MFAKE, assumed then a momentum of $\vec{p}_K = (0,0,60)$ GeV, which could be extrapolated to any part of the detector. An effective missing mass m_{fake} , was implemented as

$$m_{fake}^2 = m_{K^\pm}^2 + m_{\pi^\pm}^2 - MM^2, \quad (6.4.1)$$

with m_{K^\pm} and m_{π^\pm} the nominal K^\pm and π^\pm masses, respectively, and MM^2 the missing mass squared. Writing Eq. 6.4.1 as a function of the pion energy in the kaon rest frame:

$$m_{fake}^2 = 2E_{\pi^\pm}^{CM} m_K. \quad (6.4.2)$$

In the case of two-body decays, the missing mass is fixed and is equal to the mass of the decay product different from the charged pion. In particular, for $K^\pm \rightarrow \pi^\pm \pi^0$ decays, MM^2 corresponds to the square of the π^0 mass and E_π^{CM}

$$E_\pi^{CM} = \frac{m_K^2 + m_{\pi^\pm}^2 - m_{\pi^0}^2}{2m_K} = 246 \text{ MeV}, \quad (6.4.3)$$

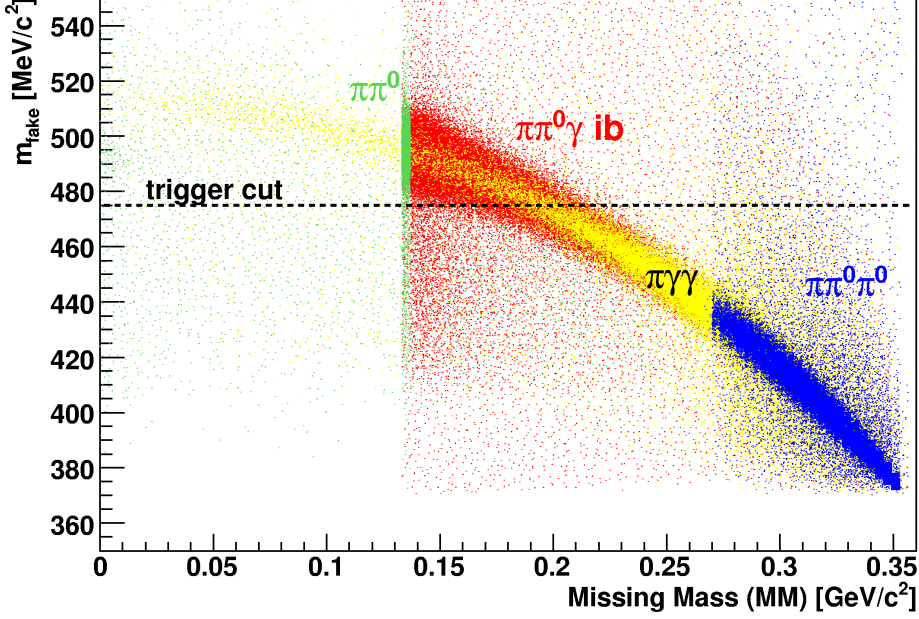


Figure 6.2: Scatter plot showing the m_{fake} distribution of different MC simulated decays as a function of $m_{\gamma\gamma}$.

which is equivalent to $m_{fake} = 489 \text{ MeV}/c^2$.

For a three body decay like $K^+ \rightarrow \pi^+\pi^0\pi^0$, the maximum momentum of the charged pion in the rest frame of the kaon is:

$$p_{\pi^\pm}^{CM,max} = \frac{1}{2m_K} \sqrt{(m_K^2 - (2m_{\pi^0} + m_{\pi^\pm})^2)(m_K^2 - (2m_{\pi^0} - m_{\pi^\pm})^2)} = 0.133 \text{ MeV}/c, \quad (6.4.4)$$

which implies that $m_{fake} \leq 436 \text{ MeV}/c^2$. Figure 6.1 shows the m_{fake} distribution for Monte Carlo $K^\pm \rightarrow \pi^\pm\pi^0\pi^0$ (blue), $K^\pm \rightarrow \pi^\pm\pi^0$ (green), $K^\pm \rightarrow \pi^\pm\pi^0\gamma$ inner bremsstrahlung (red), and $K^\pm \rightarrow \pi^\pm\gamma\gamma$ (black) decays.

In 2003, the m_{fake} online resolution for $K^\pm \rightarrow \pi^\pm\pi^0$ events was $7.5 \text{ MeV}/c^2$, and $\approx 4 \text{ MeV}/c^2$ offline. The trigger cut was set to $m_{fake} < 475 \text{ MeV}/c^2$, rejecting all events with m_{fake} above this value. Only during the third data taking period (SS3) the trigger cut was changed to reject events with $475 < m_{fake} < 515 \text{ MeV}/c^2$. This trigger requirement not only implied the clean rejection of $K^\pm \rightarrow \pi^\pm\pi^0$ decays, but also the loss of $K^\pm \rightarrow \pi^\pm\gamma\gamma$ with a di-photon mass $m_{\gamma\gamma} < 0.194 \text{ GeV}/c^2$, as can be inferred from Equation 6.4.1. Figure 6.2 shows the scatter plot of the m_{fake} distribution versus the missing mass of different Monte Carlo samples before any analysis cut.

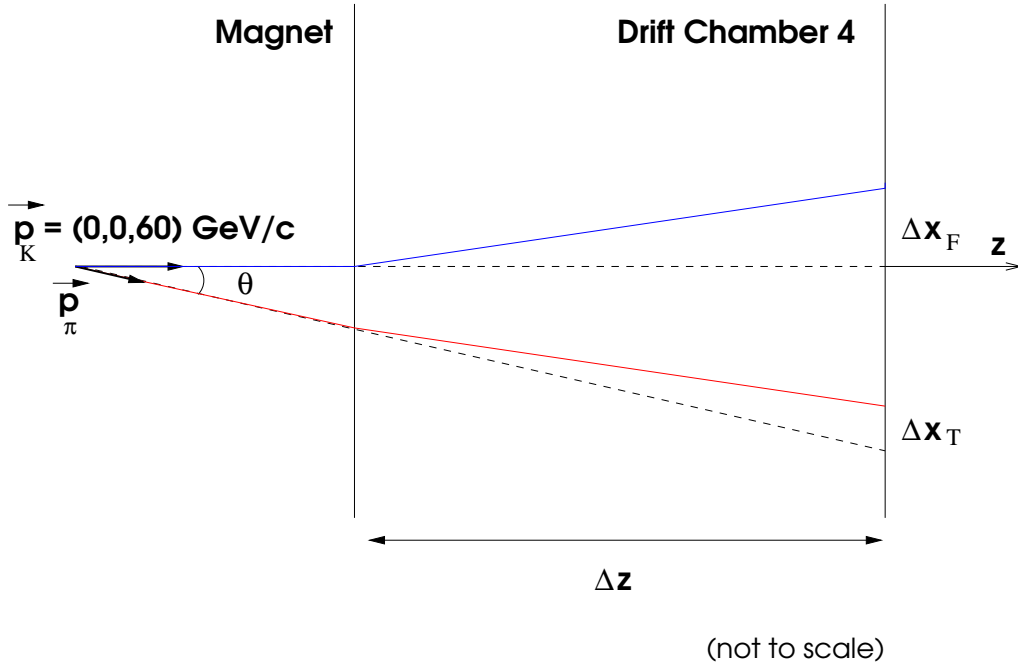


Figure 6.3: Schematic representation of the deviation of the fake kaon track (blue) and the pion track (red) as it is used in the MFAKE-trigger calculation.

MassBoX algorithm

The MassBoX algorithm looped over pairs of one real and fake track segments in DCH1 and DCH2 until a fake-vertex was found between the two tracks (the kaon track and the real track). A vertex was found if the closest distance of approach between the tracks was less than 5 cm. The space points in DCH4 were then calculated for both tracks assuming a deviation Δx_F in the x-direction of flight of the kaon. Finally, m_{fake} was calculated for the two tracks as:

$$m_{fake}^2 = \frac{1}{|\Delta x_F \Delta x_T|} \left[p_{kick}^2 (z_{DCH4} - z_{MAG})^2 \theta^2 + m_\pi^2 |\Delta x_T|^2 + m_K^2 |\Delta x_F|^2 \right],$$

where θ is the opening angle, Δx_T is the magnet to DCH4 displacement of the real track, Δx_F is the constant displacement of the fake track, and p_{kick} is the transversal momentum provided by the magnet. Equation 6.4.1 is recovered by considering that the particles are completely boosted in the z -direction, and calculating the flying distance L from the change of the z -coordinate. In this way, Δx_T and the angle θ are the only quantities to be measured by the trigger [61]. Figure 6.3 shows the quantities involved in the m_{fake} computation.

6.5 Trigger Chain for the Selection of $K^\pm \rightarrow \pi^\pm \gamma \gamma$

The neutral trigger logic in 2003 was designed to efficiently collect $K^\pm \rightarrow \pi^\pm \pi^0 \pi^0$ events. Most of all other 'neutral' decays (decays with photons in the final state) were also initially selected by the L1 NTPEAK trigger requiring more than two peaks in at least one of the projections of the calorimeter, and then by the L2 MFAKE trigger. This was the case of the signal $K^\pm \rightarrow \pi^\pm \gamma \gamma$ decays, which were collected through the L1 bit 0 (see Section 9.2) and then the L2 MFAKE trigger, since those triggers were not downscaled. As a consequence, the efficiency of the trigger chain for the $K^\pm \rightarrow \pi^\pm \gamma \gamma$ selection was very small, since these decays did not always made more than two energy peaks in LKr calorimeter (see Section 9.2.1).

To cancel systematic effects arising from the efficiency measurement, normalization $K^\pm \rightarrow \pi^\pm \pi^0$ decays used to measure $\text{BR}(K^\pm \rightarrow \pi^\pm \gamma \gamma)$ were also collected from the NTPEAK trigger, which was used as a L2 trigger downscaled by a factor of 50. Trigger efficiencies for $K^\pm \rightarrow \pi^\pm \gamma \gamma$ and $K^\pm \rightarrow \pi^\pm \pi^0$ decays will be discussed in detail in Chapter 9.

7 The Monte Carlo Simulation

The use of Monte Carlo (MC) simulations in this thesis had four purposes:

- The determination of the acceptance of a decay, i.e. the number of selected events with respect to the number of generated events in the same energy and z -decay vertex range.
- The computation of trigger efficiencies which cannot be measured using signal data events.
- The identification and rejection of background sources by studying and comparing the behaviors of the different decays.
- The access to both the reconstructed and true values of the generated magnitudes.

The Monte Carlo program used for the simulation of the 2003 data taking period is called CMC (Charged kaons Monte Carlo). It was based on the MC for neutral kaons of the NA48 experiment (NASIM [39]) and used the GEANT¹ package of the CERN libraries [6].

7.1 Simulation of Charged Kaons Spectra

Kaon decays are generated within a certain energy and z -decay vertex range. The production spectrum used in order to generate the energy and momentum of the kaon beam was

$$\frac{d^2 N}{d\Omega dp} = A \left[\frac{B}{p_0} e^{-Bp/p_0} \right] \cdot \left[\frac{2Cp^2}{2\pi} \right], \quad (7.1.1)$$

with p the momentum of the kaon, and $p_0 = 400$ GeV/ c the momentum of the protons coming from the SPS onto the target. The constants A , B and C depend on the charge and quark content of the kaon produced and have the following values [10]:

¹GEometry ANd Tracking

	A	B	C
K^+	0.16	8.5	3
K^-	0.10	13.0	3.5

The kaon spectrum at the exit of the NA48/2 beam line was defined by the beam line optics rather than by the initial spectrum (20% more K^+ were actually observed than expected from Eq. 7.1.1). The simulation of the beam transport system was done using a program called TURTLE² [28]. This included higher order chromatic aberrations, effects of non-linearities in magnetic fields, and higher order geometric aberrations due to the accumulation of second order effects. The parameters of the beam simulation were tuned on a run by run basis for K^+ and K^- in order to reproduce the momentum distribution of the beam.

The decay spectrum depends on the lifetime of the decaying particle and was obtained by weighting the production spectrum with the decay probability expressed as

$$\frac{d^2N}{dzdE} = e^{-z/\lambda}, \quad (7.1.2)$$

with $\lambda = \gamma\beta c\tau_{K^\pm}$ being the mean free path. After weighting the production spectrum, an integration over the desired decay range must be performed.

7.2 Simulation of Decays

The momenta of the kaon decay products were generated according to phase space and weighted afterwards by the corresponding matrix element of the generated decay. The calculation of the 4-momentum of the decay products was first done in the rest frame of the decaying kaon (CM), and then a Lorentz transformation boosted them into the laboratory frame. After this, the flight of the particles through the detector was simulated including all the possible interactions with the different components [6]:

- Positron annihilation
- Bremsstrahlung
- Compton Scattering
- Decay in flight
- Delta ray production
- Hadronic interactions

²Trace Unlimited Rays Through Lumped Elements

- Continuous energy loss
- Multiple scattering
- Photoelectric effect
- Pair conversion

and detector resolution effects.

Monte Carlo events were generated in COMPACT format (see 4.5.6), allowing that the same reconstruction program used for the data analysis was used also for Monte Carlo events.

7.2.1 Simulation of Phase Space

The phase space was generated for each decay by calling the CERN routine GENBOD from CERNLIB³. GENBOD generated a multi-particle weighted event in the center of mass of the decaying particle according to Lorentz-invariant Fermi phase space [77]. The total CM energy as well as the number and masses of the outgoing particles were specified by the user and might be changed from event to event. The weight given by GENBOD to each event, was then multiplied by the 'matrix element' of the simulated decay.

7.2.2 Simulation of Signal and Normalization Channels

Simulation of $K^\pm \rightarrow \pi^\pm \gamma \gamma$ Decays

The simulation of $K^\pm \rightarrow \pi^\pm \gamma \gamma$ decays (signal channel) was done according to the definition by [47]:

$$\frac{\partial \Gamma}{\partial y \partial z} = \frac{M_K}{2^9 \pi^3} \left[z^2 (|A + B|^2 + |C|^2) + \left(y^2 - \frac{1}{4} \lambda(1, r_\pi^2, z) \right)^2 \cdot (|B|^2 + |D|^2) \right], \quad (7.2.1)$$

and using Chiral Perturbation Theory of $O(p^6)$ for the A , B , C and D amplitudes of this decay [37]. This means that non vanishing G27 and $\eta - \eta'$ mixing effects [60] were not included in C and that vector meson exchange was also neglected in the simulation.

Different MC samples of this decay were generated with different values of \hat{c} , for $O(p^6)$ and with radiative corrections in the outgoing pion (Section 7.4). About 14 and 10 million decays were generated with $\hat{c} = 2.0$ and $\hat{c} = 1.74$, respectively.

³The CERN Program Library consists of a number of independent Fortran and C callable libraries and a collection of complete programs.

Simulation of $K^\pm \rightarrow \pi^\pm \pi^0$ Decays

No specific generator was used for $K^\pm \rightarrow \pi^\pm \pi^0$ decays (normalization channel). Since they are two-body decays, the pion momenta are determined by 4-momentum conservation, and the angular distribution in the kaon rest frame is uniform, given that the kaon is a spinless particle. For the π^0 , instantaneous $\pi^0 \rightarrow \gamma\gamma$ decays were generated. A sample of about 8 million $K^\pm \rightarrow \pi^\pm \pi^0$ decays, including radiative corrections effects in the outgoing charged pion, was generated for acceptance studies.

7.2.3 Simulation of the Background

Simulation of $K^\pm \rightarrow \pi^\pm \pi^0 \gamma$ Decays

The generator used for this decay is the one published in reference [32], with a small modification in the weighting factor of the internal bremsstrahlung contribution to this decay⁴. This decay has three different contributions to its final rate, one coming from internal bremsstrahlung of the photon (IB), one due to direct emission of the photon (DE) and a third one caused by the interference (INT) of the two previous contributions:

$$\frac{d\Gamma}{dW} = \underbrace{\left(\frac{d\Gamma^\pm}{dW}\right)}_{\text{IB}} \left[1 + \underbrace{2 \left(\frac{m_\pi}{m_K}\right)^2 W^2 |E| \cos((\delta_1 - \delta_0) \pm \Phi)}_{\text{INT}} + \underbrace{\left(\frac{m_\pi}{m_K}\right)^4 W^4 (|E|^2 + |M|^2)}_{\text{DE}} \right]$$

$$W^2 = \frac{(p_K p_\gamma)(p_\pi p_\gamma)}{m_K^2 m_\pi^2},$$

with all the four-momenta given in the center of mass. E and M are the electric and magnetic dipole contributions, δ_1 , δ_0 the strong re-scattering phases for the two different isospin final states, and Φ the phase difference between the dipole moments and their respective amplitudes [32].

The different contributions were generated separately, to study their different behavior as background for the signal channel. Instantaneous $\pi^0 \rightarrow \gamma\gamma$ decays were assumed for the π^0 decays.

A total of about 97 million, 11 million, and 6.5 million decays were generated of $K^\pm \rightarrow \pi^\pm \pi^0 \gamma$ IB, $K^\pm \rightarrow \pi^\pm \pi^0 \gamma$ DE, and $K^\pm \rightarrow \pi^\pm \pi^0 \gamma$ INT, respectively. These numbers translate in about 21 million, 8 million, and 3.4 million corresponding decays in the $55 \text{ MeV} < T_\pi^{CM} < 90 \text{ MeV}$ kinematic region (where background from $K^\pm \rightarrow \pi^\pm \pi^0$ is minimum). $K^\pm \rightarrow \pi^\pm \pi^0 \gamma$ INT decays contribute negatively to the total number of $K^\pm \rightarrow \pi^\pm \pi^0 \gamma$ decays and need to be subtracted from the IB and DE contributions.

⁴The correction is such, that $(m_\pi^2 - m_{\pi^0}^2)/(2m_K)$ is not neglected in comparison to $0.5 \cdot m_K - E_{\pi^0}$ [67].

Simulation of $K^\pm \rightarrow \pi^\pm \pi^0 \pi^0$ Decays

The decay matrix element for $K^\pm \rightarrow \pi^\pm \pi^0 \pi^0$ decays can be parameterized as

$$|M(u, v)|^2 \approx 1 + gu + hu^2 + kv^2, \quad (7.2.2)$$

with $u = (s_3 - s_0)/m_\pi^2$, $v = (s_1 - s_2)/m_\pi^2$, $s_0 = \frac{1}{3}(s_1 + s_2 + s_3)$, and $s_i = (p_K - p_i)^2$, and where p_K and p_i are the four-momenta of the kaon and the pion (being $i = 3$ the charged pion) [2]. The following values were used for the parameters g , h and k : $g = 0.638$, $h = 0.0825$, $k = 0$.

A number of about 92.6 million $K^\pm \rightarrow \pi^\pm \pi^0 \pi^0$ decays was generated, with both π^0 decaying instantaneously into $\gamma\gamma$.

7.3 Parameters of the Simulation

The Monte Carlo was simulated according to the experimental conditions of each data taking period. This means that parameters like the currents in the magnets of both magnet spectrometer and achromats, that were regularly alternated during the whole run, were read directly from a database together with beam and detector geometry conditions for each of the kaon beams and implemented in the Monte Carlo in a *run by run* basis. The proton intensities were measured for each run and according to these values the corresponding numbers of charged kaon decays for each period were generated.

The simulated pion momentum was chosen by the user, but due to the narrow momentum spread of the beam, the range between 50 and 70 GeV/c already contained the whole spectrum. The chosen generated decay region was $-2200 \text{ cm} < z_{vertex} < 9000 \text{ cm}$, with the z_{vertex} origin at the end of the final collimator. To prevent for resolution effects, wider energy and decay vertex ranges were generated than the ones used in the data selection, where the acceptance region was defined as $55 \text{ GeV} < E_K < 65 \text{ GeV}$ and $-1800 \text{ cm} < z_{vertex} < 7000 \text{ cm}$.

7.4 Radiative Corrections

Normalization and signal events were generated including bremsstrahlung photons emitted by the charged pion [65]. After generating an event without any corrections, PHOTOS read in the four-momenta, masses and types of the particles and produced, with a certain probability, one or more additional photons, correcting the four-momenta of the emitted particles, so that energy and momentum conservation were assured. The CMC MC generator program read back the modified event and proceeded then with the boost into the laboratory system (Section 7.2).

8 Selection of Events

The data used in this thesis correspond to the super samples 1, 2 and 3 of the 2003 data taking period, i.e. to run periods 15620-15703, 15704-15777 and 15778-15790, respectively. Events which belonged to bursts flagged as 'bad' by at least one of the central detectors were rejected. In particular, 20% of the data were excluded from the analysis due to the low efficiency of the NTPEAK trigger during the periods 15652-15663, 15688-15753, and 15786-15790.

Only data with the level 2 MFAKE, NTPEAK or CPRE-Q1/100 trigger bits set were analyzed. The first trigger was used to select the signal $K^\pm \rightarrow \pi^\pm \gamma \gamma$ candidates, while the last two were used to select the normalization $K^\pm \rightarrow \pi^\pm \pi^0$ decays used for measuring the flux.

In the following sections the selection criteria for $K^\pm \rightarrow \pi^\pm \gamma \gamma$ events are explained. The same criteria were applied to both data and Monte Carlo events¹ and were optimized using signal and background simulations in order to obtain a high signal acceptance and a low background contamination. The pre-selection criteria are summarized in Section 8.1, and restrict the initial sample to the events which have a well defined pion track and exactly two good quality photon clusters. The variables used for the complete event reconstruction, like the energy center of gravity, the event vertex position and the di-photon invariant mass, are introduced in Section 8.2. The decay vertex region is then defined in Section 8.3. Background sources and their rejection are studied in Sections 8.4 and 8.5. The set of corrections applied to the reconstruction are explained in Sections 8.6. Finally, the selected signal and normalization candidates are presented in Section 8.7 and 8.8, respectively.

The distribution plots, shown in the different sections of this chapter, contain all the cuts applied up to that stage of the selection. Figures using real data events contain only the potential signal candidates collected through the MFAKE trigger. All the cuts applied in the events selection are summarized in Table 8.5.

¹Time cuts were only applied to data, since the MC simulation did not contain this information.

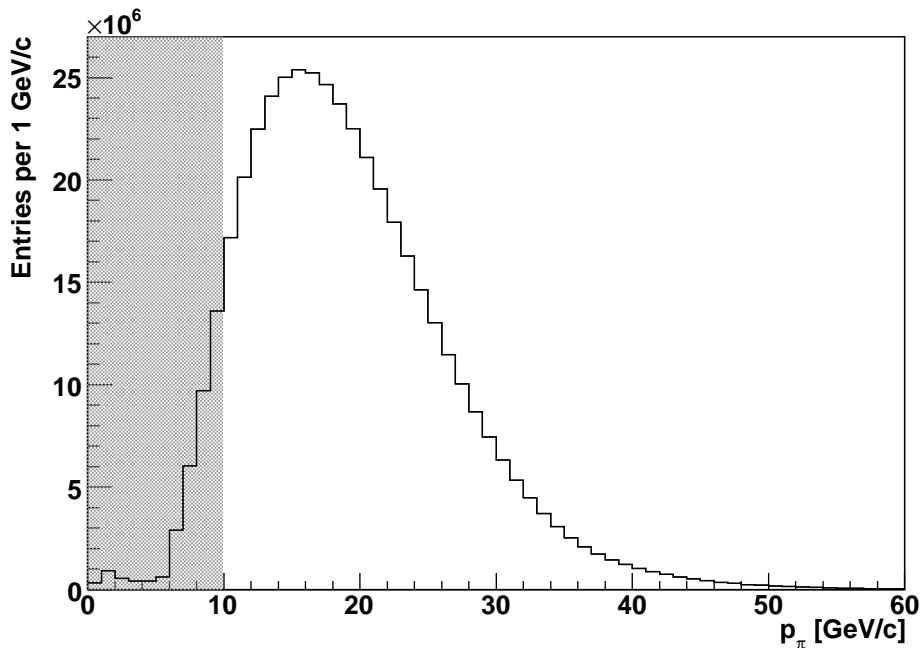


Figure 8.1: Momentum of the track before any selection cut. The shadowed area shows the rejected region.

8.1 Pre-Selection of Events

The criteria used to pre-select events with a $K^\pm \rightarrow \pi^\pm \gamma \gamma$ signature, i.e. events with one pion and two photons in the final state, are summarized in this section.

8.1.1 Selection of the Pion Track

- **Only one charged track in DCHs.** This requirement was used to avoid the presence of decays into three charged tracks in the data sample.
- **Momentum of the track.** A minimum track momentum of 10 GeV/ c was asked for the efficient reconstruction of muon hits in the MUV counters.
- **Distance to the beam pipe.** To ensure a correct momentum reconstruction avoiding the edges of the detector, a radial distance to the center of the beam pipe of $15 \text{ cm} < r_\pi^{DCH1,2,3} < 120 \text{ cm}$ at the first three drift chambers, and $15 \text{ cm} < r_\pi^{DCH4,LKr} < 113 \text{ cm}$ at the last drift chamber and the LKr, was required for the track². The harder cut on the maximum distance to the beam pipe at the DCH4 and the LKr ensures the full energy reconstruction in the calorimeter in case the track is caused by an electron.

²The pion track can be extrapolated to any sub-detector by using the track position at DCH4 and its direction of flight after the magnet in the spectrometer.

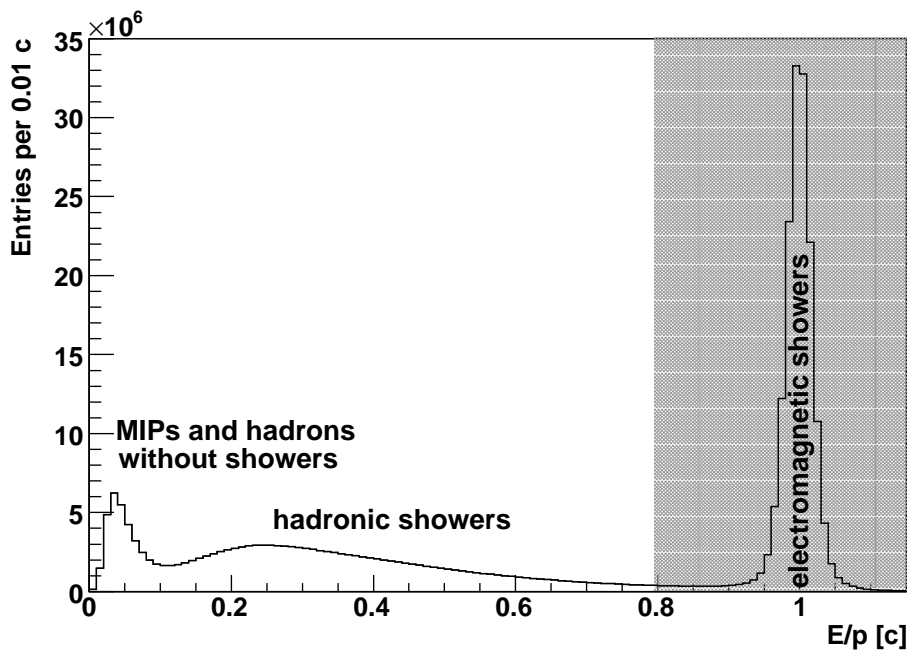


Figure 8.2: E/p distribution. The peak around $1 c$ corresponds to electrons. The broad flat distribution below $0.9 c$ are hadrons that did not deposit all their energy in the calorimeter. The peak close to $0 c$ contains minimum ionizing particles and hadrons that did not interact in the calorimeter. The shadowed area shows the rejected region.

- **Minimum distance to dead cells in the LKr calorimeter.** The track distance to any dead cell in the calorimeter was required to be $d_{track-dead\ cell} > 2$ cm.
- **Particle identification.** The particle identification relied on two methods:
 - **The E/p cut.** E/p is the ratio between the energy deposited by the particle in the LKr calorimeter and the momentum measured by the magnetic spectrometer. While electrons and positrons deposit all their energy in the electromagnetic calorimeter, having E/p centered at $1 c$, pions produce shower fluctuations and deposit only part of their energy, which means $E/p < 1 c$. Minimum ionizing particles like muons, do not leave any energy in an electromagnetic calorimeter, peaking in the E/p distribution around 0 . Figure 8.2 illustrates all these different behaviors. Pion candidates were asked to have $E/p < 0.8 c$.
 - **Muon identification.** Muons are the only particles able to traverse the hadron calorimeter and leave a signal in the muon veto counters. To avoid muons in the decay products, tracks with hits at the MUV were rejected.

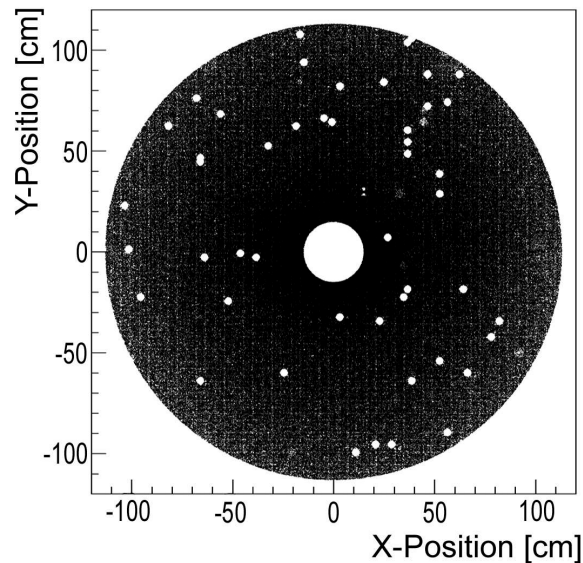


Figure 8.3: Distribution of dead cells (white holes) in the LKr calorimeter during 2003 data taking. Note also the radial geometrical acceptance cuts.

8.1.2 Selection of Photon Candidates

Each event was required to contain exactly two photon clusters meeting the following conditions:

- **Minimum distance to dead cells in the LKr calorimeter.** The minimum distance to any dead cell in the calorimeter should be $d_{\gamma\text{-deadcell}} > 2$ cm. Figure 8.3 shows the distribution of dead cells on the transverse plane of the calorimeter during 2003 data taking.
- **Minimum distance between the photon clusters.** To avoid energy sharing between the clusters at the LKr, the minimum distance between a photon candidate and any other cluster in the calorimeter, $d_{\gamma\text{-cluster}}$, had to be greater than 10 cm.
- **Minimum distance to pion in LKr.** Figure 8.4 shows the energy of the LKr clusters as a function of their distance to the pion impact point at the calorimeter. The populated area at low $d_{\pi\text{-}\gamma}$ shows the shower fluctuation region created by the pion. To minimize the misidentification of clusters belonging to the pion shower as photon clusters, photon candidates had to have a distance to the pion impact point at LKr $d_{\pi\text{-}\gamma} > 30$ cm.
- **Time difference between pion track and photon candidates.** To assign the pion track and the photon clusters to the same event, the difference between the pion time measured at the DCHs and the photon

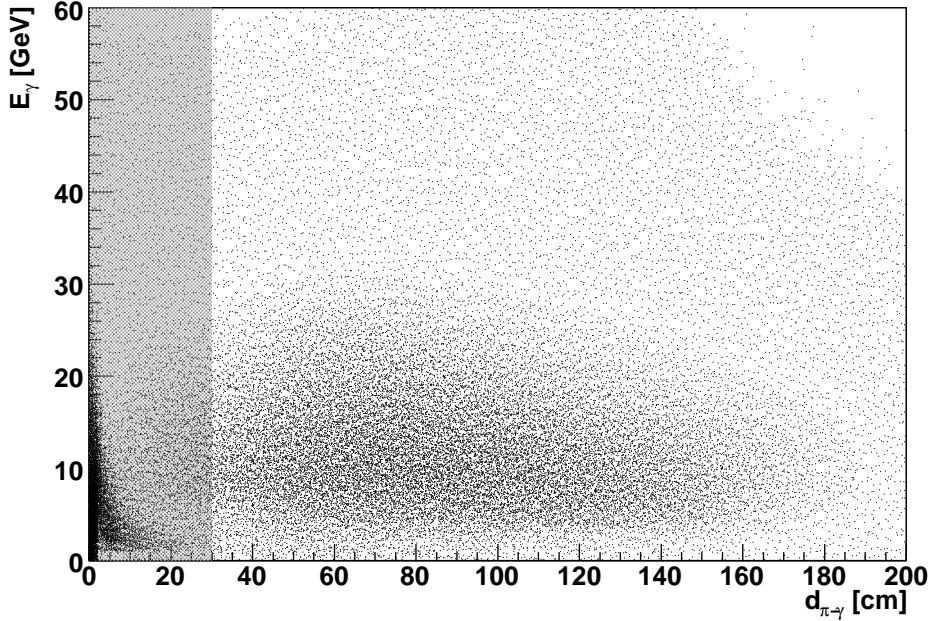


Figure 8.4: Cluster energy, E_γ , as a function of the cluster distance to the pion track at the LKr, $d_{\pi-\gamma}$. The low $d_{\pi-\gamma}$ region shows the shower fluctuations due to the pion shower. The shadowed area contains clusters not accepted as photon candidates.

clusters time measured at the LKr had to be smaller than 6 ns. Figure 8.5 shows the distribution of the time differences between the pion and other clusters at the LKr.

- **Time difference between photon clusters.** The maximum time difference allowed between two photon clusters belonging to the same event was 6 ns.
- **Radial distance to the beam pipe.** Only photon showers fully contained in the geometrical acceptance of the LKr were accepted, $15 \text{ cm} < r_\gamma^{\text{LKr}} < 113 \text{ cm}$.
- **Minimum energy of a photon cluster.** To reject low energy photons arising from bremsstrahlung and from the pion shower (see Figure 8.4), a minimum photon energy of 6 GeV was required (Figure 8.6). This cut was also applied to increase the efficiency of the NTPEAK trigger and to avoid dependencies of the trigger on the photon energy.

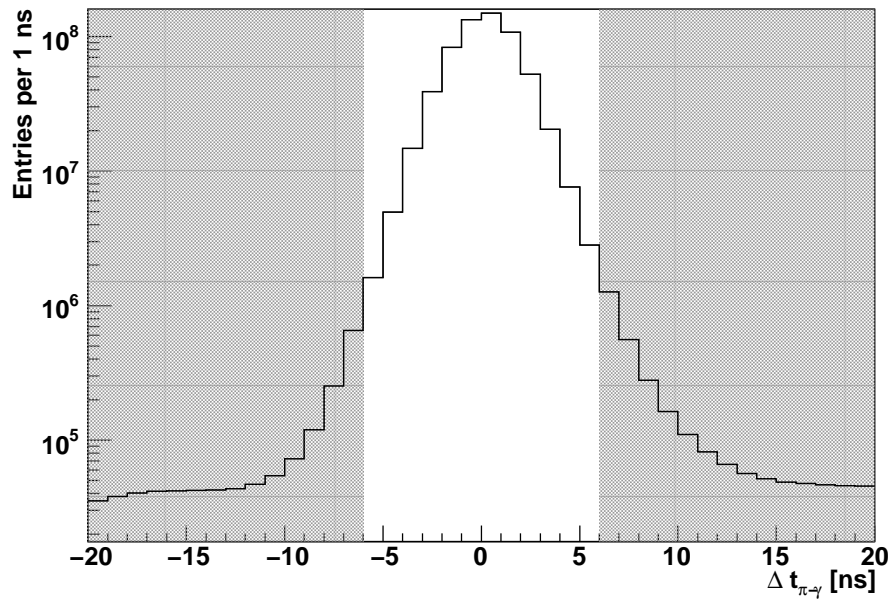


Figure 8.5: Time difference between the pion track and the photon candidates. The shadowed area contains clusters not accepted as photon candidates.

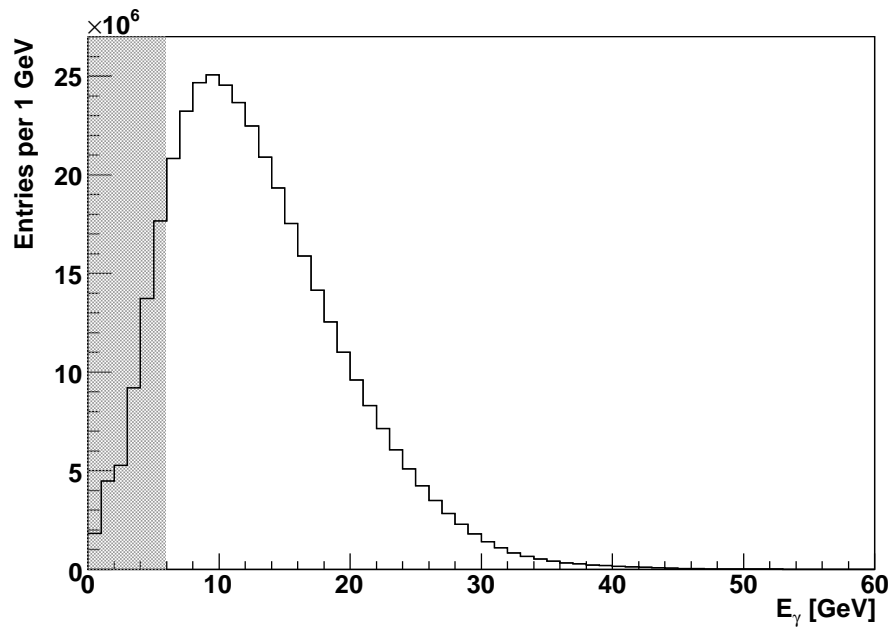


Figure 8.6: Energy of the photon candidates. The shadowed area contains clusters not accepted as photon candidates.

8.1.3 Selection of Pion Shower Clusters

Events with extra clusters other than the two photons were accepted only if the clusters could be assigned to the pion shower.

- **Maximum distance to the pion in the LKr calorimeter.** As shown in Fig. 8.4, the pion shower is mostly realized inside a radius of 30 cm from the pion track impact point in the LKr. Clusters with $d_{\pi-cluster} < 30$ cm were assigned to the pion shower.
- **Time difference between the pion track and the pion clusters in the LKr.** Clusters from the pion shower had to belong to the same event, $\Delta t_{\pi-cluster} < 6$ ns.

8.2 Event Reconstruction

After the pre-selection cuts, all particles belonging to the event were already identified and global event variables could be calculated. In the following sections some of these variables are introduced.

8.2.1 Energy Center of Gravity (COG)

The energy center of gravity of the event is the sum of the energy weighted positions of the decay products in the LKr calorimeter. It can be expressed as:

$$COG = \sqrt{COG_x^2 + COG_y^2}, \quad (8.2.1)$$

with

$$COG_x = \frac{\sum_i E_i \cdot x_i}{\sum_i E_i}, \quad COG_y = \frac{\sum_i E_i \cdot y_i}{\sum_i E_i}, \quad (8.2.2)$$

and where E_i is the energy of each particle, and x_i, y_i are its coordinates at the front face of the LKr. The pion energy is $E_\pi = \sqrt{m_\pi^2 + p_\pi^2}$, with p_π measured in the spectrometer and $m_\pi = m_{\pi^\pm} = 139.57$ MeV/ c^2 [108]. The position of the pion at the LKr is obtained by extrapolating its line of flight from the DCHs located before the magnet to the front face of the LKr, i.e. considering no deviation introduced by the magnet in the spectrometer. Figure 8.7 shows a schematic view with the relevant information needed to calculate the center of gravity of one event.

For a fully reconstructed event, the center of gravity position should coincide with the point where the kaon would have hit the LKr calorimeter if it had not decayed, i.e, around the center of the beam pipe (the COG is never exactly 0 due to the finite cross section of the beam).

decays into a pion and two photons, $z_{vertex}^{neutral}$ can be calculated from the kaon mass as follows:

$$m_K^2 = E_K^2 - p_K^2 = m_\pi^2 + 2E_\pi E_{\gamma_1} + 2E_\pi E_{\gamma_2} - 2p_\pi p_{\gamma_1} \cos(\widehat{\pi\gamma_1}) - 2p_\pi p_{\gamma_2} \cos(\widehat{\pi\gamma_2}) + 2E_{\gamma_1} E_{\gamma_2} [1 - \cos(\widehat{\gamma_1\gamma_2})], \quad (8.2.3)$$

and for small angles⁴:

$$m_K^2 \approx m_\pi^2 + 2(E_{\gamma_1} + E_{\gamma_2})(E_\pi - p_\pi) + p_\pi E_{\gamma_1} \frac{d_{\pi-\gamma_1}^2}{d^2} + p_\pi E_{\gamma_2} \frac{d_{\pi-\gamma_2}^2}{d^2} + E_{\gamma_1} E_{\gamma_2} \frac{d_{\gamma_1-\gamma_2}^2}{d^2}, \quad (8.2.4)$$

with $d = z_{LKr} - z_{vertex}^{neutral}$, z_{LKr} the z -position of the LKr front plane, $d_{\gamma_1-\gamma_2}$ the distance between the two photon clusters, and $d_{\pi-\gamma_i}$ the distance between the i^{th} -photon and the pion at the LKr assuming no deviation of the pion trajectory after traversing the magnetic spectrometer. Finally, reordering Eq. 8.2.4 and inserting the kaon and pion masses:

$$z_{vertex}^{neutral} = z_{LKr} - \sqrt{\frac{p_\pi E_{\gamma_1} d_{\pi-\gamma_1}^2 + p_\pi E_{\gamma_2} d_{\pi-\gamma_2}^2 + E_{\gamma_1} E_{\gamma_2} d_{\gamma_1-\gamma_2}^2}{m_K^2 - m_\pi^2 - 2(E_{\gamma_1} + E_{\gamma_2})(E_\pi - p_\pi)}}, \quad (8.2.5)$$

with E_π the pion energy as defined in Section 8.2.1.

8.2.3 Invariant Mass of the Di-Photon System

The invariant mass of the di-photon system is obtained using the knowledge of the z_{vertex} position and the energies and positions of the photon clusters at the LKr as:

$$\begin{aligned} m_{\gamma_1\gamma_2}^2 &= m_{\gamma_1}^2 + m_{\gamma_2}^2 + 2E_{\gamma_1} E_{\gamma_2} - 2\vec{p}_{\gamma_1} \vec{p}_{\gamma_2} \\ &= 2E_{\gamma_1} E_{\gamma_2} - 2p_{\gamma_1} p_{\gamma_2} \cos(\widehat{\gamma_1\gamma_2}) \\ &= 2E_{\gamma_1} E_{\gamma_2} (1 - \cos(\widehat{\gamma_1\gamma_2})), \end{aligned} \quad (8.2.6)$$

or equivalently (at small angles):

$$m_{\gamma_1\gamma_2} \approx \frac{1}{z_{LKr} - z_{vertex}} \sqrt{E_{\gamma_1} E_{\gamma_2} (\vec{r}_{\gamma_1} - \vec{r}_{\gamma_2})^2}. \quad (8.2.7)$$

⁴Given the large distances between the decay region and the LKr, this approximation always holds.

8.3 Decay Vertex Region

The decay region was defined as the region with $-1800 \text{ cm} < z_{vertex} < 7000 \text{ cm}$. The low z_{vertex} limit excludes kaon decays produced in the last collimator and particles deflected at its edges, while the upper limit avoids kaon decays produced too close to the detector.

8.4 Background Sources

After the pre-selection conditions have been applied, four kinds of background channels can be present in the signal data sample. Table 8.1 summarizes these decays channels.

Decay Channel	Branching Ratio
$K^\pm \rightarrow \pi^\pm \pi^0$	$(20.65 \pm 0.09)\%$ [4]
$K^\pm \rightarrow \pi^\pm \pi^0 \pi^0$	$(1.757 \pm 0.024)\%$ [108]
$K^\pm \rightarrow \pi^\pm \pi^0 \gamma$ (IB)	$(2.75 \pm 0.15) \cdot 10^{-4}$ [108]
$K^\pm \rightarrow \pi^\pm \pi^0 \gamma$ (DE)	$(4.4 \pm 0.7) \cdot 10^{-6}$ [108]
$K^\pm \rightarrow \pi^\pm \pi^0 \gamma$ (INT)	$-(5.8 \pm 2.4) \cdot 10^{-6}$ [97, 67]

Table 8.1: Summary of background channels with a $K^\pm \rightarrow \pi^\pm \gamma \gamma$ -signature. The branching ratios for the $K^\pm \rightarrow \pi^\pm \pi^0 \gamma$ IB, DE and INT channels correspond to the kinematic region with pion kinetic energy in the kaon rest frame of $55 \text{ MeV} < T_{\pi^\pm}^{CM} < 90 \text{ MeV}$. The NA48/2 2003 preliminary results on the interference component fractions were used for the $\text{BR}(K^\pm \rightarrow \pi^\pm \pi^0 \gamma)$ INT.

8.4.1 $K^\pm \rightarrow \pi^\pm \pi^0$

$K^\pm \rightarrow \pi^\pm \pi^0$ decays have exactly the same signature as $K^\pm \rightarrow \pi^\pm \gamma \gamma$ events, with the only difference that the di-photon invariant mass is equal to the π^0 mass. Background from this channel was eliminated online by the MFAKE trigger (Section 6.4.1) and the remaining π^0 tails in the offline analysis by requiring $m_{fake} < 460 \text{ MeV}/c^2$.

8.4.2 $K^\pm \rightarrow \pi^\pm \pi^0 \pi^0$

The different ways in which $K^\pm \rightarrow \pi^\pm \pi^0 \pi^0$ decays can reproduce the $K^\pm \rightarrow \pi^\pm \gamma \gamma$ -signature are summarized in Fig. 8.8. Except for the case where two photons from different π^0 decays overlap together (Fig. 8.8 up left), all the other cases have missing energy because one of the photons (in the case of Fig. 8.8 up right) or two of them (Fig. 8.8 down) missed the detector acceptance or did not pass the pre-selection cuts.

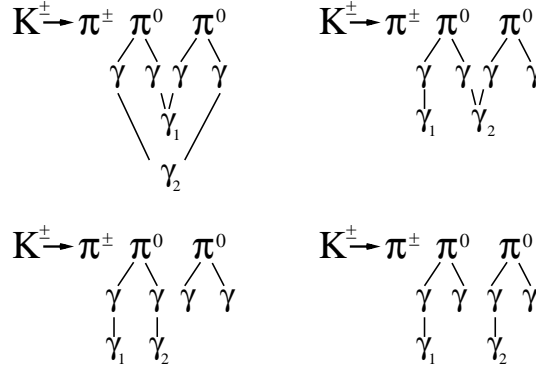


Figure 8.8: Scheme of the possible ways of obtaining a $K^\pm \rightarrow \pi^\pm \gamma_1 \gamma_2$ -signature from $K^\pm \rightarrow \pi^\pm \pi^0 \pi^0$ decays.

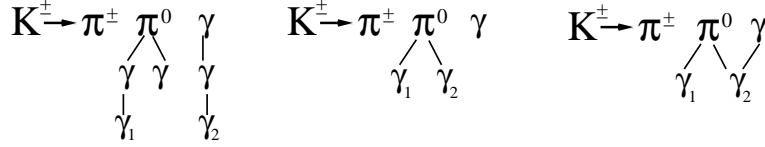


Figure 8.9: Scheme of three possible ways of creating a $K^\pm \rightarrow \pi^\pm \gamma_1 \gamma_2$ -signature from $K^\pm \rightarrow \pi^\pm \pi^0 \gamma$ decays.

8.4.3 $K^\pm \rightarrow \pi^\pm \pi^0 \gamma$

There are three different $K^\pm \rightarrow \pi^\pm \pi^0 \gamma$ decay channels:

- $K^\pm \rightarrow \pi^\pm \pi^0 \gamma$ IB. In these decays, the odd photon is emitted from the charged pion in the same direction of flight as the pion, and with a soft bremsstrahlung energy spectrum.
- $K^\pm \rightarrow \pi^\pm \pi^0 \gamma$ DE. In this case, the odd photon is directly emitted from the kaon decay vertex and has the corresponding energy spectrum of a particle from a three body decay.
- $K^\pm \rightarrow \pi^\pm \pi^0 \gamma$ INT. This channel is the result of the interference between IB and DE decays.

The different ways in which $K^\pm \rightarrow \pi^\pm \pi^0 \gamma$ decays can produce a $K^\pm \rightarrow \pi^\pm \gamma \gamma$ -signature are summarized in Fig. 8.9. Like for $K^\pm \rightarrow \pi^\pm \pi^0 \pi^0$ decays, except for the case where the odd photon overlaps with one of the π^0 photons (Fig. 8.9 right), the other two cases (Fig. 8.9 left and middle) have missing energy because one of the photons missed the detector acceptance or did not pass the pre-selection. Events with a very soft odd photon were rejected by the MFAKE trigger together with $K^\pm \rightarrow \pi^\pm \pi^0$ decays.

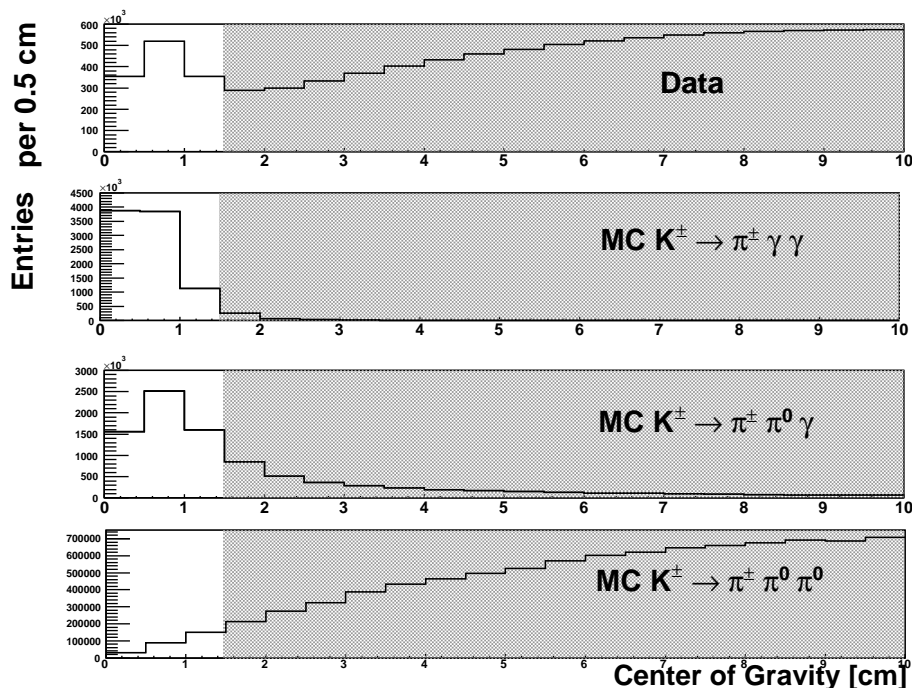


Figure 8.10: *COG* distributions for data and MC $K^\pm \rightarrow \pi^\pm \gamma \gamma$, MC $K^\pm \rightarrow \pi^\pm \pi^0 \gamma$, and MC $K^\pm \rightarrow \pi^\pm \pi^0 \pi^0$ events. The shadowed area shows the rejected region. The plots are arbitrarily normalized.

8.5 Background Rejection

The following cuts were applied to reduce the background from the data sample:

- Center of gravity.** As explained in the previous section, some of the background events passing the pre-selection criteria have one or more decay photons not selected as photon candidates, and therefore have missing energy. Figure 8.10 shows the *COG* distributions for data, MC $K^\pm \rightarrow \pi^\pm \gamma \gamma$ decays, MC $K^\pm \rightarrow \pi^\pm \pi^0 \gamma$ IB decays, and MC $K^\pm \rightarrow \pi^\pm \pi^0 \pi^0$ decays. The higher the missing energy not reconstructed, the broader the *COG* distribution. Events with *COG* larger than 1.5 cm were rejected from the data sample.
- Difference between charged and neutral vertex.** This cut is complementary to the previous one. It relies on the fact that if not all the energy is measured, the 'neutral' vertex is shifted with respect to the 'charged' vertex, since the kaon is no longer reconstructed. Figure 8.11 shows the difference between the charged and the neutral vertex for data, MC $K^\pm \rightarrow \pi^\pm \gamma \gamma$ decays, MC $K^\pm \rightarrow \pi^\pm \pi^0 \gamma$ IB decays and MC $K^\pm \rightarrow \pi^\pm \pi^0 \pi^0$ decays. Note that the $COG < 1.5$ cm requirement was

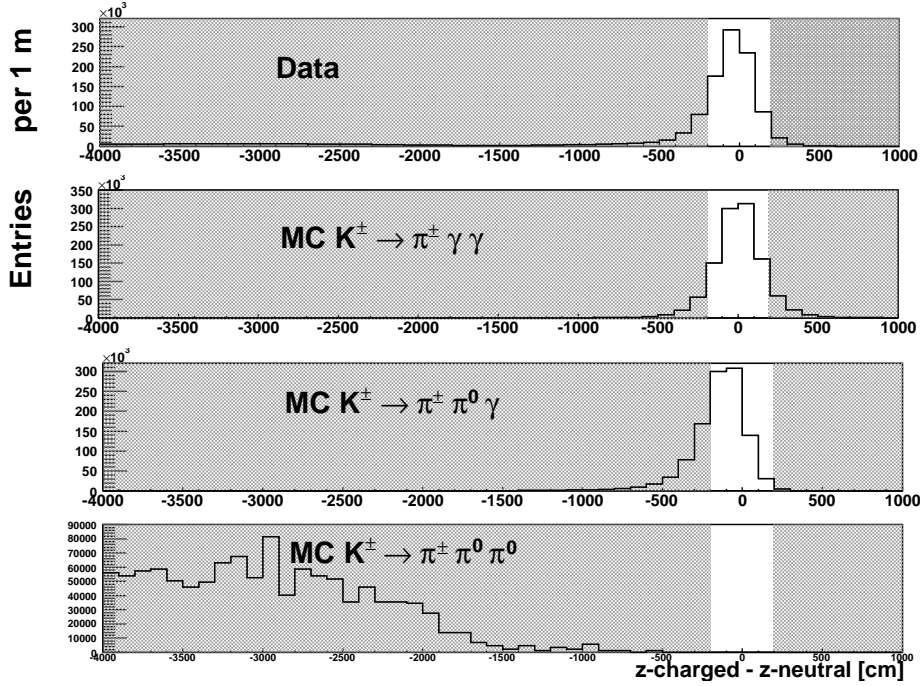


Figure 8.11: Difference between the charged and the neutral vertex for data and MC $K^\pm \rightarrow \pi^\pm \gamma \gamma$, $K^\pm \rightarrow \pi^\pm \pi^0 \gamma$, and $K^\pm \rightarrow \pi^\pm \pi^0 \pi^0$ events. The plots are arbitrarily normalized.

already applied. A cut on $|z_{charged} - z_{neutral}| > 200$ cm was applied to further remove missing energy background.

- **Total energy of the event.** To eliminate the remaining $K^\pm \rightarrow \pi^\pm \pi^0 \gamma$ decays with missing energy not rejected by the previous cuts, the total energy of the event was required to be $55 \text{ GeV} < E_K = E_\pi + E_{\gamma_1} + E_{\gamma_2} < 65 \text{ GeV}$.
- **Shower width.** To remove background events with overlapping showers, a cut was applied in the total shower width. The shower width, r_{rms} , is defined as the radial spread of an LKr shower:

$$r_{rms} = \sqrt{RMS_x^2 + RMS_y^2}, \quad (8.5.1)$$

with $RMS_{x,y}$ the radial spread in the x and y -directions measured in cell units, i.e. in units of 2 cm. Since the shower width of low energetic particles is wider than for high energetic particles, a cut on the width must be done as a function of the energy.

To define the width of a single shower, photons from π^0 decays of selected $K^\pm \rightarrow \pi^\pm \pi^0$ events were studied⁵. The energy of a photon was divided in

⁵The studied $K^\pm \rightarrow \pi^\pm \pi^0$ decays were selected from data with the NTPEAK trigger set, using

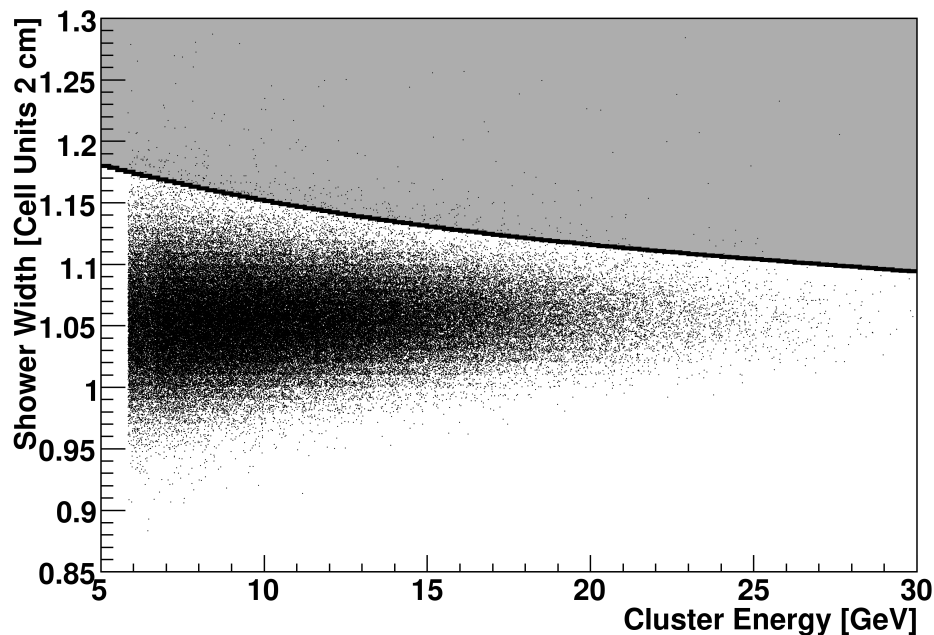


Figure 8.12: Shower width in the LKr vs. the cluster energy. The shadowed region represents the cut against overlapping showers.

	p_0	p_1	p_2	p_3
$K^\pm \rightarrow \pi^\pm \pi^0$ Data	1.22	-0.009	0.00025	$-3 \cdot 10^{-6}$
$K^\pm \rightarrow \pi^\pm \pi^0$ MC	1.2	-0.0075	0.0002	$-1.95 \cdot 10^{-6}$

Table 8.2: Parameters of the fit to the maximum single shower width.

20 bins of 2 GeV each, and a gaussian fit was performed to the r_{rms} in each bin. An upper limit for the shower width was then defined as the mean of the gaussian plus three times its width. In this way, each one of the 20 bins defined an upper limit for the shower width of a single photon. A polynomial function with three powers of E_γ was then fitted to the 20 values. The result of this fit is shown in Figure 8.12 for the remaining data. Events containing showers with r_{rms} above the fit line were rejected.

The same procedure was repeated to determine the shower width cut for MC events by using MC $K^\pm \rightarrow \pi^\pm \pi^0$ decays. The results of the polynomial fit can be found in Table 8.2.

the same selection criteria as for the signal plus an additional π^0 mass requirement on the di-photon mass, $0.13 \text{ GeV}/c^2 < m_{\gamma\gamma} = m_{\pi^0} < 0.14 \text{ GeV}/c^2$ (Sec. 8.8).

- **Interactions in DCH1 inner radius.** Reconstructed events with high z -decay vertices might have a photon interacting with the flange surrounding the beam pipe hole at DCH1. In this case, the photon can make a shower before reaching the electromagnetic calorimeter. These kind of showers is not well simulated in the Monte Carlo and lead to a disagreement with the data. Knowing the position of the photon clusters at the LKr and the reconstructed z -vertex of the event, the distance of the photons at DCH1 can be calculated. Events with a photon with a radial position at DCH1 compatible with the radius of the flange, $r_{flange}^{DCH1} < 11$ cm were rejected.
- **Trigger requirements.** The trigger cuts applied online to the data during the data taking were enforced and applied also to the MC simulation. This is needed to have a reliable acceptance description from the MC and to improve trigger efficiencies by avoiding trigger edge effects.
 - **The m_{fake} condition.** Data events selected through the MFAKE trigger had an online trigger cut on $m_{fake} < 475$ MeV/ c^2 . This cut was enforced to $m_{fake} < 460$ MeV/ c^2 and applied also to the MC simulated events for signal and background channels. Note that this cut was not applied to the normalization channel events, since they are selected through the NTPEAK trigger.
 - **The distance between NTPEAK clusters.** As explained in Chapter 6, the NTPEAK trigger required more than two energy peaks in at least one of the LKr projections. A good separation of the reconstructed clusters is therefore needed to increase the efficiency of this trigger. The minimum distance between each pair of the reconstructed clusters (γ_1 - γ_2 , $\gamma_1 - \pi$ and $\gamma_2 - \pi$) in at least one of the LKr projections was asked to be greater than 10 cm ($max(d_x^{min}, d_y^{min}) > 10$ cm); this cut is explained in detail in Section 9.2.1. Since during the super sample 2 and super sample 3 periods the NTPEAK trigger was only working for the x -projection of the LKr, the applied cut for these periods was $d_x^{min} > 10$ cm for all events, thus reducing the acceptance of the events during these periods in comparison with super sample 1. This requirement was applied to both data events and MC simulation.

8.6 Corrections

A set of corrections were applied to MC and data events at several stages of the reconstruction:

Correction	Data	Monte Carlo
Blue Tube Field	✓	✓
DCH Alpha and Beta	✓	✓
LKr Projectivity	✓	✓
LKr Non-Linearity	✓	✓
LKr Energy Scale	✓	X
Non-gaussian tails	X	✓
Trigger efficiency	X	✓

Table 8.3: Corrections summary (\checkmark = applied, X = not applied).

- Blue tube field.** Due to both a remanent magnetic field in the decay region and the earth magnetic field (Section 4.2), the direction of the charged pion track measured at the first DCHs was not the same as its direction at the decay vertex. The blue tube field bent the track, changing its direction along its path in the decay volume. The strength of this field was studied in detail by the NA48/2 collaboration and was measured to be about 100 μT , depending on the position in the decay volume [66]. To account for this effect, the integral of the blue tube field was computed in iterative steps, using the measured magnetic field maps both for data and MC events, providing in every point new values for the track slopes. The value of these slopes at the vertex defined the pion four momenta and were used for invariant mass computations.
- DCH alpha and beta.** During the analysis of $K^\pm \rightarrow \pi^\pm \pi^+ \pi^-$ events collected during the 2003 data taking, the NA48/2 collaboration observed that the reconstructed kaon masses were different for K^+ and K^- events, and that both were different from the nominal kaon mass. Such effects arose from imperfections in the momentum measurement by the magnetic spectrometer. A model was built [41], assuming only two sources affecting the reconstructed momenta: miscalibration of the spectrometer magnetic field, and misalignment of one of the DCHs located downstream the magnet.
 - Misalignment of DCH4.** A relative misalignment of DCH4 with respect to the DCHs located before the magnet affected the measurement of the deflections of charged particles in the plane of the transverse kick, implying therefore a momentum mismeasurement. For a given magnet polarity, this mismeasurement depended on the

charge of the particle, as tracks of opposite charges are deflected in opposite directions. Since the K^+ was reconstructed from two positive and one negative track, its mass was shifted in opposite direction compared to the K^- , which was reconstructed from one positive and two negative tracks. The corresponding momentum correction, p_{corr} , was parameterized as:

$$p_{corr} = p \cdot (1 + \alpha \cdot q) \text{ [GeV}/c], \quad (8.6.1)$$

with

$$\alpha = -\text{sign}(B)(\langle m_{K^+} \rangle - \langle m_{K^-} \rangle)/1.7476, \quad (8.6.2)$$

and q being the charge of the reconstructed track, p the reconstructed momentum of the track before the correction, and $\text{sign}(B)$ the polarization of the magnet in the spectrometer.

The value of α changed every run, for this reason the values $\langle m_{K^-} \rangle$ and $\langle m_{K^+} \rangle$ represent the mean values for the kaon masses measured during one burst. The values of α for the 2003 run were at worst about -10^{-4} , corresponding to a shift in the reconstructed kaon mass of about $0.35 \text{ MeV}/c^2$.

- **Miscalibration of the spectrometer field.** This effect was responsible for a shift with respect to the nominal kaon mass of the reconstructed measured values. Since $\frac{\Delta B}{B} = \frac{\Delta p}{p}$, a miscalibration of the field in the spectrometer induced a momentum misreconstruction. For $K^\pm \rightarrow \pi^\pm \pi^+ \pi^-$ events, this lead to a mismeasurement of the reconstructed kaon mass value m_K^{meas} of:

$$(m_K^{meas} - m_K^{nom})/m_K^{nom} \approx 0.2 \cdot \Delta B/B. \quad (8.6.3)$$

The momentum measured by the spectrometer was corrected for this effect by defining:

$$\beta = \frac{\Delta B}{B} = \frac{m_K^{nom} - \langle m_K \rangle}{0.2 \cdot m_K^{nom}}, \quad (8.6.4)$$

where m_K^{nom} is the nominal kaon mass, while $\langle m_K \rangle$ is the measured mass after applying the α correction. The corrected momentum p_{corr} was given by:

$$p_{corr} = p \cdot (1 + \beta) \text{ [GeV}/c], \quad (8.6.5)$$

with p the uncorrected momentum.

A typical value of the β correction was about -10^{-3} , corresponding to a $\approx 500 \text{ keV}/c^2$ shift on the reconstructed kaon mass.

The alpha and beta corrections were evaluated on a burst per burst basis, and the obtained results stored in a database which was also used in the MC simulation in order to reproduce there the observed distortions in data. The overall correction was accurate to a few keV/c^2 .

- **LKr projectivity.** The projectivity correction was applied in order to provide the best estimate for the photon coordinates at the LKr. The cells of the LKr calorimeter had a projective geometry, pointing to the z -axis decay region at 110 m away from the calorimeter front face. The x -, y -cluster positions given by the NA48/2 standard reconstruction program were extrapolated to the calorimeter front face, assuming that the shower had developed along the projective direction. However, when the photon was produced at a position different from the projective point, this assumption no longer held and a correction to the cluster transverse position needed to be applied.

The angle θ of the shower development with respect to the projective direction was calculated knowing the distance z of the actual decay position from the projective point (z_0) and the approximate shower transverse position at the calorimeter front (x):

$$\theta = x \cdot \left(\frac{1}{z_0 - z} - \frac{1}{z_0} \right) \quad (8.6.6)$$

For a given photon shower energy E_γ , the shower depth inside the LKr structure was calculated as [101, 102]:

$$z_{depth} = 20.8 + 4.3 \cdot \log(E_\gamma[\text{GeV}]) \text{ [cm]} \quad (8.6.7)$$

The x -, y -clusters positions at the LKr front face were then modified according to the measured particle direction as:

$$x_{corr} = x_{standard} \cdot (1 + \theta \cdot z_{depth}) \quad (8.6.8)$$

For a photon shower coming from a decay 50 m away from the projective point position and with a shower depth of 30 cm, the amount of this correction was of the order of 5 mm (≈ 5 per mil). The projectivity correction needed to be applied, since otherwise the reconstructed π^0 mass would depend on the decay point along the beam axis. The projective LKr geometry was also implemented in the simulation.

- **LKr non-linearity.** Due to the data concentrator threshold applied to the LKr calorimeter cells at the readout, a non-linear relation developed between the value of the energy deposited in the calorimeter and its actual value. Using $K_S \rightarrow \pi^0\pi^0$ decays from the 2002 run, a correction was developed to be applied to clusters with energies smaller than 11 GeV.

This was also used for the 2003 data, since the data concentrator threshold was kept at the same value as in 2002. This correction was applied to the MC simulation too. The effect of this correction was only significant for cluster energies of about 3 GeV, which were not considered in this analysis.

- **Energy scale.** The absolute energy scale factor of the electromagnetic calorimeter was measured in special runs where $\eta \rightarrow 2\gamma$ and $\eta \rightarrow 3\pi^0$ decays were studied. This factor was known to a precision of $\sim 0.1\%$ and is crucial for the correct reconstruction of the photon clusters. This effect was studied as a systematic effect in the measurement (Section 11.4).
- **Non gaussian tails.** In order to improve the agreement between data and MC, a correction was applied only to simulated events reproducing the non-gaussian tails in the energy resolution of the LKr produced in hadronic showers. The total probability and the parametrization of the energy loss as a function of the photon energy was extracted from neutral semi-leptonic data [25].
- **Trigger efficiency.** Trigger efficiency corrections simulating the effect of the trigger on the data were applied to the MC simulation after the reconstruction and selection of events (see Chapter 9).

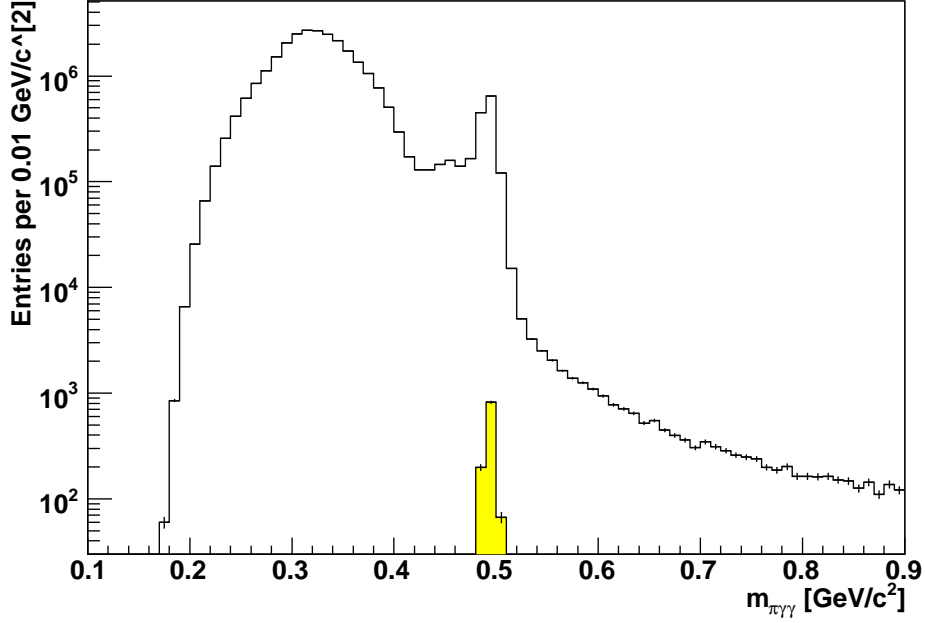


Figure 8.13: Reconstructed kaon invariant mass of the pre-selected (black histogram) and selected (yellow area) $K^\pm \rightarrow \pi^\pm \gamma\gamma$ events.

8.7 Selection of $K^\pm \rightarrow \pi^\pm \gamma\gamma$ Decays

After all selection requirements summarized in Table 8.5, 908 $K^\pm \rightarrow \pi^\pm \gamma\gamma$ candidates collected from the MFAKE trigger were selected. The number of events selected in the different super samples is summarized in Table 8.4. The remaining background contamination is estimated in Section 11.2. This background amounts to about 8% of the total number of selected candidates, and is mainly composed of $K^\pm \rightarrow \pi^\pm \pi^0 \gamma$ IB decays with an overlap of the odd photon and one of the photons from the π^0 decay, so that the π^0 mass is no longer reconstructed.

The number of selected signal events at different stages of the selection is shown in Table 8.6 for both data and Monte Carlo signal with $\hat{c} = 1.74$. The effects of the same cuts on the simulated background channels are shown in Table 8.7. Time cuts were not applied in the MC events. Figure 8.13 shows the reconstructed kaon invariant mass with only pre-selection criteria being applied (black histogram) and after all cuts (yellow area). Figures 8.15 and 8.16 show, respectively, the kaon invariant mass and the di-photon invariant mass of the selected $K^\pm \rightarrow \pi^\pm \gamma\gamma$ candidates. Note that the L2 trigger cut on m_{fake} , limited the available di-photon mass region to $m_{\gamma\gamma} > 0.2 \text{ GeV}/c^2$, as explained in Section 6.4.1. A comparison between data and Monte Carlo $K^\pm \rightarrow \pi^\pm \gamma\gamma$ events after trigger efficiency corrections is shown in Chapter 10.

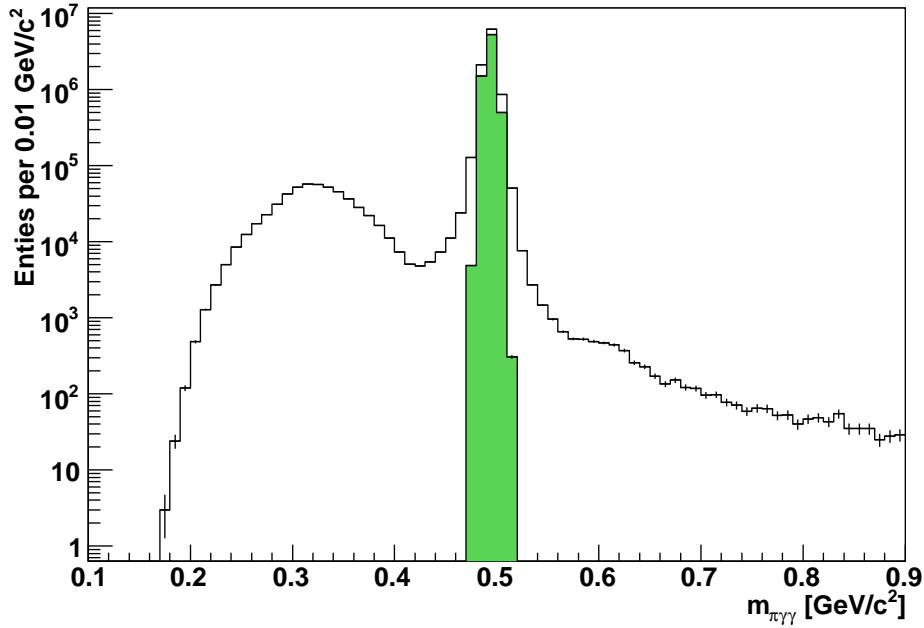


Figure 8.14: Reconstructed kaon invariant mass of the pre-selected (black histogram) and selected (green area) $K^\pm \rightarrow \pi^\pm \pi^0$ events.

8.8 Selection of $K^\pm \rightarrow \pi^\pm \pi^0$ Decays

About 5,750,121 $K^\pm \rightarrow \pi^\pm \pi^0$ decays used as a normalization channel were collected from the L2 NTPEAK trigger after all the selection requirements (Table 8.5). The amount of collected events in the different super sample periods is summarized in Table 8.4.

All selection criteria applied to the $K^\pm \rightarrow \pi^\pm \gamma \gamma$ signal were also applied to the $K^\pm \rightarrow \pi^\pm \pi^0$ normalization channel, with the exception of the $m_{fake} < 460$ MeV/ c^2 cut. Instead, the di-photon invariant mass had to meet the requirement that 0.13 GeV/ $c^2 < m_{\gamma\gamma} = m_{\pi^0} < 0.14$ GeV/ c^2 , to select events with a π^0 in the final state.

Background contributions to this channel were found to be negligible. The number of selected $K^\pm \rightarrow \pi^\pm \pi^0$ events at different stages of the selection is shown in Table 8.6 for both data and Monte Carlo events. Figure 8.14 shows the reconstructed kaon invariant mass with only pre-selection criteria being applied (black histogram) and after all cuts (green area). Figures 8.17 and 8.18 show, respectively, the kaon invariant mass and the di-photon invariant mass of the selected $K^\pm \rightarrow \pi^\pm \pi^0$ data. A comparison between data and Monte Carlo $K^\pm \rightarrow \pi^\pm \pi^0$ events after trigger efficiency corrections is shown in Chapter 10.

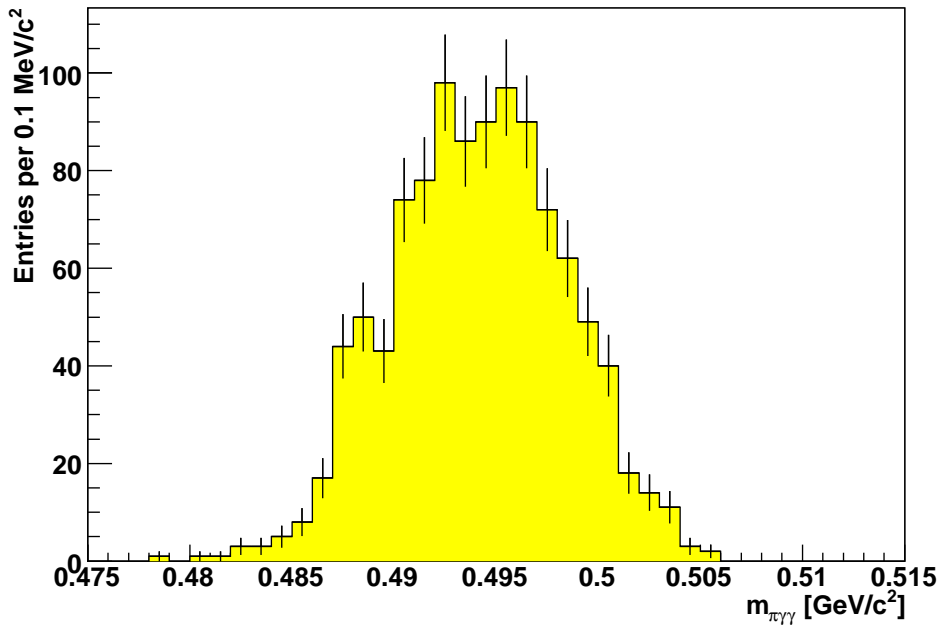


Figure 8.15: Reconstructed kaon invariant mass of the selected $K^{\pm} \rightarrow \pi^{\pm}\gamma\gamma$ events.

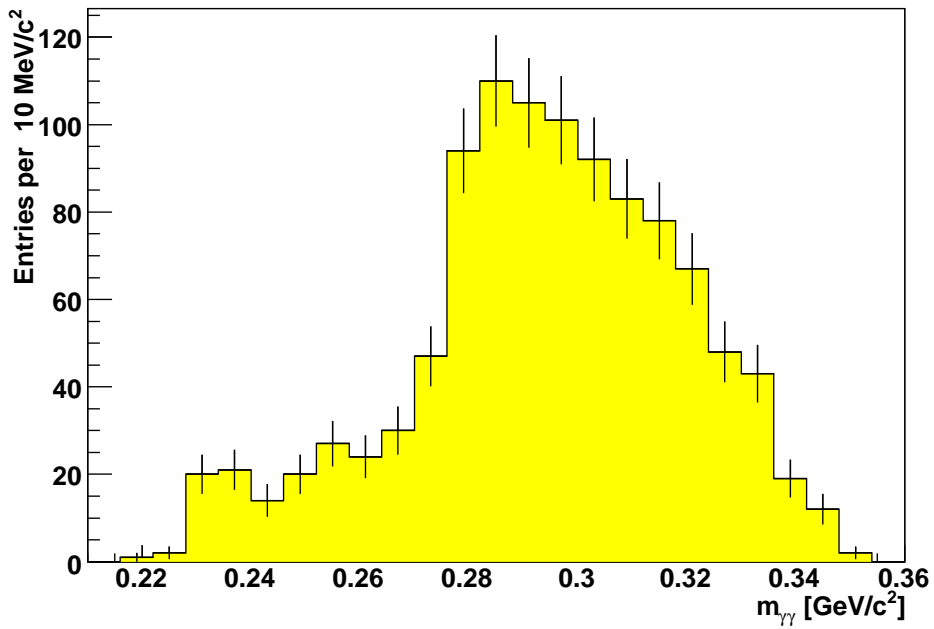
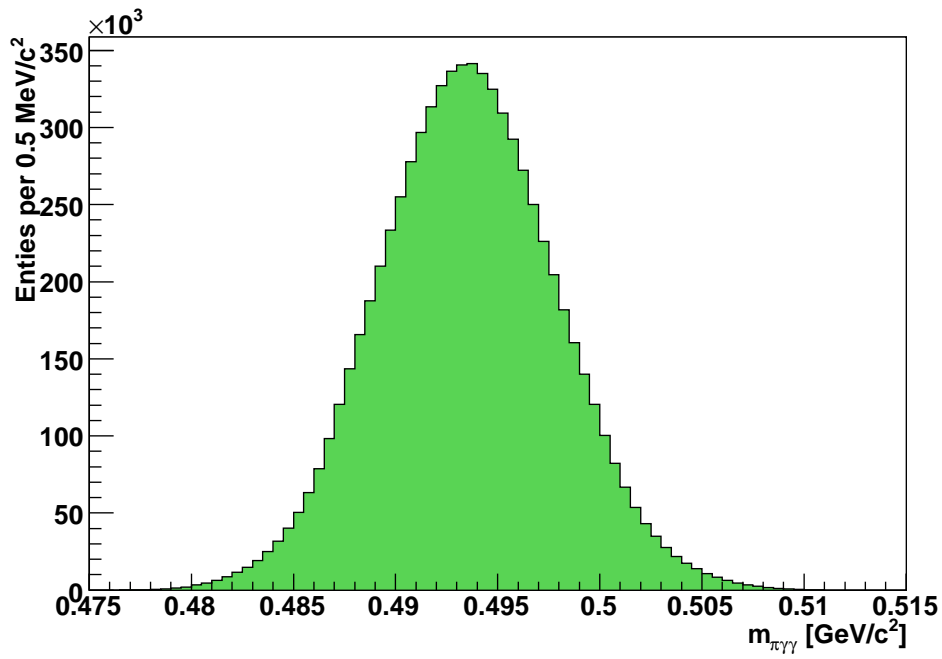
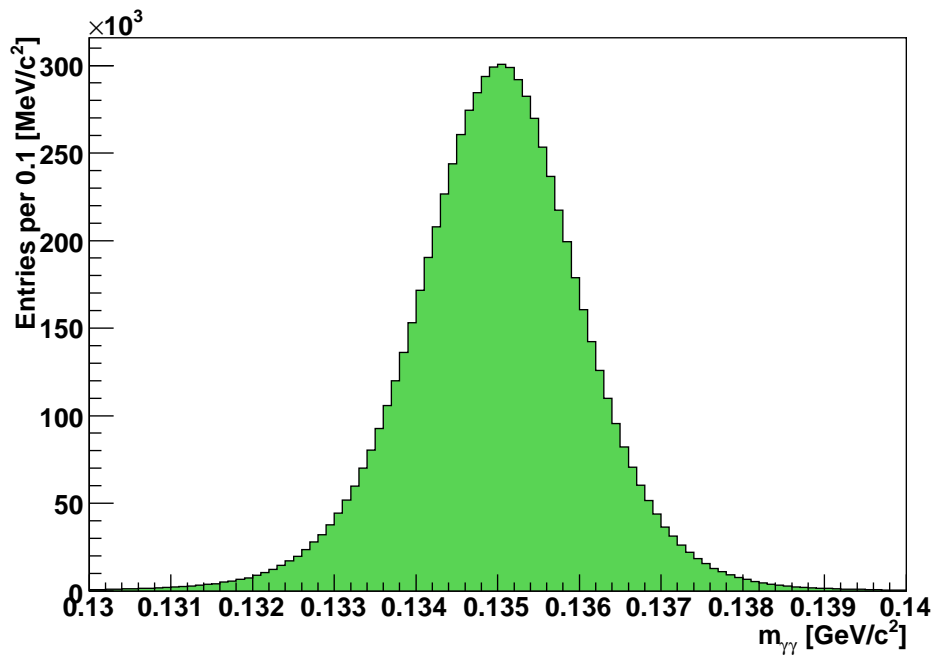


Figure 8.16: Reconstructed di-photon invariant mass of the selected $K^{\pm} \rightarrow \pi^{\pm}\gamma\gamma$ events.

Figure 8.17: Reconstructed kaon invariant mass of the selected $K^\pm \rightarrow \pi^\pm \pi^0$ events.Figure 8.18: Reconstructed di-photon invariant mass of the selected $K^\pm \rightarrow \pi^\pm \pi^0$ events.

Period	$K^\pm \rightarrow \pi^\pm \gamma \gamma$ Candidates	$K^\pm \rightarrow \pi^\pm \pi^0$ Candidates
SS1	337	2006413
SS2	418	2734139
SS3	153	1009569

Table 8.4: Selected signal and normalization data in the different super samples.

Pre-Selection Criteria	
Pion Selection	
Number of Tracks	1
Momentum	$p_\pi > 10 \text{ GeV}/c$
Distance to Beam Pipe (I)	$15 \text{ cm} < r_\pi^{DCH1,2,3} < 120 \text{ cm}$
Distance to Beam Pipe (II)	$15 \text{ cm} < r_\pi^{DCH4,LKr} < 113 \text{ cm}$
Distance to LKr Dead Cells	$d_{track-dead\ cell} > 2 \text{ cm}$
Particle Identification (I)	$E/p < 0.8 \text{ c}$
Particle Identification (II)	No Hit in MUV
Photons Selection	
Distance to LKr Dead Cells	$d_{\gamma-dead\ cell} > 2 \text{ cm}$
Distance to LKr Clusters	$d_{\gamma-cluster} > 10 \text{ cm}$
Distance to Pion at LKr	$d_{\pi-\gamma} > 30 \text{ cm}$
Time Difference with Pion (*)	$ \Delta t_{\pi-\gamma} = t_\pi^{DCH} - t_\gamma^{LKr} < 6 \text{ ns}$
Time Difference between Photons (*)	$ \Delta t_{\gamma_1-\gamma_2} = t_{\gamma_1}^{LKr} - t_{\gamma_2}^{LKr} < 6 \text{ ns}$
Distance to Beam Pipe	$15 \text{ cm} < r_\gamma^{LKr} < 113 \text{ cm}$
Photon Energy	$E_\gamma > 6 \text{ GeV}$
Extra Clusters	
Distance to Pion at LKr	$d_{\pi-cluster} > 30 \text{ cm}$
Time Difference with Pion (*)	$ \Delta t_{\pi-cluster} = t_\pi^{DCH} - t_{cluster}^{LKr} < 6 \text{ ns}$
Acceptance Region and Background Rejection Criteria	
Decay Vertex Region	$-1800 \text{ cm} < z_{vertex}^{charged} < 7000 \text{ cm}$
Energy Center of Gravity	$COG < 1.5 \text{ cm}$
Closest Distance of Approach K- π	$cda < 3 \text{ cm}$
Vertex Difference	$ z_{vertex}^{charged} - z_{vertex}^{neutral} < 200 \text{ cm}$
Event Total Energy	$55 \text{ GeV} < E_{tot} < 65 \text{ GeV}$
Photon Shower Width (DATA)	$r_{rms} < 1.22 - 9 \cdot 10^{-3} \cdot E_\gamma + 2.5 \cdot 10^{-4} \cdot E_\gamma^2$
Photon Shower Width (MC)	$r_{rms} < 1.20 - 7.5 \cdot 10^{-3} \cdot E_\gamma + 2 \cdot 10^{-4} \cdot E_\gamma^2$
Photon Interactions with DCH1	$r_{flange}^{DCH1} > 11 \text{ cm}$
MFAKE Trigger (Signal)	$m_{fake} < 460 \text{ MeV}/c^2$
Neutral Pion Mass (Normalization)	$0.13 \text{ GeV}/c^2 < m_{\gamma\gamma} = m_{\pi^0} < 0.14 \text{ GeV}/c^2$
NTPEAK Trigger	$max(d_x^{min}, d_y^{min}) > 10 \text{ cm}$

Table 8.5: Summary of selection criteria used for the reconstruction of $K^\pm \rightarrow \pi^\pm \gamma \gamma$ and $K^\pm \rightarrow \pi^\pm \pi^0$ decays. (*) Time cuts were not applied to Monte Carlo events.

Condition	$\pi^\pm \gamma \gamma$		$\pi^\pm \pi^0$	
	Data	MC	Data	MC
Initial Entries	457,983,927	9,914,382	38,216,088	8,123,123
Pre-Selection				
Pion Selection	176,602,177	6,133,598	17,993,844	5,302,080
Two Photons Selection	69,642,354	2,122,646	12,150,651	1,963,854
No Extra Clusters	49,827,674	2,074,983	11,485,221	1,899,510
Acceptance Region and Background Rejection				
$(-1800 < z_{vertex}^{charged} < 7000)$ cm	45,345,096	2,060,593	11,354,248	1,888,917
$COG < 1.5$ cm	1,626,942	1,901,372	9,854,557	1,754,828
$cda < 3$ cm	1,599,033	1,892,381	9,843,269	1,747,189
$ z_{vertex}^{charged} - z_{vertex}^{neutral} < 200$ cm	1,006,156	1,550,086	9,241,613	1,619,541
$55 \text{ GeV} < E_{tot} < 65 \text{ GeV}$	978,595	1,541,653	9,096,228	1,609,254
Shower Width	953,525	1,535,166	8,794,774	1,600,546
$r_{flange}^{DCH1} > 11$ cm	925,572	1,507,633	8,484,469	1,536,441
$m_{fake} < 460 \text{ MeV}/c^2$	1279	1,413,921	—	—
$(0.13 < m_{\gamma\gamma} < 0.14) \text{ GeV}/c^2$	—	—	8,425,376	1,525,757
$max(d_x^{min}, d_y^{min}) > 10$ cm	908	927,540	5,750,121	960,770

Table 8.6: Selected signal and normalization (data and MC) events at different stages of the selection. Signal data were collected through the L2 MFAKE trigger, while normalization events were collected through the L2 NTPEAK trigger. The cut on m_{fake} was only applied to the signal, while the $0.13 \text{ GeV}/c^2 < m_{\gamma\gamma} = m_{\pi^0} < 0.14 \text{ GeV}/c^2$ requirement was only applied to the normalization channel. The initial number of entries for the MC corresponds to the generated events in the $-1800 \text{ cm} < z_{vertex} < 7000 \text{ cm}$ decay region and with $55 < E_K < 65 \text{ GeV}$.

Condition	MC	MC $\pi^\pm\pi^0\gamma$		
	$\pi^\pm\pi^0\pi^0$	IB	DE	INT
Initial Entries ($55 \text{ GeV} < T_{\pi^\pm}^{CM} < 90 \text{ GeV}$)	92,610,008	97,351,551 (20,905,127)	10,900,966 (8,006,967)	6,469,138 (3,379,014)
Pre-Selection				
Pion Selection	48,347,670	64,408,359	7,247,173	4,331,753
Two Photons Selection	19,088,013	27,133,402	3,524,594	2,064,816
No Extra Clusters	12,512,164	20,120,175	2,830,230	1,603,220
Acceptance Region and Background Rejection				
$(-1800 < z_{vertex}^{charged} < 7000) \text{ cm}$	11,669,742	19,599,379	2,736,684	1,542,148
$COG < 1.5 \text{ cm}$	120,930	9,501,136	80,657	80,661
$cda < 3 \text{ cm}$	120,385	9,459,936	80,388	80,443
$ z_{vertex}^{charged} - z_{vertex}^{neutral} < 200 \text{ cm}$	14	6,390,059	2,462	9,954
$55 \text{ GeV} < E_{tot} < 65 \text{ GeV}$	12	6,338,345	2,441	9770
Shower width	3	6,295,402	1,170	9078
$r_{flange}^{DCH1} > 11 \text{ cm}$	3	6,024,253	1,102	8660
$m_{fake} < 460 \text{ MeV}/c^2$	3	754	587	268
$(0.13 < m_{\gamma\gamma} < 0.14) \text{ GeV}/c^2$	—	—	—	—
$max(d_x^{min}, d_y^{min}) > 10 \text{ cm}$	3	564	479	203

Table 8.7: Selected MC background events at different stages of the selection. The initial number of entries corresponds to the generated events in the $-1800 \text{ cm} < z_{vertex} < 7000 \text{ cm}$ decay region and with $55 < E_K < 65 \text{ GeV}$. The numbers in parenthesis mean the initial number of entries with $55 \text{ GeV} < T_{\pi^\pm}^{CM} < 90 \text{ GeV}$.

9 Trigger Efficiency

The neutral trigger logic in 2003 was designed to collect $K^\pm \rightarrow \pi^\pm \pi^0 \pi^0$ events with maximum efficiency and minimum systematic bias. As a consequence, the trigger chain was not optimized for the collection of $K^\pm \rightarrow \pi^\pm \gamma \gamma$ and $K^\pm \rightarrow \pi^\pm \pi^0$ decays, providing low efficiencies for these channels. The trigger efficiencies obtained for both signal and normalization channels are presented in the next sections.

9.1 Measurement of Trigger Efficiencies

The efficiency of a trigger (signal trigger) is measured with respect to another trigger (control trigger) with which it is uncorrelated. The control trigger is usually a minimum bias trigger which contains very simple requirements, not looking for a given decay signature. Once the control trigger is defined, events with the control trigger set which fulfill also the selection criteria of the decay under study are selected and referred to as control sample ($N(\text{control})$). The signal trigger condition is then checked inside the control sample by looking at the corresponding pattern units building the signal trigger. Those events are then called $N(\text{control} \cdot \text{signal})$ or efficient events.

The trigger efficiency for a given decay channel is defined as:

$$\epsilon(\text{signal}) = \frac{N(\text{control} \cdot \text{signal})}{N(\text{control})}, \quad (9.1.1)$$

with the error determined by binomial statistics.

The determination of the trigger efficiencies becomes difficult when dealing with channels with too low statistics, as is the case of $K^\pm \rightarrow \pi^\pm \gamma \gamma$ decays. To overcome this problem, an alternative method was used in this thesis. The method is based on relaxing the selection criteria, allowing background events in the control sample. The efficiency of the trigger is then measured as a function of the variables it might depend on, to avoid that the measurement depends on the channel(s) used. In this way, it is possible to calculate the trigger efficiency as a function of a set of variables, $\vec{v} = (v_1, \dots, v_n)$, using channels which have enough statistics, and weighting then by the Monte Carlo distributions of those variables for the decay for which one wants to measure the trigger efficiency:

$$\epsilon = \frac{\int N^{\text{MC}}(\vec{v}) \cdot \epsilon_{\text{control}}(\vec{v}) \cdot d\vec{v}}{N^{\text{MC}}}, \quad (9.1.2)$$

with

$$\sigma_\epsilon^2 = \frac{\int [(N^{\text{MC}}(\vec{v}) \cdot \sigma_{\epsilon_{\text{control}}}(\vec{v}))^2 + N^{\text{MC}}(\vec{v}) \cdot \epsilon_{\text{control}}^2(\vec{v})] \cdot d\vec{v}}{(N^{\text{MC}})^2} + \frac{(\int N^{\text{MC}}(\vec{v}) \cdot \epsilon_{\text{control}}(\vec{v}) \cdot d\vec{v})^2}{(N^{\text{MC}})^3}. \quad (9.1.3)$$

9.2 Trigger Efficiency of $K^\pm \rightarrow \pi^\pm \gamma \gamma$ Decays

$K^\pm \rightarrow \pi^\pm \gamma \gamma$ events accessed the MassBoX MFAKE trigger through the bit 0 of the L1 (Table 6.2):

$$(Q1+Q2) \cdot [\text{NTPEAK} + \frac{Q1}{10} \cdot \text{LKRmbias} + Q1 \cdot Q2 \cdot 1\mu \cdot \frac{\text{AKL}}{100} \cdot \text{KMU3PRE}], \quad (9.2.1)$$

built by the logical OR of three conditions, the meaning of which has already been explained in Sections 5.1.1 and 6.2. In particular, $K^\pm \rightarrow \pi^\pm \gamma \gamma$ events fired only the first two conditions in Eq. 9.2.1.

For the complete SS1, SS2 and SS3 periods it was found that 82% of the selected events fired only the NTPEAK trigger signal, 12% only the $\frac{Q1}{10} \cdot \text{LKRmbias}$ condition, and 6% both of them. Given this composition, the efficiencies of NTPEAK, $\frac{Q1}{10} \cdot \text{LKRmbias}$ and $(Q1 + Q2)$, had to be studied separately and combined to obtain the L1 trigger efficiency.

9.2.1 NTPEAK Efficiency

The NTPEAK signal was given by the logic condition of $(n_x > 2) + (n_y > 2)$, with n_x and n_y the number of peaks found by the neutral trigger system in the x -, y -projections respectively. On each projection, two calorimeter cells were read out together. The number of peaks in a given projection was given by the number of 4 cm strips firing for that particular event (Section 5.2.1).

Control Sample

The control trigger used for the trigger efficiency studies of the NTPEAK trigger was CPRE. This control trigger produced a signal if at least one charged track traversed the charged hodoscope. In particular, and since a $K^\pm \rightarrow \pi^\pm \gamma \gamma$ candidate would only fire the Q2 condition if there was a photon conversion before the hodoscope, only the Q1 part of this trigger was selected (total downscaling $D = 10000$). The use of T0N as control a trigger was discarded given that both T0N and NTPEAK were inefficient for the same kind of events, namely events with low energy deposited in the LKr calorimeter.

About 68,000 selected $K^\pm \rightarrow \pi^\pm \pi^0$ events were used as a control sample according to the criteria summarized in Table 8.5, out of which 37,000 had also the

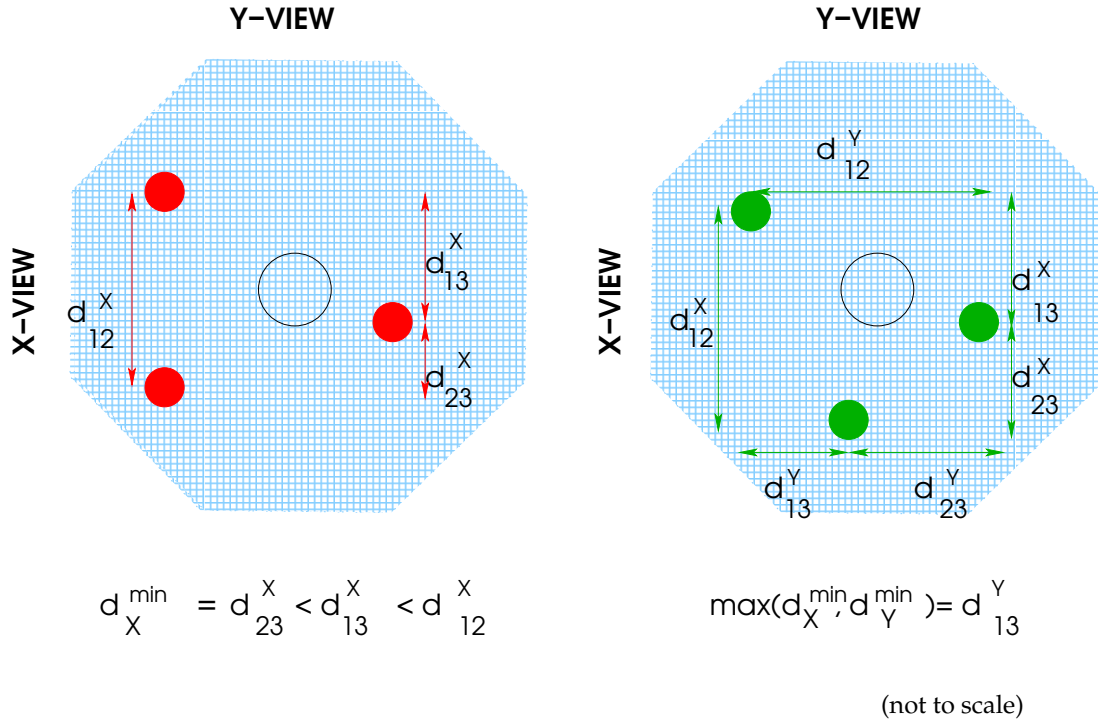


Figure 9.1: A three-cluster event only accepted by the $n_y > 2$ condition (left) and a three-cluster event accepted by both the $n_x > 2$ and the $n_y > 2$ conditions (right).

signal trigger set (efficient events). This channel had exactly the same signature, as seen by the NTPEAK trigger, as the $K^\pm \rightarrow \pi^\pm \gamma \gamma$ signal.

NTPEAK Efficiency Measurement

Under the assumption that three peaks are built, the NTPEAK condition is efficient only if:

- The clusters are well separated in at least one of the projections of the LKr calorimeter, so that they can be disentangled by the neutral trigger system. The relevant variables are the *distances between pairs of clusters in x- or y-views*. Figure 9.1 shows an example of two different kinds of 3-cluster events that would be accepted by the NTPEAK trigger. In the left plot, the three peaks would only be seen in the y -projection, while on the right plot both x - and y -projections would see the three peaks.
- The three clusters are energetic enough, so that they fire the corresponding strip signal. Since the energy of the photon clusters was required to be higher than 6 GeV in the selection (high enough for the trigger), the relevant quantity is only the *energy of the pion*. The higher the energy

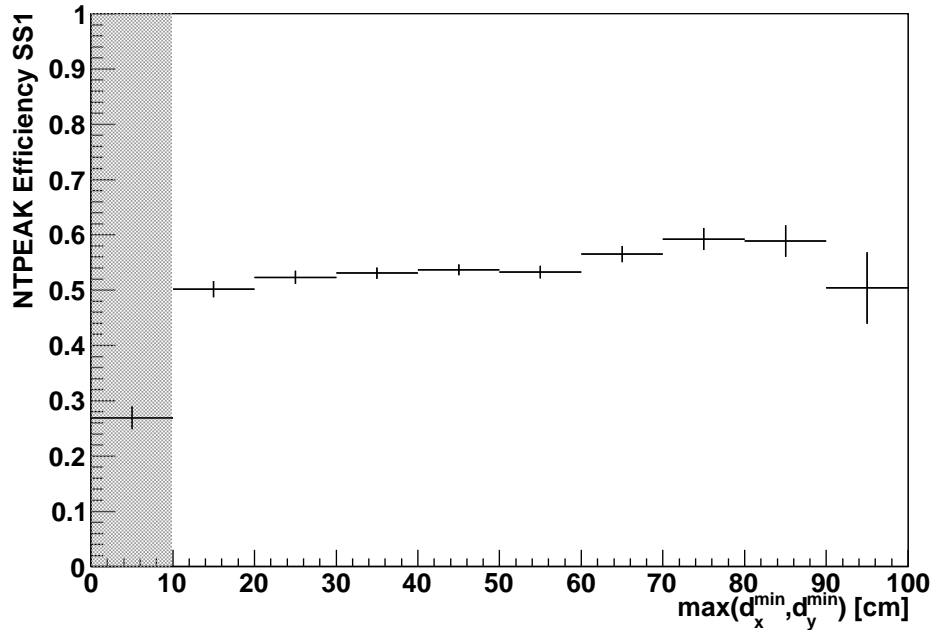


Figure 9.2: $K^\pm \rightarrow \pi^\pm \gamma \gamma$ NTPEAK trigger efficiency as a function of $\max(d_x^{\min}, d_y^{\min})$ for SS1.

of the pion track, the higher the probability that part of its shower in the LKr calorimeter will give a peak. To increase this probability, no energy requirement was applied to the pion shower clusters in the pre-selection procedure.

NTPEAK Projection Dependency

The three peaks required by the neutral trigger were only detected if the three corresponding clusters were well separated from each other in at least one of the LKr views. This means, that in case only one projection view was available for the trigger which was the case in SS2 and SS3 (Figure 9.1 (left)), the minimum distance between the three clusters d_y^{\min} had to be greater than d_{NUT}^{\min} (minimum distance required by the neutral trigger to disentangle two peaks). In the case of SS1, where both projection views were working in the trigger (Figure 9.1 (right)), this condition translated into $\max(d_x^{\min}, d_y^{\min})$ greater than d_{NUT}^{\min} .

In order to exclude large inefficiencies (see Figures 9.2 and 9.3), a cut on $d_{NUT}^{\min} > 10$ cm was included in the selection.

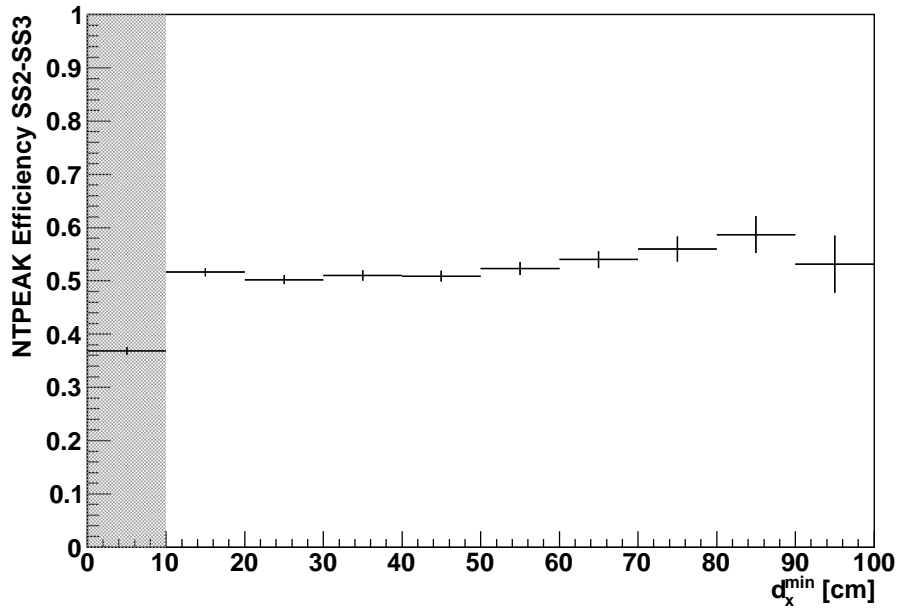


Figure 9.3: $K^\pm \rightarrow \pi^\pm \gamma \gamma$ NTPEAK trigger efficiency as a function of d_x^{\min} for SS2 and SS3 events.

Energy Dependency

Figure 9.4 shows the NTPEAK efficiency as a function of the pion energy. A big dependency on the pion energy can be seen for low energies, while for energies greater than 30 GeV the distribution becomes smoother. The projection cut at 10 cm increased the global efficiency by 1%, but did not alter the shape of the efficiency distribution versus the pion energy. The dependency of the NTPEAK efficiency on the pion energy $\epsilon(E_\pi)$, was implemented as a correction to the Monte Carlo sample. Figure 9.5 shows the NTPEAK efficiency as a function of the variable $z = m_{\gamma\gamma}^2/m_K^2$, obtained by using Eq. 9.1.2 for each bin (see also Section 11.3.2). The knowledge of this dependence is necessary to measure the branching ratio of $K^\pm \rightarrow \pi^\pm \gamma \gamma$ decays (Section 11.3) and to fit the di-photon mass spectrum (or equivalently $z = m_{\gamma\gamma}^2/m_K^2$) (Chapter 12).

The global efficiency of the NTPEAK trigger for $K^\pm \rightarrow \pi^\pm \gamma \gamma$ decays was measured to be $(47.36 \pm 0.47)\%$ in SS1, $(45.16 \pm 0.42)\%$ in SS2 and $(44.98 \pm 0.69)\%$ in SS3, and $(45.91 \pm 0.29)\%$ for all the periods together.

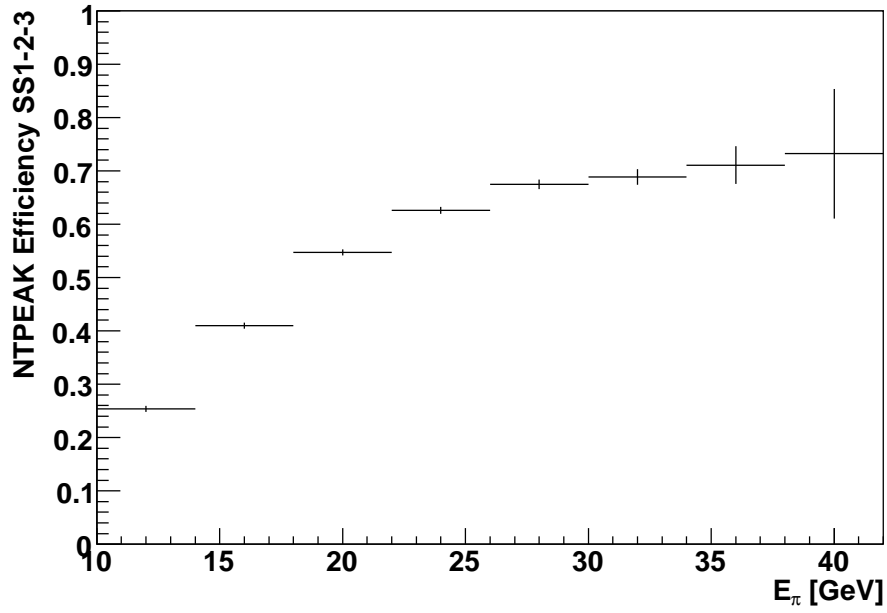


Figure 9.4: $K^\pm \rightarrow \pi^\pm \gamma \gamma$ NTPEAK trigger efficiency as a function of the pion energy.

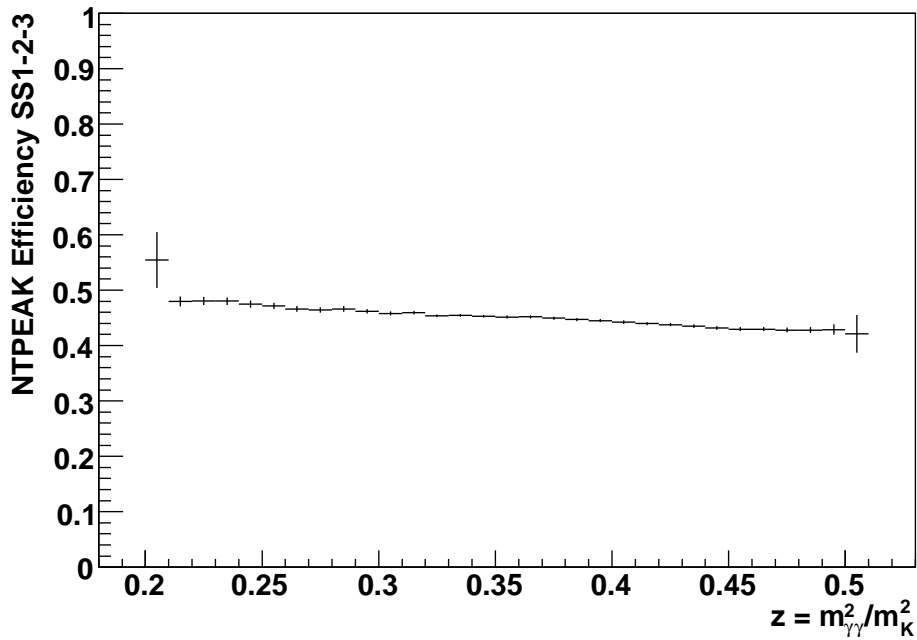


Figure 9.5: $K^\pm \rightarrow \pi^\pm \gamma \gamma$ NTPEAK trigger efficiency as a function of $z = m_\gamma^2 / m_K^2$.

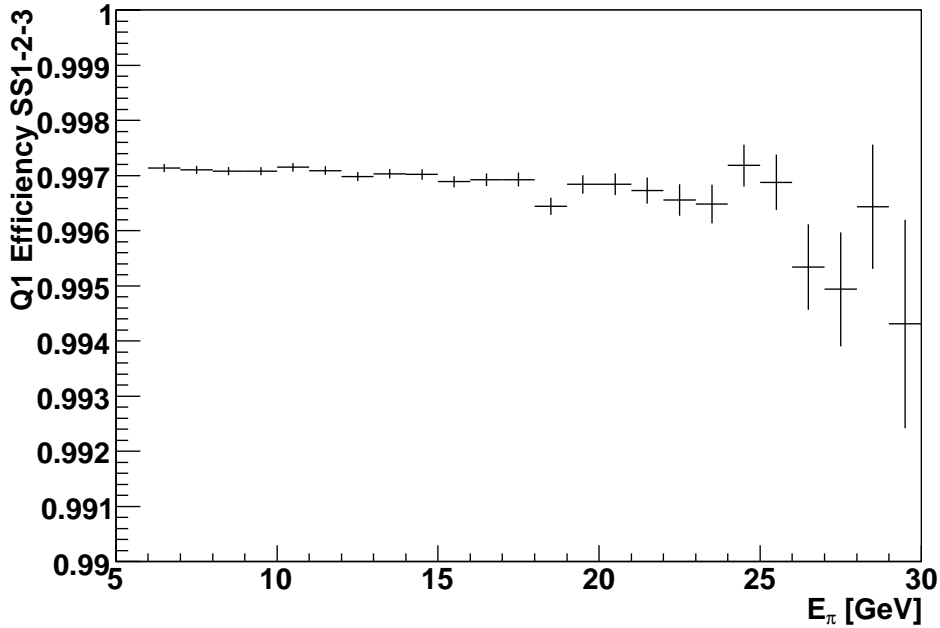


Figure 9.6: Q1 trigger efficiency as a function of the pion energy.

9.2.2 $\frac{Q1}{10}$ Efficiency Measurement

This trigger required just one charged particle traversing the charged hodoscope. Its signal was downscaled by a factor of 10.

The control trigger used to study this trigger efficiency was NTPEAK, given that both Q1 and NTPEAK were not correlated since one was a 'charged' trigger and the other one a 'neutral' trigger depending only on LKr clusters. As a control sample, a set of approximately $6 \cdot 10^6$ selected $K^\pm \rightarrow \pi^\pm \pi^0$ decays was used, assuming that any event with a pion track should behave in the same way as seen by the Q1 trigger.

The efficiency of this trigger was measured using Equation 9.1.1, finding $(99.696 \pm 0.004)\%$, $(99.689 \pm 0.004)\%$ and $(99.730 \pm 0.005)\%$ for SS1, SS2 and SS3, respectively. A global value of $(99.702 \pm 0.002)\%$ was measured for the whole data sample. Figure 9.6 shows the dependency of the Q1-trigger on the energy of the pion. No dependency was observed, confirming that the same efficiencies could be assumed for all one-charged-track decay channels.

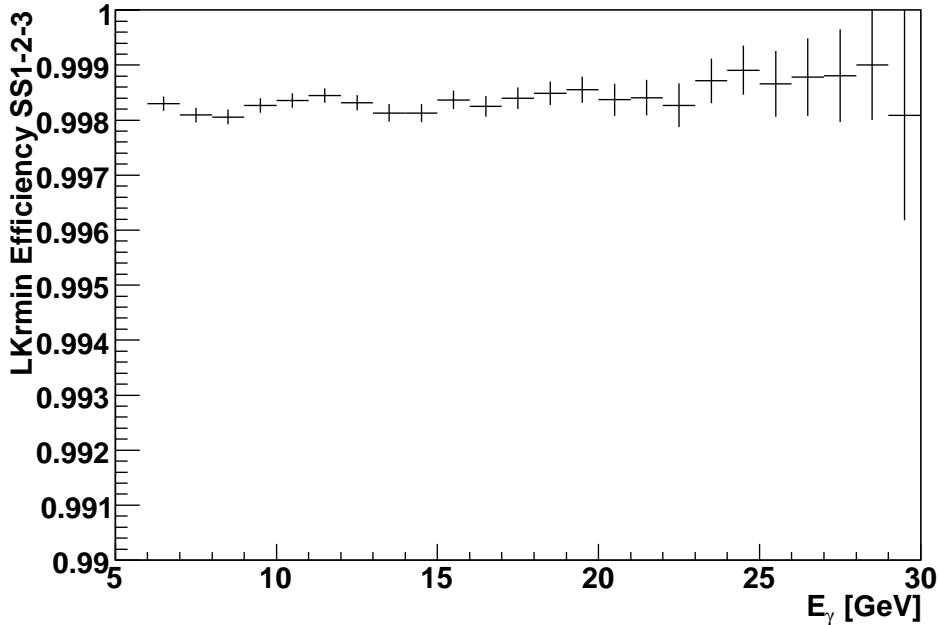


Figure 9.7: LKrmbias trigger efficiency as a function of the photon energy.

9.2.3 LKrmbias Efficiency Measurement

To calculate the efficiency of this neutral trigger, which required a minimum of 10 GeV of energy deposited in the LKr calorimeter, CPRE was chosen as an independent minimum bias control trigger. Like in the previous case and since LKrmbias only depends on the minimum energy deposited in the LKr calorimeter, about 1 million $K^\pm \rightarrow \pi^\pm \pi^0$ decays were used as a control sample. Figure 9.7 shows the dependency of the LKRmbias trigger on the energy of the single photons. No dependency on this variable was observed.

A global efficiency of $(99.828 \pm 0.004)\%$ was measured for this trigger, while for the super samples SS1, SS2 and SS3, (99.738 ± 0.008) , $(99.868 \pm 0.006)\%$, and $(99.911 \pm 0.006)\%$, were measured respectively.

9.2.4 (Q1 + Q2) Efficiency

For events with only one track, the (Q1 + Q2) signal is dominated by the Q1 condition, which has already been studied in the previous section.

9.2.5 MFAKE Trigger Efficiency

The main L2 trigger for the collection of $K^\pm \rightarrow \pi^\pm \gamma \gamma$ events was the MB-1TRK-P or MFAKE trigger. This trigger was designed to reject $K^\pm \rightarrow \pi^\pm \pi^0$ decays by requiring that $m_{fake} < 475 \text{ MeV}/c^2$.

Control Sample

To study the MFAKE efficiency, the neutral NTPEAK trigger which served as a L1 trigger for the selected $K^\pm \rightarrow \pi^\pm \gamma \gamma$ events was used as a control trigger. However, the number of $K^\pm \rightarrow \pi^\pm \gamma \gamma$ decays selected through the NTPEAK trigger was too small to perform a direct measurement of the efficiency.

An indirect measurement was done by assuming that the MFAKE trigger only depended on the charged track momentum and the z -vertex of the event. The control sample was composed of selected events with a signature as similar as possible to $K^\pm \rightarrow \pi^\pm \gamma \gamma$ decays, applying all pre-selection cuts, relaxing the COG cut to $COG < 10 \text{ cm}$, and removing all other selection cuts. In this way, the control sample consisted of about 65000 $K^\pm \rightarrow \pi^\pm \pi^0 \pi^0$ and $K^\pm \rightarrow \pi^\pm \pi^0 \gamma$ decays with low missing energy.

MFAKE Efficiency Measurement

As explained in Section 6.4.1, the MFAKE trigger depended only on the momentum of the pion, and the kaon decay vertex position. These dependencies were studied by measuring the efficiency of MFAKE as a function of $z_{vertex}^{charged}$, r_π^{DCH1} and E_π ¹.

Figures 9.8 and 9.9 (top) show the efficiency of the MFAKE trigger as a function of each variable (once integrated over the other two). Figure 9.9 (bottom) shows the MFAKE efficiency as a function of $z = m_{\gamma\gamma}^2/m_K^2$, obtained by using Equation 9.1.2 for each bin.

A three dimensional $10 \times 10 \times 10$ efficiency matrix in $z_{vertex}^{charged}$, r_π^{DCH1} and E_π was obtained as the result of the MFAKE efficiency measurement. This matrix was applied as a correction to the Monte Carlo $K^\pm \rightarrow \pi^\pm \gamma \gamma$ sample. The efficiency of this trigger was measured to be $(85.82 \pm 0.49)\%$ for SS1, $(85.51 \pm 0.47)\%$ for SS2, and $(84.71 \pm 0.81)\%$ for SS3. The global efficiency for the three periods together was $(85.61 \pm 0.31)\%$.

¹The radial distance to the beam pipe at DCH1 and the z -vertex define the pion direction of flight.

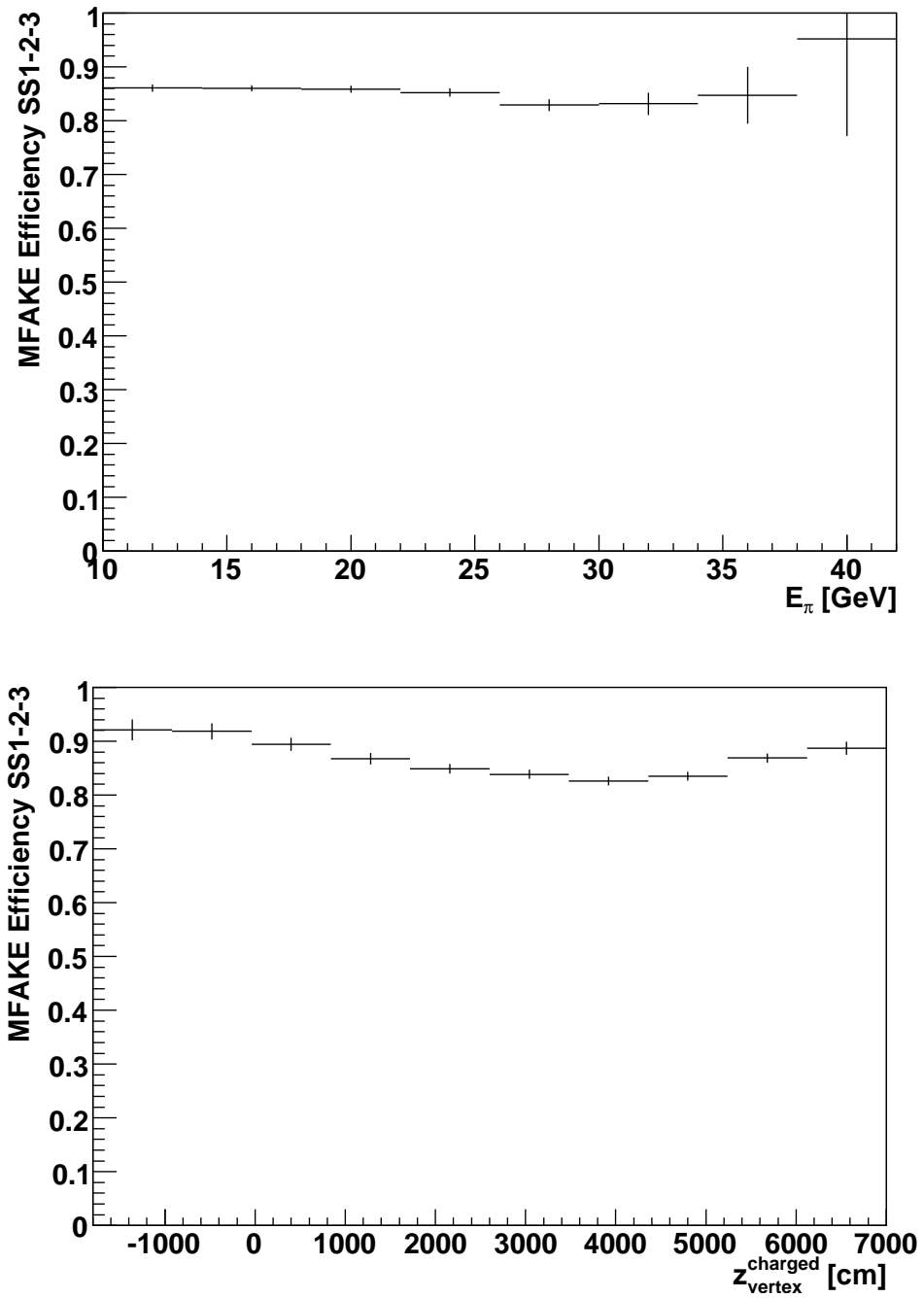


Figure 9.8: $K^{\pm} \rightarrow \pi^{\pm}\gamma\gamma$ MFAKE trigger efficiency as a function of the pion energy (top) and as a function of z -vertex position (bottom).

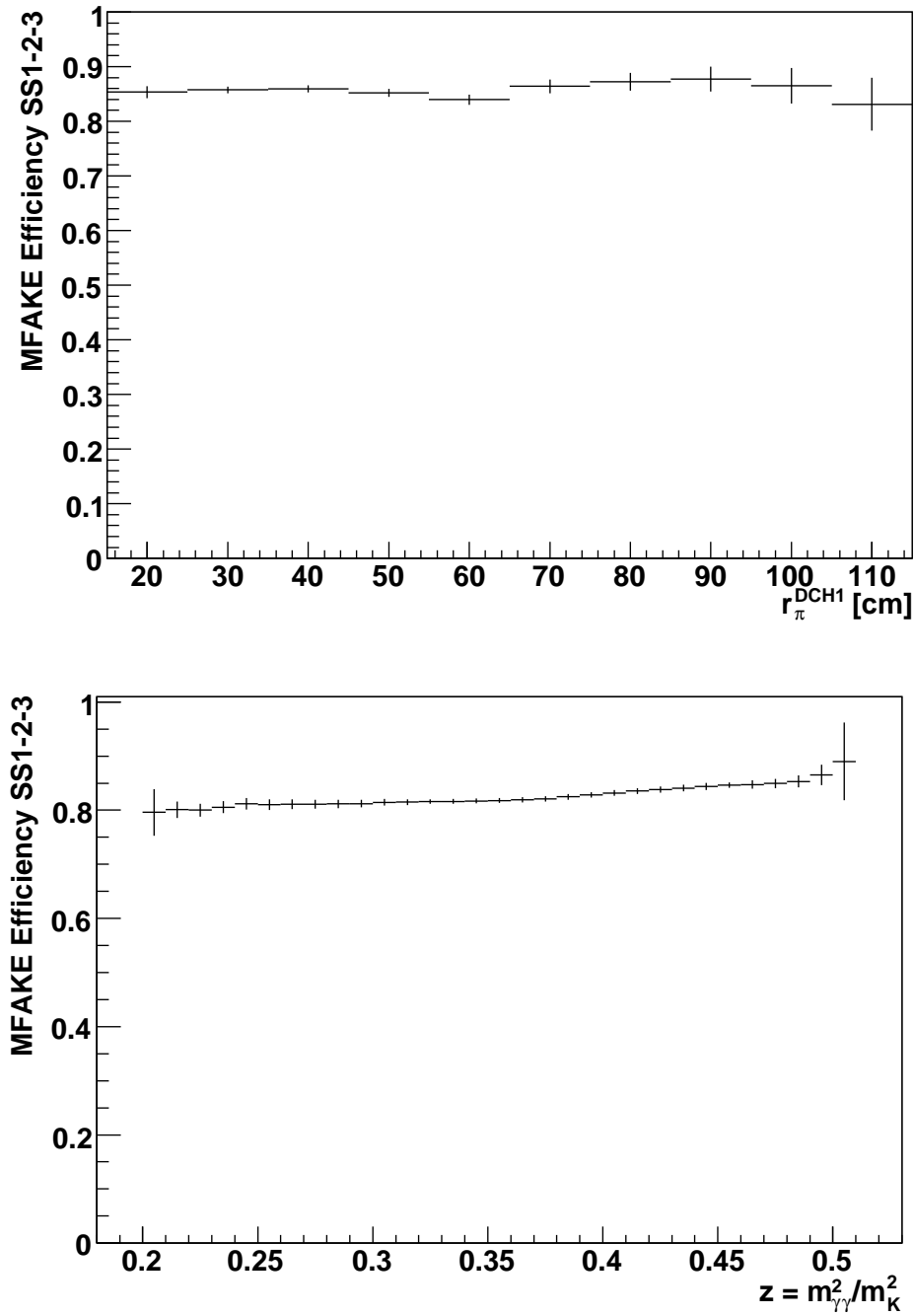


Figure 9.9: $K^\pm \rightarrow \pi^\pm \gamma \gamma$ MFAKE trigger efficiency as a function of the pion radial distance to the center of the beam pipe in DCH1 (top) and as a function of $z = m_{\gamma\gamma}^2/m_K^2$ (bottom).

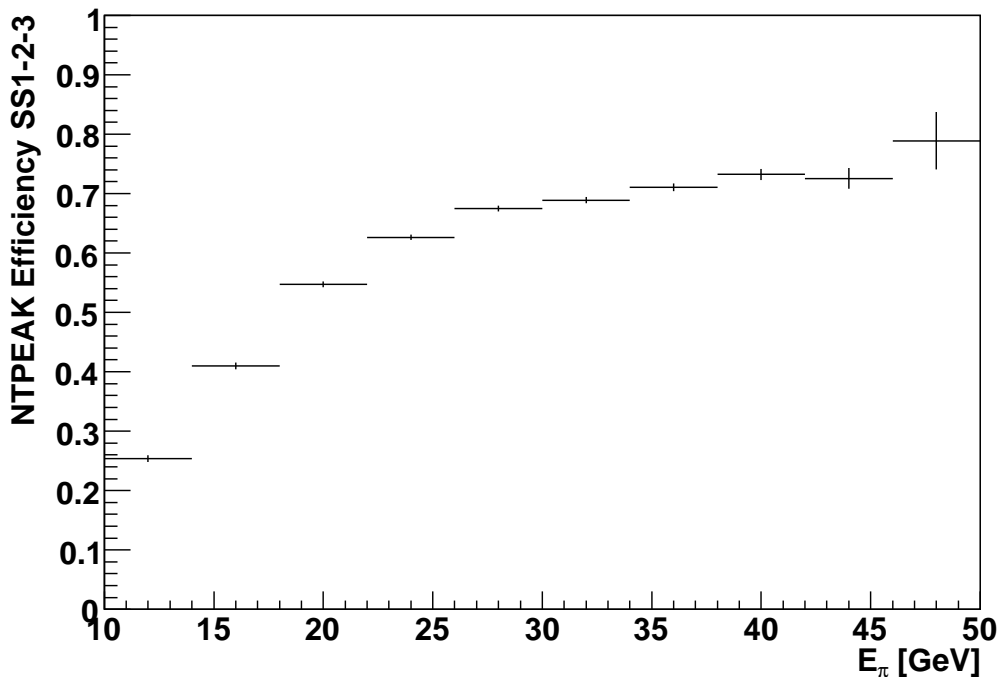


Figure 9.10: $K^\pm \rightarrow \pi^\pm \pi^0$ NTPEAK trigger efficiency as a function of the pion energy.

9.3 Trigger Efficiency of $K^\pm \rightarrow \pi^\pm \pi^0$ Decays

The $K^\pm \rightarrow \pi^\pm \pi^0$ channel was collected directly through the L2 NTPEAK trigger, which reproduced the conditions of the L1 NTPEAK, and was downscaled by a factor 50. Due to the high statistics of this channel, a direct measurement of the trigger efficiency using selected $K^\pm \rightarrow \pi^\pm \pi^0$ data as a control sample was possible. The data in the control sample fulfilled all selection criteria for the normalization channel (Table 8.5), including the NTPEAK trigger requirement on the minimum distance between the clusters (Section 9.2.1). Like in Section 9.2.1, the control trigger used was the Q1 condition of the CPRE trigger. Figure 9.10 shows the NTPEAK efficiency as a function of the pion energy. The same behavior as observed in Figure 9.4 is reproduced here for each bin. The dependency of the NTPEAK efficiency on the pion energy was implemented in the Monte Carlo.

The global efficiency of the NTPEAK trigger for $K^\pm \rightarrow \pi^\pm \pi^0$ decays was measured to be $(58.73 \pm 0.33)\%$ in SS1, $(57.07 \pm 0.29)\%$ in SS2 and $(57.12 \pm 0.47)\%$ in SS3, being $(57.67 \pm 0.20)\%$ the efficiency for all the periods together. The higher efficiency of the NTPEAK trigger for $K^\pm \rightarrow \pi^\pm \pi^0$ compared to $K^\pm \rightarrow \pi^\pm \gamma \gamma$ decays is due to the different pion energy spectrum.

9.4 Summary of Efficiencies

A summary of the L1 and L2 trigger efficiencies of signal $K^\pm \rightarrow \pi^\pm \gamma \gamma$ and normalization $K^\pm \rightarrow \pi^\pm \pi^0$ decays can be found in Tables 9.1 and 9.2.

The mean level 1 trigger efficiency, $\epsilon(\text{L1})$, for $K^\pm \rightarrow \pi^\pm \gamma \gamma$ decays was computed as:

$$\epsilon(\text{L1}) = \epsilon(\text{Q1} + \text{Q2}) \cdot \left[\epsilon(\text{NTPEAK}) + (1 - \epsilon(\text{NTPEAK})) \cdot \epsilon(\text{LKrmin}) \cdot \frac{\epsilon(\text{Q1})}{10} \right],$$

Events triggered by both NTPEAK and LKrmbias were only counted once, as triggering only the NTPEAK condition. The total trigger efficiency for $K^\pm \rightarrow \pi^\pm \gamma \gamma$ decays is then $\epsilon = \epsilon(\text{L1}) \times \epsilon(\text{L2})$.

In the case of $K^\pm \rightarrow \pi^\pm \pi^0$ decays, the total efficiency is just the efficiency of the NTPEAK trigger.

Period	$\epsilon(\text{NTPEAK})$	$\epsilon(\text{Q1})$	$\epsilon(\text{LKrmbias})$	$\epsilon(\text{L1})$	$\epsilon(\text{MFAKE})$
SS1	47.36 ± 0.47	99.696 ± 0.004	99.738 ± 0.008	52.44 ± 0.42	85.82 ± 0.49
SS2	45.16 ± 0.42	99.689 ± 0.004	99.868 ± 0.006	50.46 ± 0.38	85.51 ± 0.47
SS3	44.98 ± 0.69	99.730 ± 0.005	99.911 ± 0.006	50.03 ± 0.62	84.71 ± 0.81
SS1-2-3	45.91 ± 0.29	99.702 ± 0.002	99.828 ± 0.004	51.14 ± 0.26	85.61 ± 0.31

Table 9.1: $K^\pm \rightarrow \pi^\pm \gamma \gamma$ Efficiencies (in %) for the different data taking periods.

Period	$\epsilon_{\pi^\pm \gamma \gamma}$	$\epsilon_{\pi^\pm \pi^0}$
SS1	45.00 ± 0.44	58.73 ± 0.33
SS2	43.15 ± 0.40	57.07 ± 0.29
SS3	42.38 ± 0.66	57.12 ± 0.47
SS1-2-3	43.78 ± 0.27	57.67 ± 0.20

Table 9.2: Total $K^\pm \rightarrow \pi^\pm \gamma \gamma$ and $K^\pm \rightarrow \pi^\pm \pi^0$ efficiencies (in %) for the different data taking periods.

10 Data and Monte Carlo Comparison

In the following sections, the comparison between data and Monte Carlo signal and normalization events is shown for some relevant variables before and after applying trigger efficiency corrections in the simulations. Big improvement in the Monte Carlo description of the data is especially remarkable for variables like the pion energy and others the trigger was directly or indirectly depending on.

The comparison between data and Monte Carlo for the $K^\pm \rightarrow \pi^\pm \gamma \gamma$ selected events is presented in Section 10.0.1, while the same comparison for the selected $K^\pm \rightarrow \pi^\pm \pi^0$ events is shown in Section 10.0.2. Due to the much higher statistics available for the normalization channel (much smaller error bars), the improvement after applying trigger efficiency corrections in the Monte Carlo is even more remarkable than for the signal, where the error bars are often too big to see a clear improvement. For the signal, MC simulation with $\hat{c} = 1.74$ was used (Sec. 7.2.2).

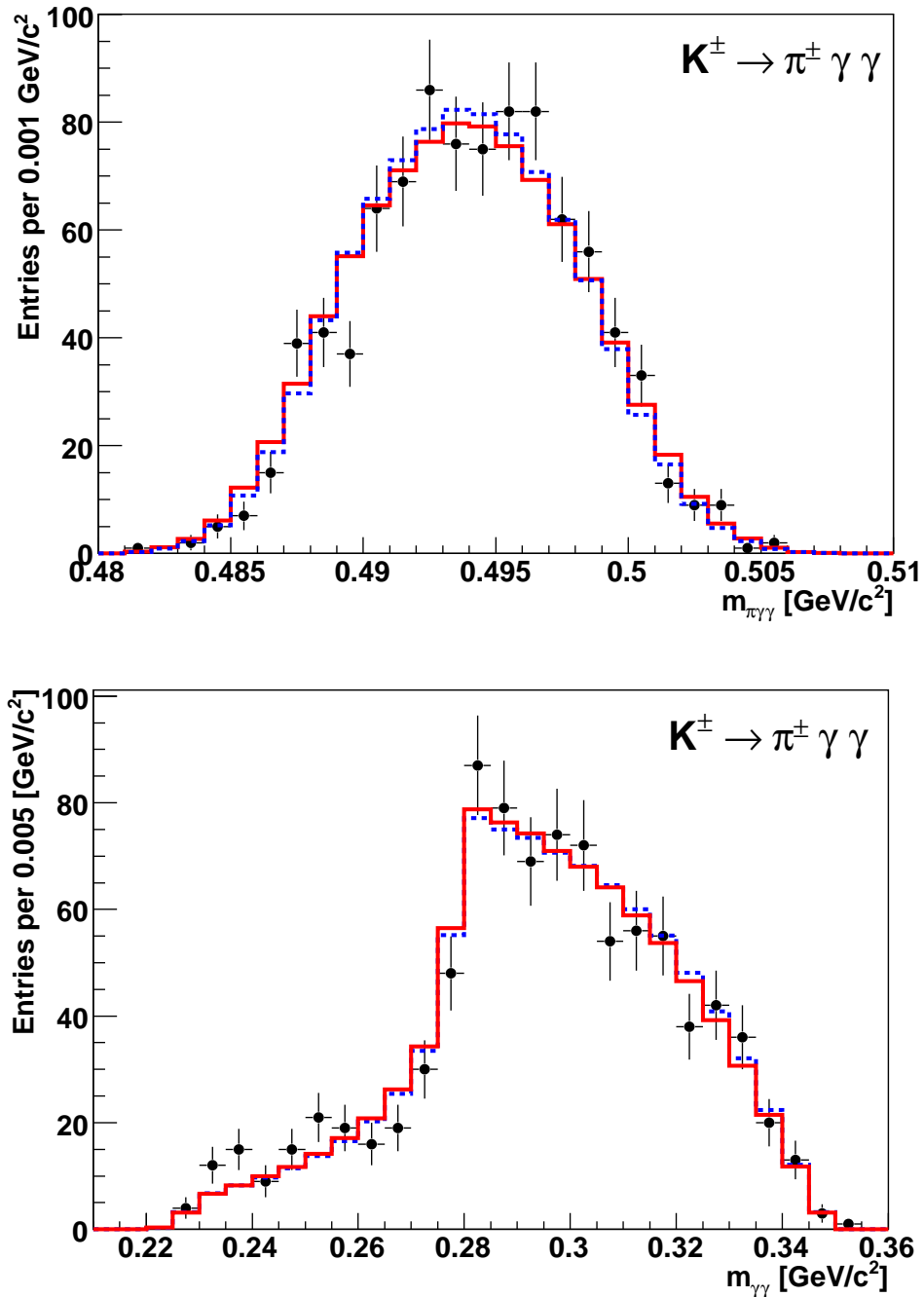
10.0.1 $K^\pm \rightarrow \pi^\pm \gamma \gamma$ Decays

Figure 10.1: Invariant $m_{\pi\gamma\gamma}$ mass (top) and invariant $m_{\gamma\gamma}$ mass (bottom) for selected signal data candidates (dots), and MC signal events before (dashed line) and after (full line) trigger efficiency corrections.

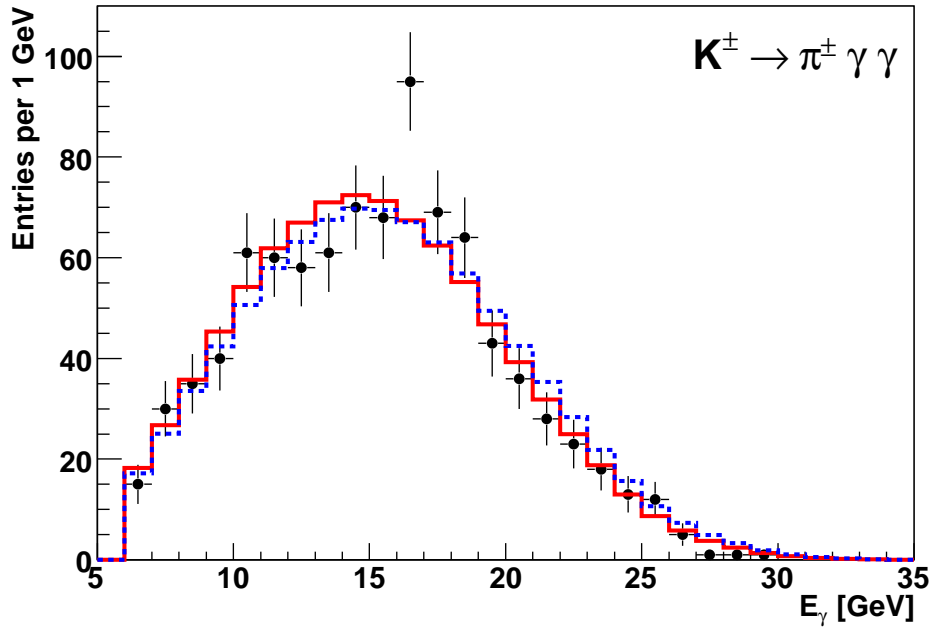
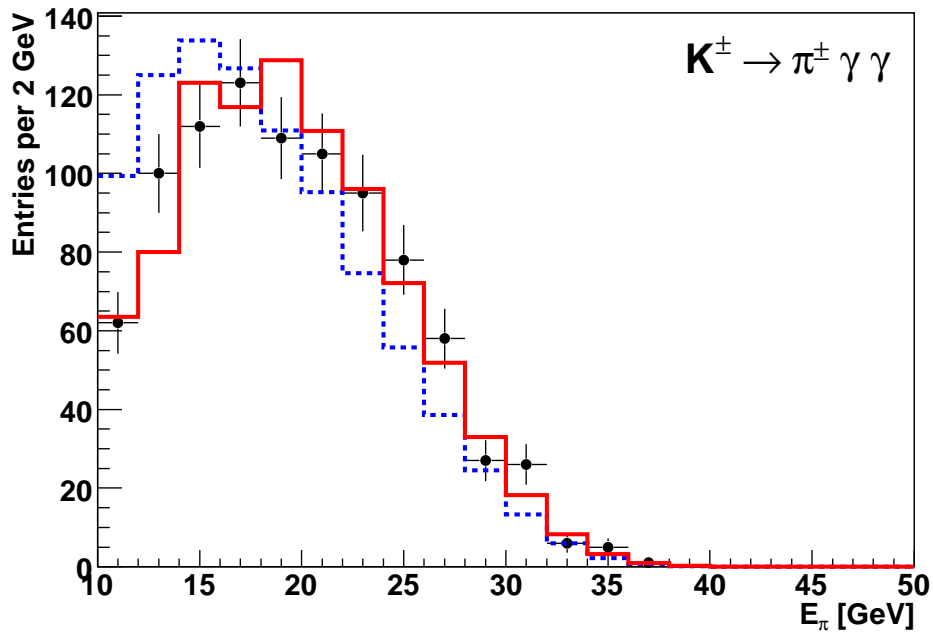


Figure 10.2: Pion energy (top) and energy of the lowest energy photon (bottom) for selected signal data candidates (dots), and MC signal events before (dashed line) and after (full line) trigger efficiency corrections.

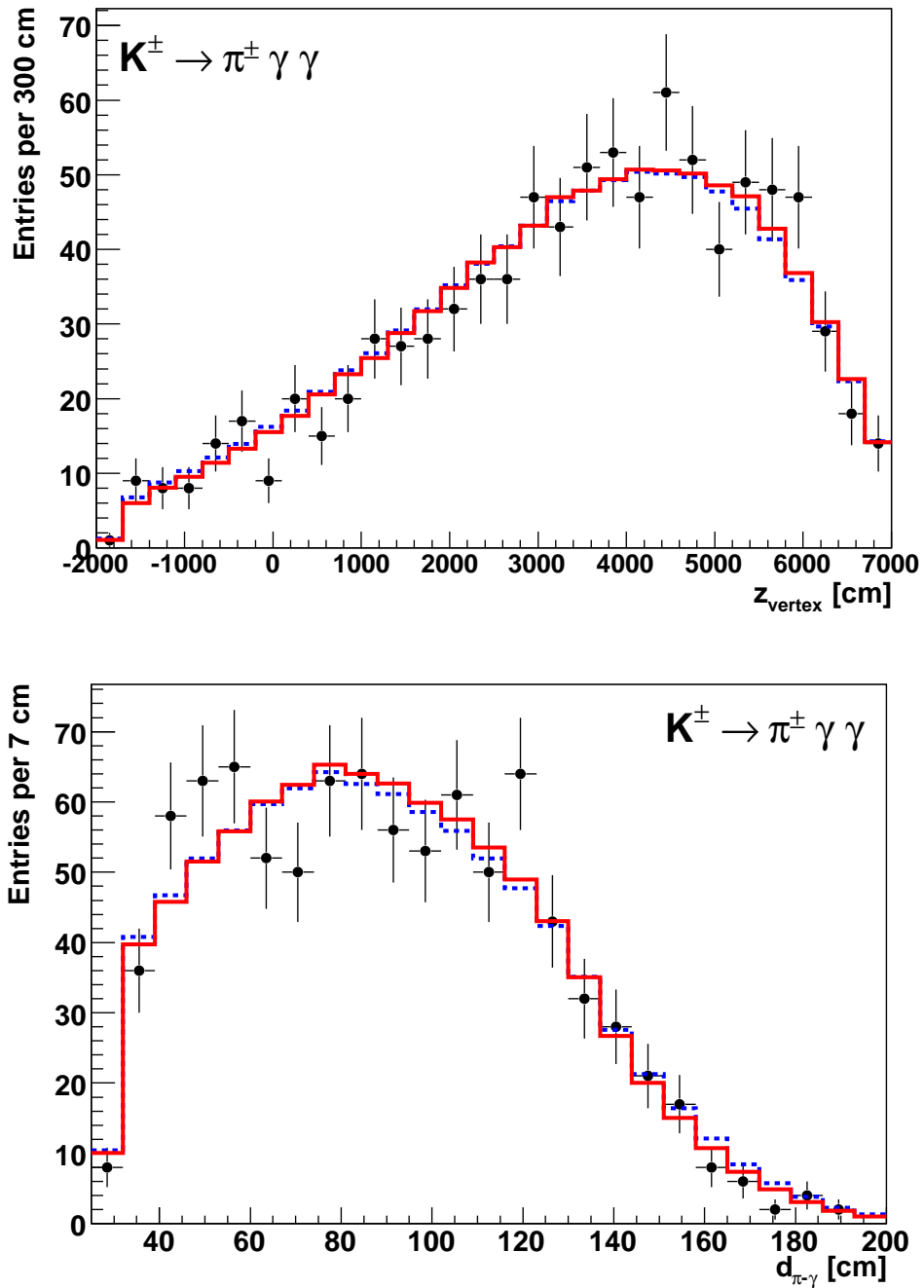


Figure 10.3: Decay vertex position (top) and distance between pion track and photon cluster in LKr (bottom) for selected signal data candidates (dots), and MC signal events before (dashed line) and after (full line) trigger efficiency corrections.

10.0.2 $K^\pm \rightarrow \pi^\pm \pi^0$ Decays

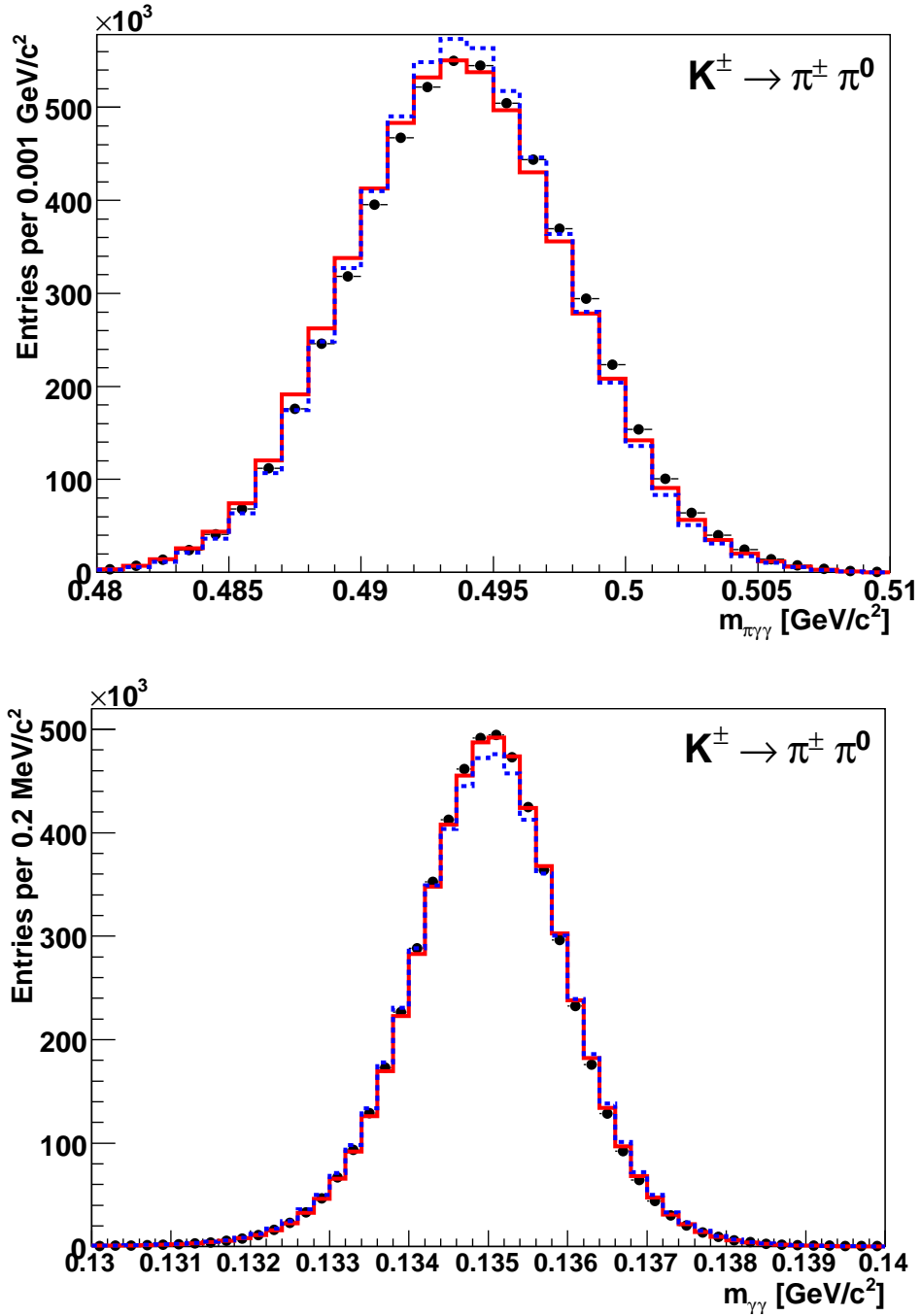


Figure 10.4: Invariant $m_{\pi\gamma\gamma}$ mass (top) and invariant $m_{\gamma\gamma}$ mass (bottom) for selected normalization data candidates (dots), and MC normalization events before (dashed line) and after (full line) trigger efficiency corrections.

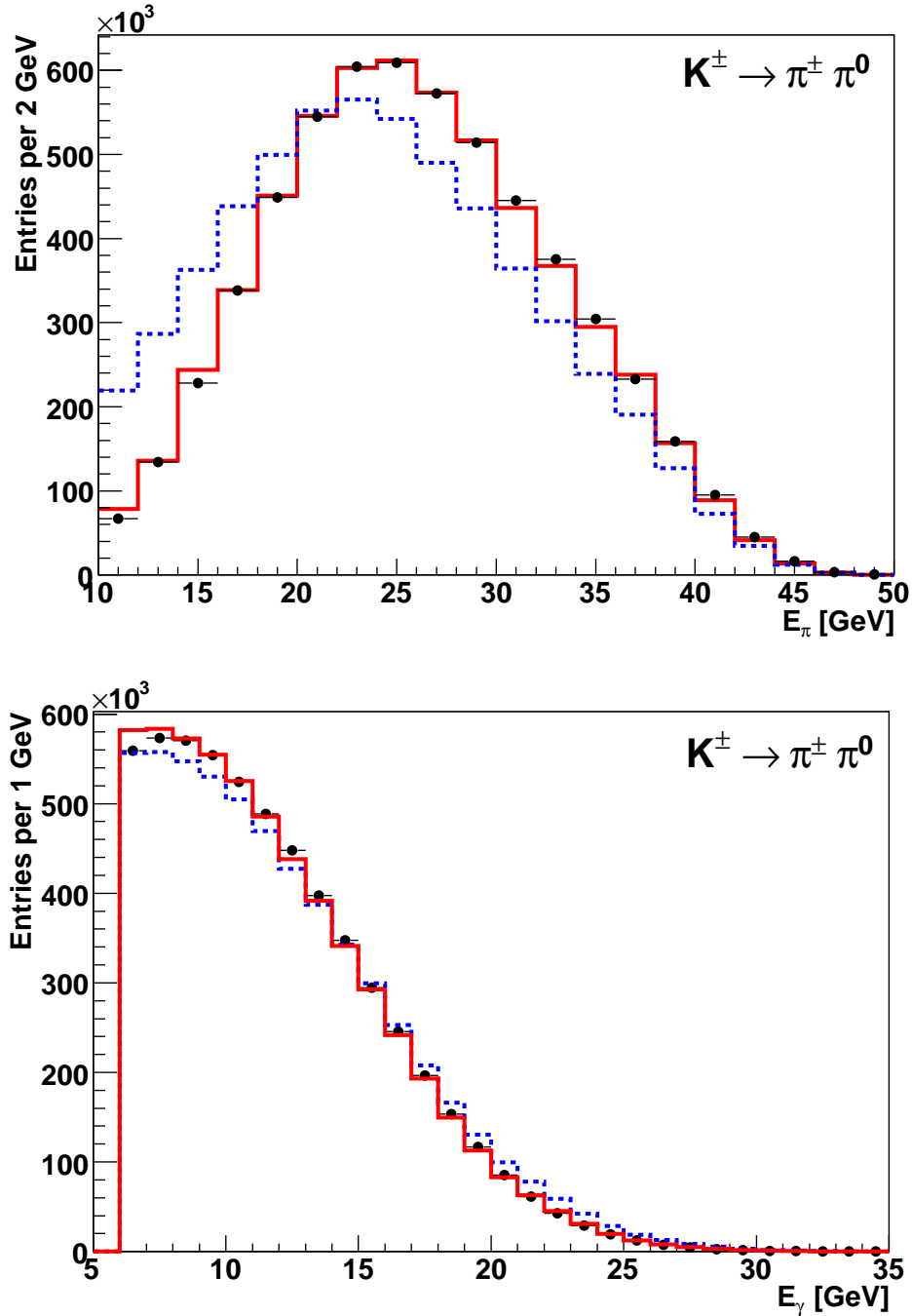


Figure 10.5: Pion energy (top) and energy of the lowest energy photon (bottom) for selected normalization data candidates (dots), and MC normalization events before (dashed line) and after (full line) trigger efficiency corrections.

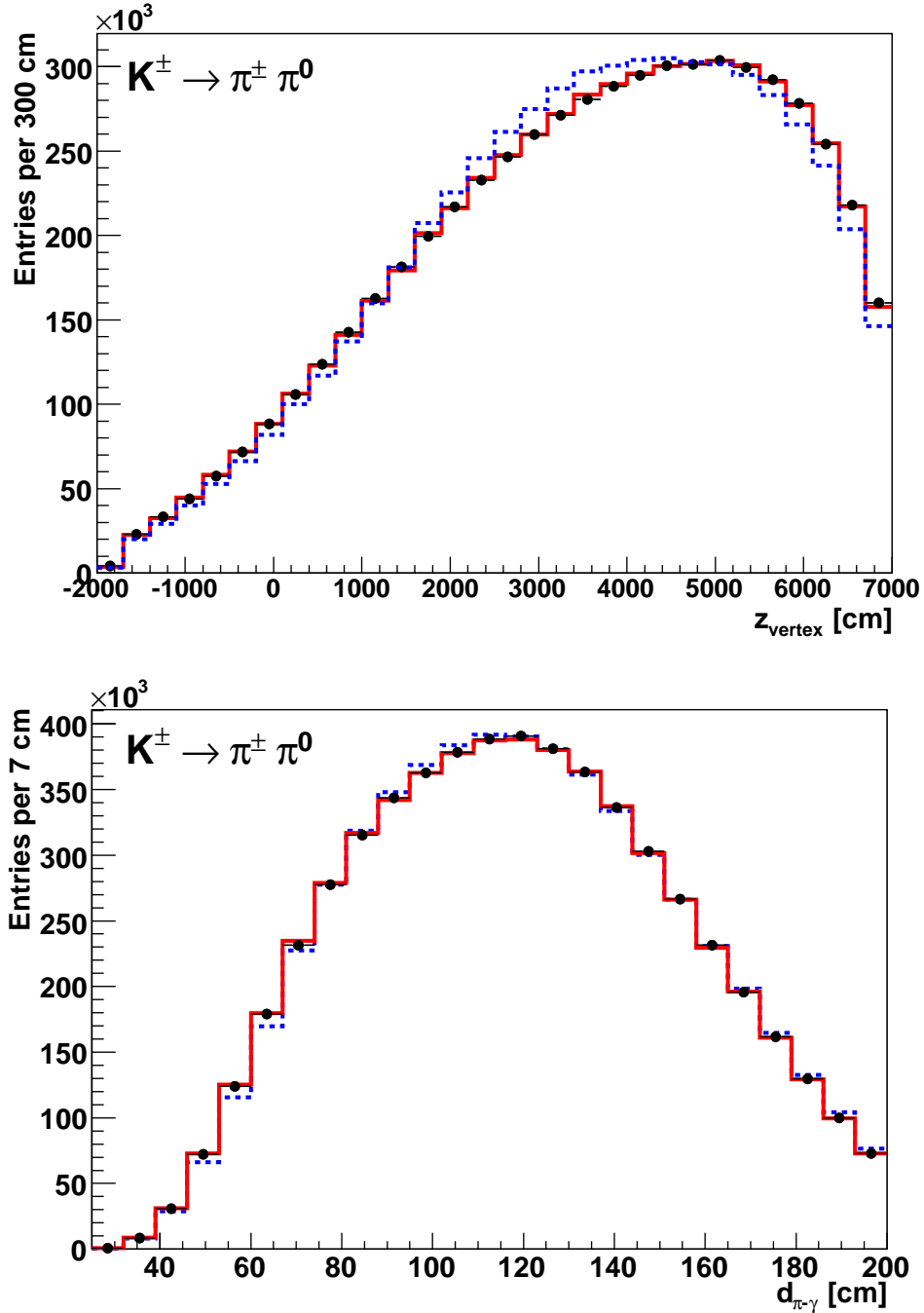


Figure 10.6: Decay vertex position (top) and distance between pion track and photon cluster in LKr (bottom) for selected normalization data candidates (dots), and MC normalization events before (dashed line) and after (full line) trigger efficiency corrections.

11 Measurement of BR($K^\pm \rightarrow \pi^\pm \gamma\gamma, z \geq 0.2$)

The branching ratio of the $K^\pm \rightarrow \pi^\pm \gamma\gamma$ channel is the ratio of $K^\pm \rightarrow \pi^\pm \gamma\gamma$ decays with respect to all possible K^\pm decay channels. In general, a branching ratio is obtained from the number of selected signal events (once the background has been subtracted), N_{x_S} , normalized to the signal acceptance α_{x_S} , the trigger efficiency for the signal ϵ_{x_S} and the kaon flux Φ_K :

$$\text{BR}(K \rightarrow x_S) = \frac{N_{x_S}}{\alpha_{x_S} \cdot \epsilon_{x_S} \cdot \Phi_K}. \quad (11.0.1)$$

In the following sections, all the quantities involved in the previous equation are computed. Flux and background expectation studies are presented in Sections 11.1 and 11.2, respectively, and the branching ratio measurement is explained in Section 11.3. Systematic uncertainties are studied in Section 11.4, and the final result of the branching ratio measurement with all its uncertainty sources is summarized in Section 11.5.

11.1 Kaon Flux

The flux, Φ_K , is the total number of kaon decays occurring in the acceptance region.

The flux is measured from a *normalization channel*, which has a similar signature than the signal, and is collected simultaneously and through similar selection criteria. In this way, systematic uncertainties arising from the reconstruction and the selection of the events cancel in Eq. 11.0.1. To avoid large statistical uncertainties, a normalization channel with a sufficiently high and precise branching ratio is chosen. For these reasons, $K^\pm \rightarrow \pi^\pm \pi^0$ decays were used in this thesis as normalization channel.

The kaon flux in the acceptance region is calculated as:

$$\Phi_K = \frac{N_{\pi^\pm \pi^0} \cdot D}{\alpha_{\pi^\pm \pi^0} \cdot \epsilon_{\pi^\pm \pi^0} \cdot \text{BR}(K^\pm \rightarrow \pi^\pm \pi^0) \cdot \text{BR}(\pi^0 \rightarrow \gamma\gamma)}, \quad (11.1.1)$$

where $N_{\pi^\pm \pi^0}$ is the number of $K^\pm \rightarrow \pi^\pm \pi^0$ decays reconstructed from the data collected through the NTPEAK trigger, $D = 50$ is the downscaling factor

11 Measurement of $BR(K^\pm \rightarrow \pi^\pm \gamma\gamma, z \geq 0.2)$

Period	$N_{\pi^\pm\pi^0}$	$\alpha_{\pi^\pm\pi^0}$	$\epsilon_{\pi^\pm\pi^0}$	$\Phi_K(10^9)$
SS1	2,006,413	0.13432 ± 0.00021	0.5873 ± 0.0033	$6.234 \pm 0.037_{\text{stat}}$
SS2	2,734,139	0.11137 ± 0.00017	0.5707 ± 0.0029	$10.543 \pm 0.056_{\text{stat}}$
SS3	1,009,569	0.11151 ± 0.00021	0.5712 ± 0.0047	$3.885 \pm 0.033_{\text{stat}}$
SS1-2-3	5,750,121	0.11832 ± 0.00011	0.5767 ± 0.0020	$20.654 \pm 0.075_{\text{stat}}$

Table 11.1: Summary of the kaon fluxes and related quantities in the different super sample periods. The fluxes were measured for the $-1800 \text{ cm} < z_{\text{vertex}} < 7000 \text{ cm}$ decay vertex region.

applied to this trigger, $\alpha_{\pi^\pm\pi^0}$ is the acceptance of the selection, $\epsilon_{\pi^\pm\pi^0}$ is the efficiency of the NTPEAK trigger, and $BR(K^\pm \rightarrow \pi^\pm\pi^0) \cdot BR(\pi^0 \rightarrow \gamma\gamma) = (0.2040 \pm 0.0009)$ [4, 108]. In general, the acceptance of a decay is calculated as the inverse of the ratio between the number of *generated* MC decays in the studied acceptance region, N^{gen} , and the number of those events which are *reconstructed* after all selection criteria have been applied, N^{rec} :

$$\alpha(z_{\text{vertex}}, E_K) = \frac{N^{\text{rec}}(z_{\text{vertex}}, E_K)}{N^{\text{gen}}(z_{\text{vertex}}, E_K)}. \quad (11.1.2)$$

In this thesis, the acceptance region was defined by the $-1800 \text{ cm} < z_{\text{vertex}} < 7000 \text{ cm}$ decay vertex region and $55 < E_K < 65 \text{ GeV}$ kaon energy.

About 8 million generated $K^\pm \rightarrow \pi^\pm\pi^0$ decays were to measure $\alpha(\pi^\pm\pi^0)$, with the result 0.1183 ± 0.0011 . The NTPEAK efficiency for $K^\pm \rightarrow \pi^\pm\pi^0$ decays was measured to be 0.5767 ± 0.0020 (Section 9.4). Around 5.75 million $K^\pm \rightarrow \pi^\pm\pi^0$ event candidates free of background were reconstructed after all selection criteria had been applied for the selection of the normalization channel (Table 8.5). Acceptances, efficiencies, number of reconstructed $K^\pm \rightarrow \pi^\pm\pi^0$ events and fluxes obtained by applying Eq. 11.1.1 are summarized in Table 11.1 for each super sample period. Note that due to the different NTPEAK trigger conditions in the three super samples (Section 9.2.1), the acceptances of super sample 2 and 3 are smaller than in super sample 1.

The total flux in the acceptance region was measured to be:

$$\begin{aligned} \Phi_K &= (20.654 \pm 0.009_{\text{data}} \pm 0.019_{\alpha} \pm 0.072_{\epsilon} \pm 0.091_{\text{ext}}) \cdot 10^9 \\ &= (20.654 \pm 0.075_{\text{stat}} \pm 0.091_{\text{ext}}) \cdot 10^9, \end{aligned} \quad (11.1.3)$$

where σ_{data} is the statistical uncertainty from the reconstructed $K^\pm \rightarrow \pi^\pm\pi^0$ data, $\sigma_{\alpha, \epsilon}$ are the statistical uncertainties from the acceptance and efficiency measurements, respectively, and σ_{ext} is the external uncertainty from $BR(K^\pm \rightarrow \pi^\pm\pi^0) \cdot BR(\pi^0 \rightarrow \gamma\gamma)$. The total statistical uncertainty, σ_{stat} , is the square root of the sum in quadrature of the individual uncertainties.

11.2 Background Expectation

The amount of events expected from a given background channel surviving all selection cuts and selected together with the final $K^\pm \rightarrow \pi^\pm \gamma \gamma$ candidates was estimated as:

$$N_{x_B} = \Phi_K \cdot \text{BR}(K \rightarrow x_B) \cdot \alpha_{x_B} \cdot \epsilon_{x_B}, \quad (11.2.1)$$

being $\text{BR}(K \rightarrow x_B)$, α_{x_B} and ϵ_{x_B} the branching ratio, acceptance and trigger efficiency of the background channel under study. Given that the remaining background was not distinguishable from the signal, the same trigger efficiencies were assumed for signal and background channels, i.e. $\epsilon_{x_B} = 0.4378 \pm 0.0027$ (Section 9.4).

The potential channels contributing to the signal background were presented in Section 8.4, namely $K^\pm \rightarrow \pi^\pm \pi^0 \gamma$ and $K^\pm \rightarrow \pi^\pm \pi^0 \pi^0$ decays with one or two not reconstructed decay photons, respectively.

Expected $K^\pm \rightarrow \pi^\pm \pi^0 \pi^0$ background.

The acceptance for these decays was calculated using about 92.6 million MC $K^\pm \rightarrow \pi^\pm \pi^0 \pi^0$ generated events (about one fourth of the total $K^\pm \rightarrow \pi^\pm \pi^0 \pi^0$ decays occurring in the decay region). The acceptance obtained after all signal selection criteria were applied was $(3.2 \pm 1.9) \cdot 10^{-8}$, which substituted in Eq. 11.2.1 gave an estimate of 5 ± 3 $K^\pm \rightarrow \pi^\pm \pi^0 \pi^0$ events, or equivalently, 0.6% of the 908 signal candidates.

Expected $K^\pm \rightarrow \pi^\pm \pi^0 \gamma$ background.

Since the branching ratios for $K^\pm \rightarrow \pi^\pm \pi^0 \gamma$ decays quoted in [108] are valid only for the $55 \text{ MeV} < T_{\pi^\pm}^{CM} < 90 \text{ MeV}$ kinematic region, the acceptance in Equation 11.2.1 was redefined to normalize it to the whole spectrum:

$$\alpha_{\pi^\pm \pi^0 \gamma} = \frac{N_{\pi^\pm \pi^0 \gamma}^{rec}}{N_{\pi^\pm \pi^0 \gamma}^{gen}(55 \text{ MeV} < T_{\pi^\pm}^{CM} < 90 \text{ MeV})}, \quad (11.2.2)$$

with $N_{\pi^\pm \pi^0 \gamma}^{rec}$ the number of reconstructed MC $K^\pm \rightarrow \pi^\pm \pi^0 \gamma$ decays after all signal selection cuts and in the complete $T_{\pi^\pm}^{CM}$ spectrum, and $N_{\pi^\pm \pi^0 \gamma}^{gen}(55 \text{ MeV} < T_{\pi^\pm}^{CM} < 90 \text{ MeV})$ the number of generated MC $K^\pm \rightarrow \pi^\pm \pi^0 \gamma$ decays with $55 \text{ MeV} < T_{\pi^\pm}^{CM} < 90 \text{ MeV}$.

The contributions to the background from the three different $K^\pm \rightarrow \pi^\pm \pi^0 \gamma$ channels were studied separately:

x_B	$BR(K \rightarrow x_B)$	α_{x_B}	$\epsilon_{x_B} (\%)$	N_{x_B}
$\pi^\pm \pi^0 \pi^0$	$(1.757 \pm 0.024)\%$	$(3.2 \pm 1.9) \cdot 10^{-8}$	43.78 ± 0.27	5 ± 3
$\pi^\pm \pi^0 \gamma$ IB	$(2.75 \pm 0.15) \cdot 10^{-4}$	$(2.70 \pm 0.11) \cdot 10^{-5}$	43.78 ± 0.27	66 ± 4
$\pi^\pm \pi^0 \gamma$ DE	$(4.4 \pm 0.7) \cdot 10^{-6}$	$(6.0 \pm 0.3) \cdot 10^{-5}$	43.78 ± 0.27	2 ± 1
$\pi^\pm \pi^0 \gamma$ INT	$-(5.8 \pm 2.4) \cdot 10^{-6}$	$(6.0 \pm 0.4) \cdot 10^{-5}$	43.78 ± 0.27	$-(3 \pm 1)$

Table 11.2: Summary of the background expected in the complete data taking period. The branching ratios of the first three channels are listed in [108], while the one of $K^\pm \rightarrow \pi^\pm \pi^0 \gamma$ INT was obtained from [97, 67]. To calculate the expected background from each channel, the branching ratios of the table were multiplied by $BR(\pi^0 \rightarrow \gamma \gamma)$ in the case of $K^\pm \rightarrow \pi^\pm \pi^0 \gamma$ decays and by $(BR(\pi^0 \rightarrow \gamma \gamma))^2$ in the case of $K^\pm \rightarrow \pi^\pm \pi^0 \pi^0$ decays, since the MC simulations assumed π^0 decays into two photons for all cases.

- $K^\pm \rightarrow \pi^\pm \pi^0 \gamma$ IB.** About 97 million MC $K^\pm \rightarrow \pi^\pm \pi^0 \gamma$ IB decays were generated in the whole $T_{\pi^\pm}^{CM}$ range, of which 21 million had $55 \text{ MeV} < T_{\pi^\pm}^{CM} < 90 \text{ MeV}$ (4 times more than the total $K^\pm \rightarrow \pi^\pm \pi^0 \gamma$ IB decays occurring in the decay region). The acceptance obtained after all selection criteria were applied was $(2.70 \pm 0.11) \cdot 10^{-5}$. From Eq. 11.2.1, the amount of remaining background estimated for this channel was 66 ± 4 events, corresponding to 7.3% of the signal candidates. This background was originating from decays where the odd photon perfectly overlapped with one of the photons from the π^0 decay (see Figure 11.1), so that the π^0 mass was no longer reconstructed.
- $K^\pm \rightarrow \pi^\pm \pi^0 \gamma$ DE.** Approximately 11 million MC $K^\pm \rightarrow \pi^\pm \pi^0 \gamma$ DE decays were generated in the complete $T_{\pi^\pm}^{CM}$ spectrum, with about 8 million inside the region $55 \text{ MeV} < T_{\pi^\pm}^{CM} < 90 \text{ MeV}$ (90 times more than the total $K^\pm \rightarrow \pi^\pm \pi^0 \gamma$ DE decays occurring in the decay region). The acceptance obtained after all selection criteria were applied was $(6.0 \pm 0.3) \cdot 10^{-5}$. The amount of remaining background estimated from this channel was 2 ± 1 events, corresponding to 0.2% of the signal candidates.
- $K^\pm \rightarrow \pi^\pm \pi^0 \gamma$ INT.** Around 6.5 million MC $K^\pm \rightarrow \pi^\pm \pi^0 \gamma$ INT decays were generated in the full $T_{\pi^\pm}^{CM}$ spectrum, with approximately 3.4 million in the region with $55 \text{ MeV} < T_{\pi^\pm}^{CM} < 90 \text{ MeV}$ (30 times more than the total $K^\pm \rightarrow \pi^\pm \pi^0 \gamma$ INT decays occurring in the decay region). The acceptance obtained after all selection criteria were applied was $(6.0 \pm 0.4) \cdot 10^{-5}$. The amount of remaining background estimated from this channel was 3 ± 1 events, corresponding to 0.3% of the signal candidates. Note that the background arising from this channel interferes negatively with the IB and the DE contributions.

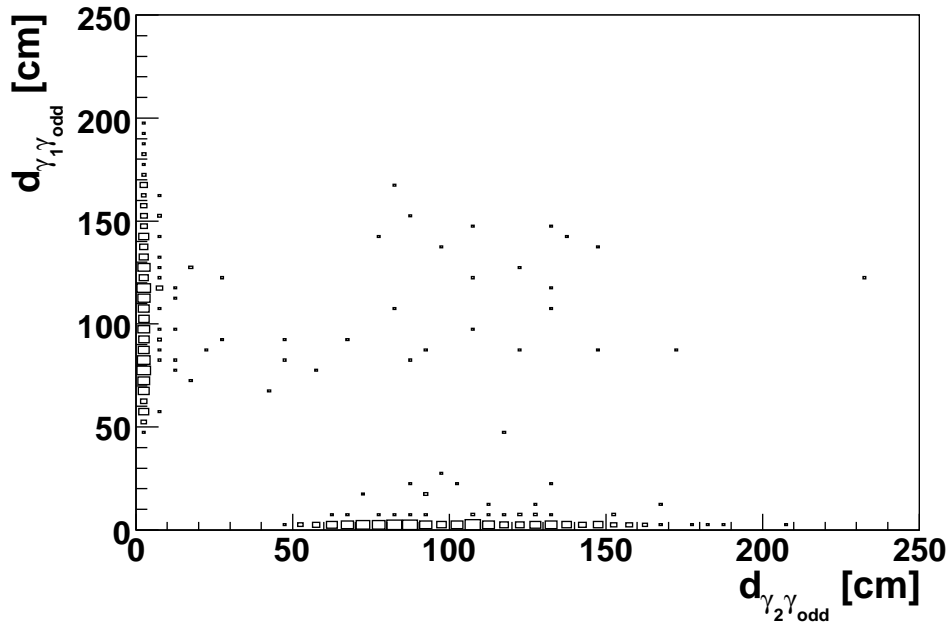


Figure 11.1: True generated distances between the odd photon and the π^0 decay photons, $\gamma_{1,2}$, for simulated $K^\pm \rightarrow \pi^\pm \pi^0 \gamma$ IB decays surviving all signal selection cuts.

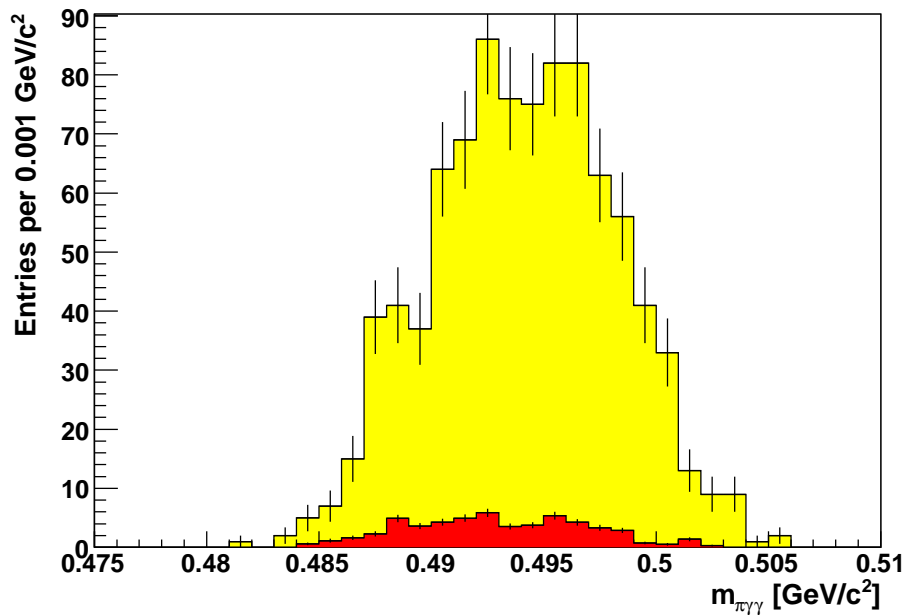


Figure 11.2: Reconstructed kaon mass of selected data (yellow area) and expected $K^\pm \rightarrow \pi^\pm \pi^0 \gamma$ IB background (red area).

Accidental Background

Accidental background appears when the decay products of two different kaon decays are detected in the time window assigned to the event. The event time was defined as the time associated to the pion track at the spectrometer. In the selection, the time difference required between the pion and each of the photons to be assigned to the same event had to be less 6 ns. The amount of accidental background was estimated by removing this requirement and looking at the side bands of the resulting time difference distribution, which then defined a control region. The number of events in these side bands should consist of resolution tails proportional to the number of events in the signal region and of accidental background. Following this procedure, and after finding only one event out of the 6 ns signal region, the estimated accidental background was 0.8 ± 0.8 events.

After considering all the background sources, the total amount of background estimated to remain in the selected 908 $K^\pm \rightarrow \pi^\pm \gamma \gamma$ candidates sample was 7.7%, with about 7.3% $K^\pm \rightarrow \pi^\pm \pi^0 \gamma$ IB decays, and the other contributions below the percent level. Note that as stated in Section 7.2.3, the expected background from $K^\pm \rightarrow \pi^\pm \pi^0 \gamma$ INT interferes negatively with the IB and DE contributions and was, therefore, subtracted from the total $K^\pm \rightarrow \pi^\pm \pi^0 \gamma$ background. Table 11.2 summarizes the expected background in the three super samples together. Figure 11.2 shows the reconstructed kaon mass of the selected signal candidates (yellow area), together with the expected background contribution from $K^\pm \rightarrow \pi^\pm \pi^0 \gamma$ IB decays (red area).

11.3 Measurement of $BR(K^\pm \rightarrow \pi^\pm \gamma \gamma, z \geq 0.2)$

A model independent measurement of $BR(K^\pm \rightarrow \pi^\pm \gamma \gamma)$ for the di-photon mass region corresponding to $z = m_{\gamma\gamma}^2/m_K^2 \geq 0.2$ is presented in this section. To perform this measurement, the quantities involved in Eq. 11.0.1 had to be evaluated avoiding dependencies on kinematic variables which characterize the dynamics of the signal decay. As a three body decay, $K^\pm \rightarrow \pi^\pm \gamma \gamma$ has two independent kinematic variables. The variables most commonly used are y and z , as defined in Eq. 3.3.3. Of these two variables, only z is dynamically relevant, since the differential branching ratio is symmetric in y .

Re-writing the branching ratio of $K^\pm \rightarrow \pi^\pm \gamma \gamma$ in bins of z :

$$BR(K^\pm \rightarrow \pi^\pm \gamma \gamma, z) = \frac{1}{\Phi_K} \left[\frac{N^{\text{selected}}(z) - N^{\text{background}}(z)}{\alpha_{\pi^\pm \gamma \gamma}(z) \cdot \epsilon_{\pi^\pm \gamma \gamma}(z)} \right], \quad (11.3.1)$$

with $N^{\text{selected}}(z)$, $N^{\text{background}}(z)$, $\alpha_{\pi^\pm \gamma \gamma}(z)$ and $\epsilon_{\pi^\pm \gamma \gamma}(z)$ evaluated for each z in. In the following sections, the measurement of all these quantities in bins of size 0.01 in z is presented. A differential branching ratio was then evaluated for each bin, and all results were afterwards added to obtain $BR(K^\pm \rightarrow \pi^\pm \gamma \gamma, z \geq 0.2)$.

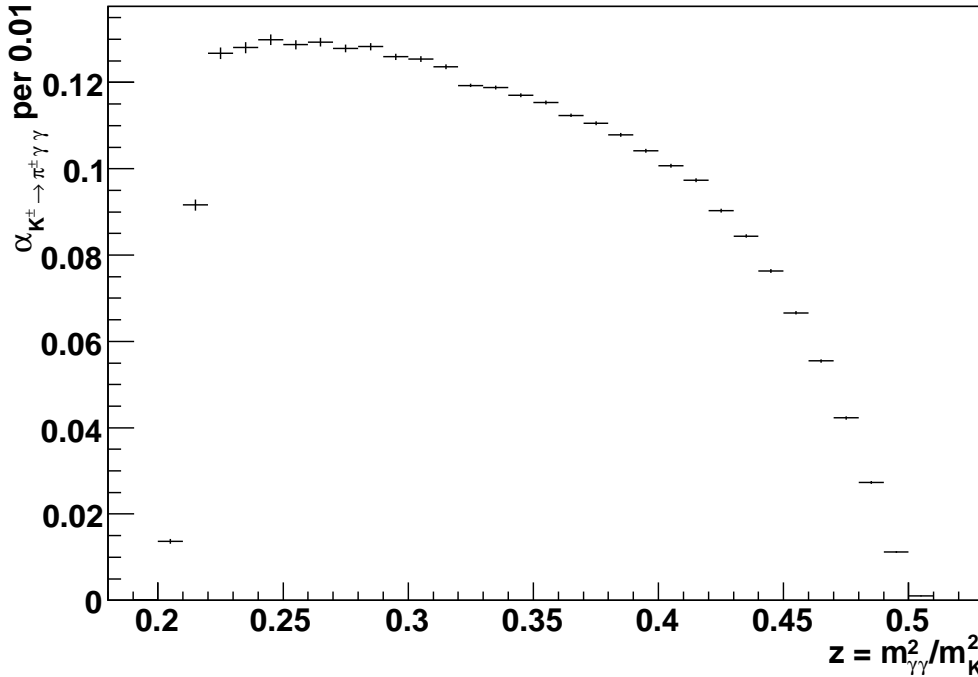


Figure 11.3: Acceptance of $K^\pm \rightarrow \pi^\pm \gamma\gamma$ as a function of $z = m_{\gamma\gamma}^2/m_K^2$.

11.3.1 Signal Acceptance

As explained in Section 7.2.2, the Monte Carlo simulation of the signal followed the description by [37] and was generated with $\hat{c} = 1.74$. However, given that the measurement was done in bins of z , dependencies on the particular theoretical model used in the MC were eliminated.

The acceptance was calculated according to the following definition:

$$\alpha_{\pi^\pm \gamma\gamma}(z) = \frac{N^{rec}(z^{rec})}{N^{gen}(z^{true})}. \quad (11.3.2)$$

In this equation, z^{true} are the true theoretical values for z as provided by the MC generator without applying any detector resolution smearing, and z^{rec} are the values of z obtained after reconstruction effects were taken into account.

Figure 11.3 shows the results of the acceptance obtained for each bin of z . The error bars in each bin follow binomial statistics.

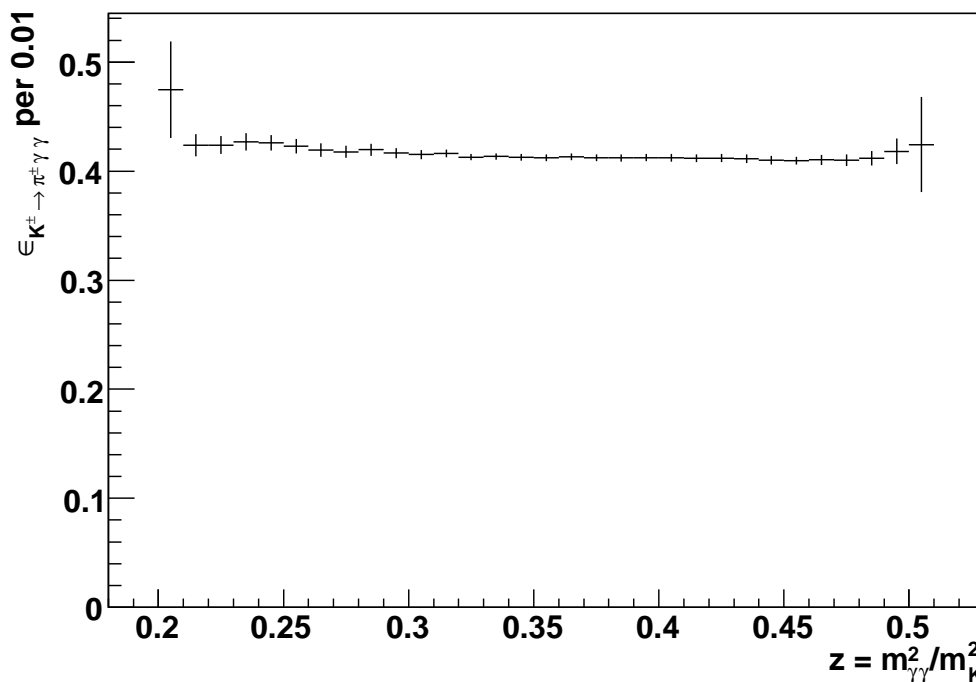


Figure 11.4: L1 \times L2 Efficiencies of $K^\pm \rightarrow \pi^\pm \gamma\gamma$ as a function of $z = m_{\gamma\gamma}^2/m_K^2$.

11.3.2 Trigger Efficiencies

According to the procedure explained in Chapter 9, both the L1 NTPEAK and the L2 MFAKE efficiencies were calculated for each bin of z as:

$$\epsilon_{\pi^\pm \gamma\gamma}(z) = \frac{\int N^{\text{MC}}(\vec{v}, z) \cdot \epsilon_{\text{control}}(\vec{v}) \cdot d\vec{v}}{N^{\text{MC}}}, \quad (11.3.3)$$

where \vec{v} stands for the variables on which the corresponding trigger efficiency depends, $\epsilon_{\text{control}}(\vec{v})$ is the trigger efficiency of the corresponding control sample, and $N^{\text{MC}}(\vec{v}, z)$ is the \vec{v} distribution as a function of z for MC signal events.

The total efficiency of the L1 and L2 triggers as a function of z , was then calculated assuming that the efficiencies of the L1 Q1/10 and LKrbias triggers were independent of z and using their values as listed in Table 9.1.

Figure 11.4 shows the results of the L1 \times L2 efficiencies obtained for each bin in z . The uncertainties quoted for the efficiencies contain only the statistical contribution from the MC signal in each bin.

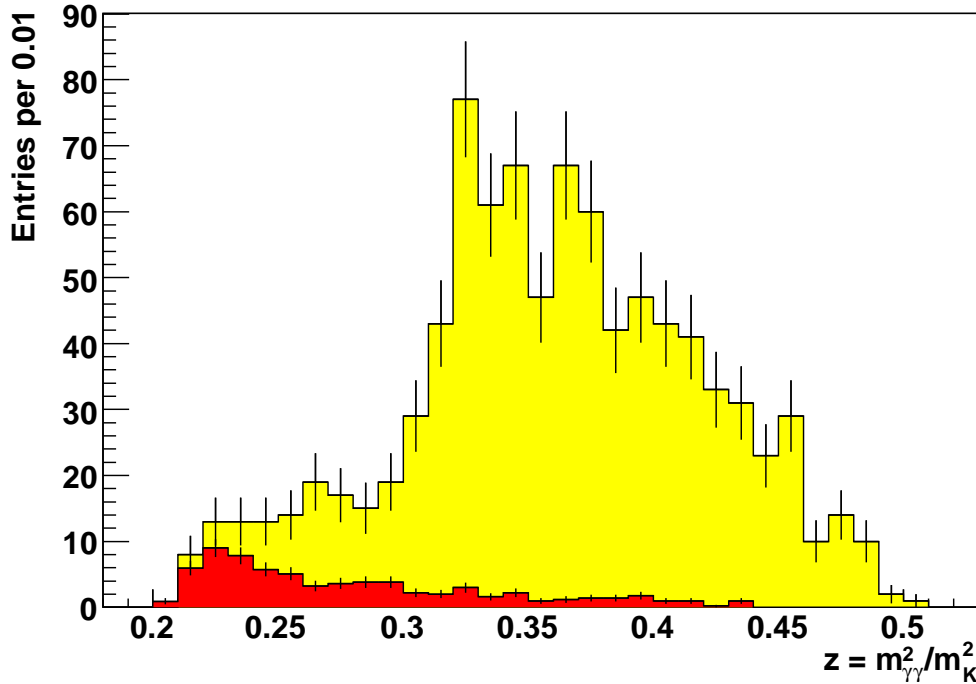


Figure 11.5: Reconstructed $z = m_{\gamma\gamma}^2/m_K^2$ of selected data (yellow area) and expected $K^\pm \rightarrow \pi^\pm \pi^0 \gamma$ IB simulated background (red area).

11.3.3 Background Subtraction

As explained in Section 11.2, the total background expected for the complete z kinematic range was 7.7%, from which about 7.3% arose only from $K^\pm \rightarrow \pi^\pm \pi^0 \gamma$ IB decays.

A total of about 97 million $K^\pm \rightarrow \pi^\pm \pi^0 \gamma$ IB decays were generated in the acceptance region, out of which almost 600 survived all selection cuts. These events were then corrected by the trigger efficiency effects depending on their z , and normalized to the total number of estimated remaining background (including the 0.6% background from other channels, which was assumed to behave as $K^\pm \rightarrow \pi^\pm \pi^0 \gamma$ IB). The so estimated background was then subtracted from the data sample.

Figure 11.5 shows the signal candidates (yellow area) with the estimated background (red area) as a function of z . In the case of the background, only the statistical contribution of the MC sample was considered in the error bars (since the other contributions were common to all bins and therefore considered only in the final result).

11.3.4 Branching Ratio

Equation 11.3.1 was used to calculate $\Delta(\text{BR}) \equiv \text{BR}(\Delta z)$, for each bin of z , using the results from the previous sections as inputs.

Figure 11.6 and Table 11.3 show the results obtained for $\Delta(\text{BR})$. The uncertainty in each bin was calculated as the square root of the sum in quadrature of the single statistical contributions from the signal candidates, the expected background, the signal efficiency and the signal acceptance (all of them obtained by using gaussian statistics). The last four bins in Figure 11.6 were merged into one in Table 11.3, to reduce the statistical uncertainty arising from the low acceptance for $z > 0.49$ (Figure 11.3).

The sum of the single $\Delta(\text{BR})$ provided the measurement of the branching ratio for $z \geq 0.2$:

$$\text{BR}(K^\pm \rightarrow \pi^\pm \gamma \gamma, z \geq 0.2) = (1.018 \pm 0.038_{\text{stat}} \pm 0.004_{\text{ext}}) \cdot 10^{-6}, \quad (11.3.4)$$

where

$$0.038_{\text{stat}}^2 = 0.037_{\text{data}}^2 + 0.006_{\text{backg}}^2 + 0.001_{\alpha}^2 + 0.006_{\epsilon}^2 + 0.004_{\Phi}^2.$$

σ_{ext} is the external uncertainty from $\text{BR}(K^\pm \rightarrow \pi^\pm \pi^0) \cdot \text{BR}(\pi^0 \rightarrow \gamma \gamma)$, and σ_{Φ} is the statistical uncertainty from the flux measurement. The negative BR in the first bin is due to the absence of signal candidates in this bin but background expectation different from zero. This bin was also considered in the total BR, to avoid a bias in the measurement by neglecting negative fluctuations.

11.4 Analysis of Systematic Uncertainties

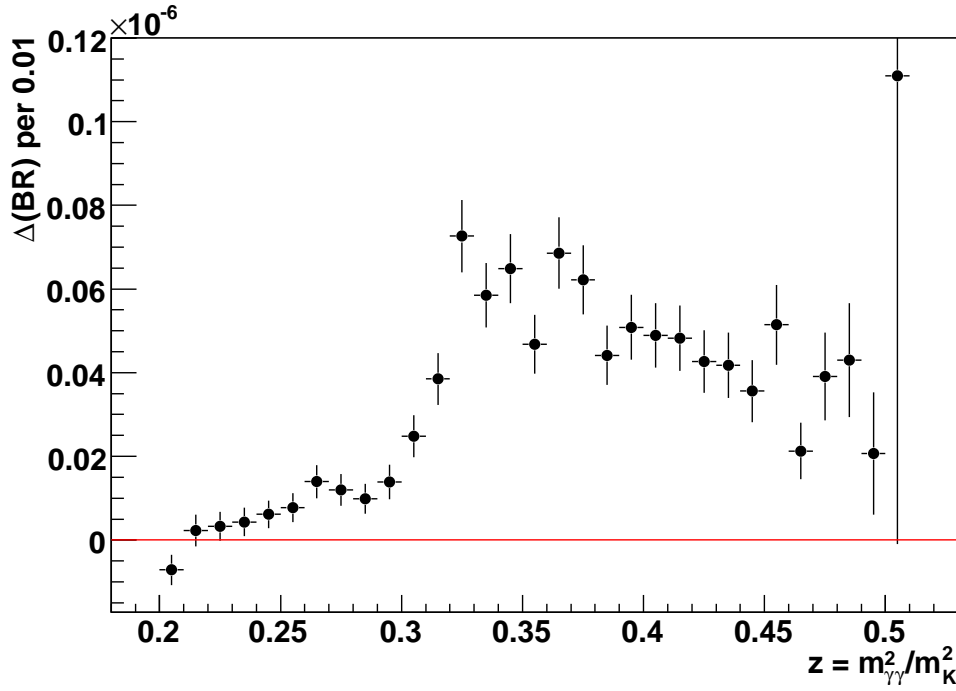
Systematic uncertainties intend to give an estimate of the precision of the measurement independently of the statistics available for it.

By varying the selection cuts, the inaccurate description of the MC of the most relevant variables used in the selection was studied as a source of systematic uncertainties. Also systematics arising from the efficiency measurement and the flux determination were studied and are summarized in this section.

11.4.1 Systematics from the Selection

Systematic effects were assumed to be independent on the z -bin, and were studied for the complete spectrum.

A reference BR, $\text{BR}(\text{ref})$, was calculated using Eq. 11.0.1. Note that the so calculated BR is a model dependent measurement, since the acceptance of the signal is calculated using a given theoretical description. Monte Carlo signal


 Figure 11.6: $\Delta(\text{BR})$ as a function of $z = m_{\gamma\gamma}^2/m_K^2$.

$z = m_{\gamma\gamma}^2/m_K^2$	$\Delta(\text{BR})(\cdot 10^{-9})$	$z = m_{\gamma\gamma}^2/m_K^2$	$\Delta(\text{BR})(\cdot 10^{-9})$
0.20 - 0.21	-7.11 ± 3.63	0.35 - 0.36	46.82 ± 7.02
0.21 - 0.22	2.27 ± 3.81	0.36 - 0.37	68.60 ± 8.58
0.22 - 0.23	3.25 ± 3.49	0.37 - 0.38	62.20 ± 8.27
0.23 - 0.24	4.29 ± 3.40	0.38 - 0.39	44.16 ± 7.09
0.24 - 0.25	6.12 ± 3.31	0.39 - 0.40	50.86 ± 7.77
0.25 - 0.26	7.72 ± 3.46	0.40 - 0.41	48.94 ± 7.68
0.26 - 0.27	13.96 ± 3.97	0.41 - 0.42	48.24 ± 7.76
0.27 - 0.28	11.98 ± 3.83	0.42 - 0.43	42.69 ± 7.50
0.28 - 0.29	9.88 ± 3.58	0.43 - 0.44	41.77 ± 7.80
0.29 - 0.30	13.86 ± 4.11	0.44 - 0.45	35.60 ± 7.43
0.30 - 0.31	24.82 ± 5.05	0.45 - 0.46	51.44 ± 9.57
0.31 - 0.32	38.49 ± 6.21	0.46 - 0.47	21.27 ± 6.73
0.32 - 0.33	73.62 ± 8.68	0.47 - 0.48	39.11 ± 10.47
0.33 - 0.34	58.50 ± 7.74	0.48 - 0.49	43.01 ± 13.63
0.34 - 0.35	64.89 ± 8.25	0.49 - 0.53	47.98 ± 27.70

 Table 11.3: Partial $K^\pm \rightarrow \pi^\pm \gamma\gamma$ branching fractions as a function of $z = m_{\gamma\gamma}^2/m_K^2$. Note that the last four bins were merged to reduce the statistical uncertainty.

simulation with $\hat{c} = 1.74$ (Section 7.2.2) was used, and provided an acceptance of $(9.222 \pm 0.001) \times 10^{-2}$.

The total branching ratio $BR(\text{ref})$ obtained was:

$$BR(K^\pm \rightarrow \pi^\pm \gamma \gamma, O(p^6), \hat{c} = 1.74) = (1.005 \pm 0.037_{\text{stat}}) \cdot 10^{-6}, \quad (11.4.1)$$

with σ_{stat} containing the statistical contributions.

The stability of $BR(\text{ref})$ was then studied by varying one selection criteria at a time both in data and in MC, and measuring the resulting acceptances, efficiencies, background and flux, which then provided a new BR, $BR(\text{new})$. For each $BR(\text{new})$, uncorrelated errors with respect to $BR(\text{ref})$ were calculated as:

$$\sigma_{\text{uncorr}}^{\text{new}} = \sqrt{\left| \left(\frac{\sigma_{\text{stat}}^{\text{BR}(\text{ref})}}{BR(\text{ref})} \right)^2 - \left(\frac{\sigma_{\text{stat}}^{\text{BR}(\text{new})}}{BR(\text{new})} \right)^2 \right|} \times BR(\text{new}), \quad (11.4.2)$$

while the error on $BR(\text{ref})$ was kept to be the initial statistical uncertainty $\sigma_{\text{stat}}^{\text{BR}(\text{ref})} = 0.037$. From the study of the variation of the results with respect to the reference measurement, relative systematic uncertainties were extracted and applied to the model independent result (Section 11.5).

The systematic uncertainties arising from the variation of the following selection criteria were studied:

- **Distance between pion impact point in LKr and photon clusters.** Shower fluctuations created by pions in the electromagnetic calorimeter contain clusters which can be misidentified as photon candidates. To study the implications of this effect in the measurement, the minimum distance required between the pion and a photon candidate, $d_{\pi-\gamma}^{\text{min}} > 30$ cm, was varied in the selection (Figure 11.7 (top left)). No systematic deviation was observed.
- **The pion identification.** The selection criteria required $(E/p)^{\text{max}} < 0.8$ c to reject any decay containing an electron in the final state. This condition was varied between 0.7 c and 0.9 c (Fig. 11.7 (top right)), with negligible effect observed in the measurement.
- **Allowed z -decay vertex region.** The maximum allowed z_{vertex} was changed from 7000 cm to 4000 cm (Figure 11.7 (bottom left)). The statistical reduction of the data increases the size of the uncorrelated error bars with decreasing $z_{\text{vertex}}^{\text{max}}$. A small deviation of the measurement towards higher values is observed in the figure, and a relative systematic uncertainty of $\pm 2\%$ was associated to the measurement. This effect is due to the slight disagreement between data and MC for high z_{vertex} values shown in Figures 10.6 (top) and 10.3 (top).

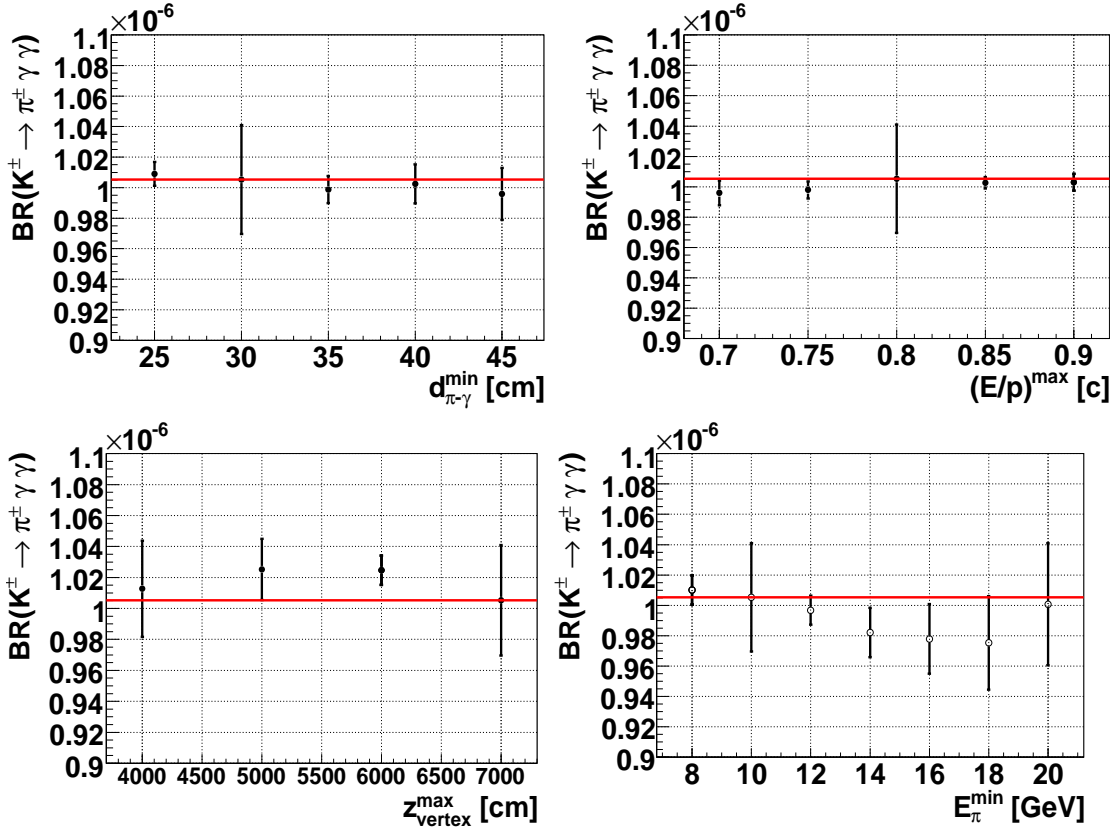


Figure 11.7: Variation in $\text{Br}(K^\pm \rightarrow \pi^\pm \gamma \gamma)$ as a function of $d_{\pi-\gamma}^{\text{min}}$ (top left), $(E/p)^{\text{max}}$ (top right), $z_{\text{vertex}}^{\text{max}}$ (bottom left), and E_π^{min} (bottom right). Statistical errors are used for the reference measurement, while uncorrelated errors are used for the new measurements.

- Minimum pion energy.** The minimum energy of the pion track $E_\pi^{\text{min}} = 10$ GeV was varied between 8 and 20 GeV (Figure 11.7 (bottom right)). A relative systematic uncertainty of $\pm 2.4\%$ due to the disagreement in the region around 15 GeV with the reference value was assigned. As shown in Figures 10.5 (top) and 10.2 (top), this corresponds exactly to the region where some disagreement between data and MC remained even after trigger efficiency corrections were applied.
- Minimum photon energy.** The value of this cut was varied from 4 to 16 GeV. The corresponding results are plotted in Figure 11.8 (left). Since all the measurements are flatly distributed, fluctuations were assumed to be of statistical nature.
- Energy scale.** The absolute energy scale factor of the electromagnetic calorimeter was measured in special runs where $\eta \rightarrow 2\gamma$ and $\eta \rightarrow 3\pi^0$ decays are studied. This factor is known to a precision of $\sim 0.1\%$ and is

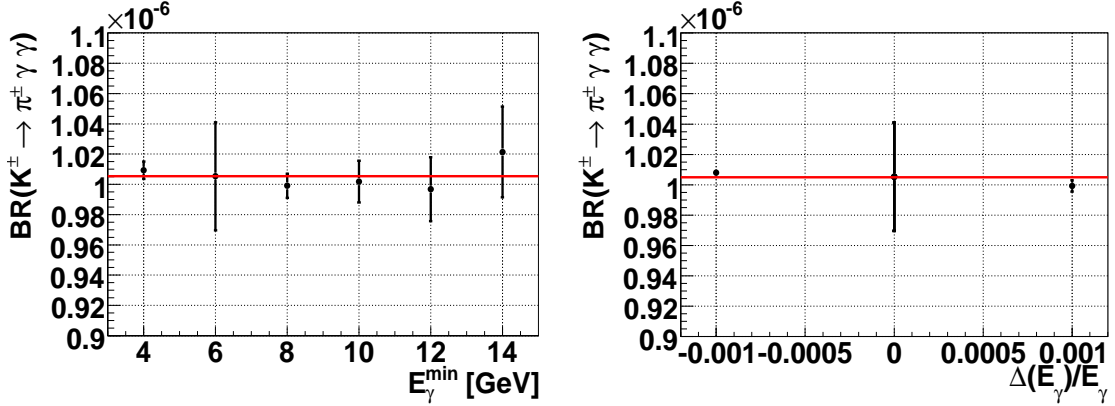


Figure 11.8: Variation in $Br(K^\pm \rightarrow \pi^\pm \gamma \gamma)$ as a function of E_γ^{min} (left) and of the LKr energy scale (right). Statistical errors are used for the reference measurement, while uncorrelated errors are used for the new measurements.

crucial for the correct reconstruction of the photon clusters. The energy of the clusters as provided by the detector was varied in $\pm 0.1\%$ and the selection criteria were applied. The results are shown in Figure 11.8 (right). No significant systematic deviation was observed.

- **LKr non-linearity.** Non linearity effects between the energy deposited in the calorimeter and its actual value were investigated and found to be negligible, since these effects are only noticeable for energies around 3 GeV, and the minimum energy of the photons was required to be 6 GeV in the selection.

11.4.2 Systematics from the Efficiency Measurement

The correctness of the assumptions made in order to measure the efficiencies of the signal and normalization channels is checked in the following sections.

- **The direct efficiency measurement vs. the (indirect) weighting procedure.** Both methods were used to measure the trigger efficiency of the NTPEAK trigger for $K^\pm \rightarrow \pi^\pm \pi^0$ decays. The direct measurement using $K^\pm \rightarrow \pi^\pm \pi^0$ data, provided a value of $(57.67 \pm 0.02)\%$, with the error being only statistical. The measurement was repeated by calculating the efficiency of the same data as a function of the pion energy, and weighting with the corresponding MC $K^\pm \rightarrow \pi^\pm \pi^0$ distribution as described in Eq. 9.1.2. The result from this measurement was $(57.71 \pm 0.02)\%$, which gives a negligible relative systematic uncertainty of $\pm 0.07\%$ to be associated with the weighting procedure for measuring efficiencies. Figure 11.9 (left) shows the agreement between the two efficiency measurements as a function of the energy of the pion. The slight disagreement for low pion energies is due

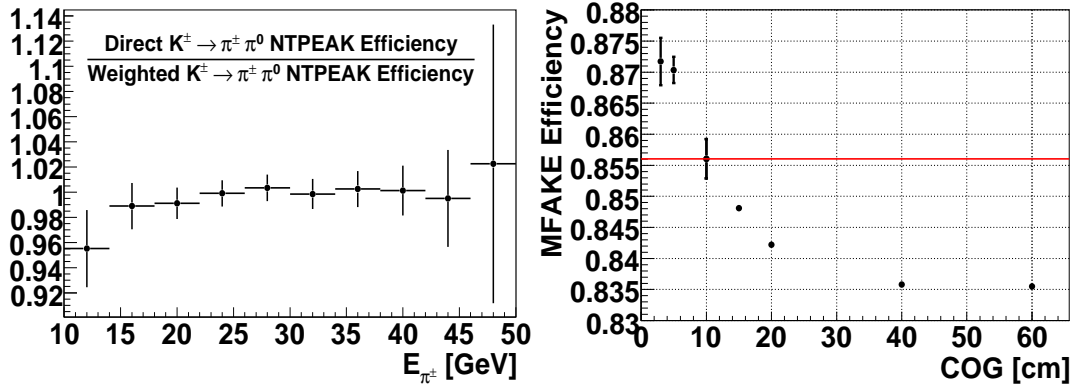


Figure 11.9: (Left) Comparison of the direct and MC weighting measurements of the efficiency of the NTPEAK trigger for $K^\pm \rightarrow \pi^\pm \pi^0$ decays as a function of the energy of the pion. (Right) Variation of MFAKE efficiency for signal events as a function of COG .

to the poor description of the MC for that region (Figures 10.5 (top) and 10.2 (top)).

- The MFAKE efficiency measurement.** Given the low statistics of the signal channel, events with a pion and two photons in the final state were used as a control sample for this measurement (see Section 9.2.5). Further requirements on the control sample were imposed, by enforcing or relaxing the cut on the center of gravity of the events (Figure 11.9 (right)). A systematic deviation towards higher (or lower) efficiency values was observed when enforcing (or relaxing) the center of gravity requirement. This is explained by the fact that asking for smaller values of this variable, is similar to rejecting events with high missing energy, in particular $K^\pm \rightarrow \pi^\pm \pi^0 \pi^0$ decays (see Fig. 8.10), thus changing the composition of the control sample and its distribution in pion momentum and vertex. Moreover, correlations between the NTPEAK trigger used to select the control sample events and the MFAKE trigger appear, since the NTPEAK efficiency decreases when removing the $K^\pm \rightarrow \pi^\pm \pi^0 \pi^0$ contribution. A $\pm 1.8\%$ relative systematic uncertainty was assigned to this effect.
- The Binning.** The MFAKE efficiency was computed from a control sample of about 65000 events distributed in a 3D matrix in the variables $z_{vertex}^{charged}$, r_π^{DCH1} and E_π (Section 9.2.5). It was checked, whether different binnings with different statistical significance affected the efficiency measurement. A negligible relative systematic uncertainty of $\pm 0.1\%$ was found. Results are summarized in Table 11.4.

Binning	MFAKE Efficiency
$5 \times 5 \times 5$	0.8571 ± 0.0031
$10 \times 10 \times 10$ (reference)	0.8560 ± 0.0031
$15 \times 15 \times 15$	0.8550 ± 0.0032

Table 11.4: MFAKE efficiency for different binnings.

Period	$N_{\pi^\pm \pi^0}$	$\alpha_{\pi^\pm \pi^0}$	$\epsilon_{\pi^\pm \pi^0}$	$\Phi_K(10^9)$
SS1	17690	0.13432 ± 0.00021	0.996961 ± 0.000037	$6.475 \pm 0.049_{\text{stat}}$
SS2	24044	0.11137 ± 0.00017	0.996893 ± 0.000039	$10.605 \pm 0.068_{\text{stat}}$
SS3	8852	0.11151 ± 0.00021	0.997300 ± 0.000046	$3.901 \pm 0.041_{\text{stat}}$
SS1-2-3	50586	0.11832 ± 0.00011	0.997020 ± 0.000023	$21.018 \pm 0.093_{\text{stat}}$

 Table 11.5: Summary of the kaon fluxes and related quantities in the different super sample periods obtained using CPRE · Q1/100 as trigger for $K^\pm \rightarrow \pi^\pm \pi^0$ events.

11.4.3 Systematics from the Flux Measurement

To check the stability of the flux measurement, $K^\pm \rightarrow \pi^\pm \pi^0$ data were collected from the CPRE trigger. In particular, only events which fired the Q1/100 condition were accepted (total downscaling $D = 10000$). The fluxes obtained for the different super samples are summarized in Table 11.5.

The total flux obtained was:

$$\begin{aligned}
 \Phi_K &= (21.018 \pm 0.0913_{\text{data}} \pm 0.0191_\alpha \pm 0.0005_\epsilon \pm 0.118_{\text{ext}}) \cdot 10^9 \\
 &= (21.018 \pm 0.093_{\text{stat}} \pm 0.118_{\text{ext}}) \cdot 10^9.
 \end{aligned}
 \tag{11.4.3}$$

From the comparison with the result obtained in Eq. 11.1.3, a significant shift is observed towards higher values for the flux using CPRE as a trigger. The reason for this, is that while the efficiency of CPRE · Q1/100 was almost 100% and very easy to measure, the efficiency of NTPEAK was very low for $K^\pm \rightarrow \pi^\pm \pi^0$ decays, depending also on the energy of the charged pion. However, in order to cancel systematic effects with the signal in the branching ratio measurement, the use of NTPEAK as a $K^\pm \rightarrow \pi^\pm \pi^0$ trigger was preferred. A relative systematic uncertainty of $\pm 1.7\%$ was associated to the flux measurement.

11.5 Summary

All uncertainties associated to the branching ratio measurement are summarized in Tables 11.6 and 11.7. Statistical and systematic uncertainties are of the same order or magnitude.

The biggest contributions to the systematic uncertainty arise from the Monte Carlo reconstruction of the pion energy spectrum and the decay vertex position, followed by the trigger efficiency determination and the flux measurement. The origin of the single uncertainties was treated in previous sections.

The statistical uncertainty in the measurement comes from the low amount of signal candidates found in the super sample periods 1, 2 and 3 of the 2003 data taking. This amounts to approximately 40% of the total available statistics for this channel considering all the data collected by the experiment during the year 2003. The use of all the available data, would not only reduce the statistical uncertainty in the measurement, but also allow to perform a measurement of the trigger efficiencies with real signal candidates, reducing thus the systematic uncertainty on the trigger efficiency determination.

Considering the different uncertainties, the branching ratio measurement of $K^\pm \rightarrow \pi^\pm \gamma \gamma$ decays for $z \geq 0.2$ results:

$$\text{BR}(K^\pm \rightarrow \pi^\pm \gamma \gamma, z \geq 0.2) = (1.018 \pm 0.038_{\text{stat}} \pm 0.039_{\text{syst}} \pm 0.004_{\text{ext}}) \cdot 10^{-6}, \quad (11.5.1)$$

with σ_{syst} the square root of the single systematic uncertainties quoted in Table 11.6 added in quadrature, and σ_{stat} and σ_{ext} the statistical and external uncertainty, respectively.

Summary of Systematics Uncertainties	$\sigma(\text{BR})/\text{BR}$
Selection Criteria:	
Distance Pion-Photon at LKr ($d_{\pi-\gamma}$)	—
Pion Identification (E/P)	—
Decay Vertex	$\pm 2.00\%$
Pion Energy (E_π)	$\pm 2.40\%$
Photon Energy (E_γ)	—
LKr Energy Scale	—
LKr Energy Non-linearities	—
Efficiency Measurement:	
Direct Measurement vs. Weighting Procedure	$\pm 0.07\%$
MFAKE Efficiency	$\pm 1.80\%$
MFAKE Matrix Binning	$\pm 0.10\%$
Flux Measurement:	
$K^\pm \rightarrow \pi^\pm \pi^0$ from CPRE-Q1/100	$\pm 1.70\%$
External:	
$BR(K^\pm \rightarrow \pi^\pm \pi^0), BR(\pi^0 \rightarrow \gamma \gamma)$	$\pm 0.44\%$
Total Systematics Uncertainty	$\pm 4.01\%$

Table 11.6: Summary of systematic and external uncertainties investigated for the branching ratio measurement. The sign ‘—’ means that no systematic uncertainty was assigned for the corresponding effect.

Summary of Statistical Uncertainties	$\sigma(\text{BR})/\text{BR}$
Signal:	
Data	$\pm 3.63\%$
Background Expectation	$\pm 0.59\%$
MC Acceptance	$\pm 0.10\%$
Trigger Efficiency	$\pm 0.59\%$
Total	$\pm 3.73\%$
Normalization:	
Data	$\pm 0.04\%$
MC Acceptance	$\pm 0.09\%$
Trigger Efficiency	$\pm 0.35\%$
Total	$\pm 0.36\%$
Total Statistical Uncertainty	$\pm 3.77\%$

Table 11.7: Summary of uncertainties of statistical and external nature in the branching ratio measurement.

12 Fit to $z = m_{\gamma\gamma}^2/m_K^2$

The measured branching ratio and the shape of the $z = m_{\gamma\gamma}^2/m_K^2$ spectrum can be used to extract a value for the parameter \hat{c} . The measurement of this parameter is not only important to constrain and test the underlying theory, but it can also be used to extract a model dependent branching ratio for the region with $z < 0.2$, not accessible from the NA48/2 data.

12.1 $O(p^6)$ ChPT Theory

As explained in Section 3.3, the differential decay rate of $K^\pm \rightarrow \pi^\pm\gamma\gamma$ in the framework of Chiral Perturbation Theory reads [47]:

$$\frac{\partial^2\Gamma}{\partial y\partial z} = \frac{M_K}{2^9\pi^3} \left[z^2(|A+B|^2 + |C|^2) + \left(y^2 - \frac{1}{4}\lambda(1, r_\pi^2, z) \right)^2 \cdot (|B|^2 + |D|^2) \right], \quad (12.1.1)$$

with $\lambda(a, b, c) = a^2 + b^2 + c^2 - 2(ab + bc + ca)$, $r_\pi = M_\pi/M_K$, $y = p \cdot (q_1 - q_2)/M_K^2$, $z = (q_1 + q_2)^2/M_K^2$. The variables p , q_1 and q_2 stand for the four momenta of the kaon and each of the two photons, respectively. The variables y and z are defined in the regions $0 \leq |y| \leq \frac{1}{2}\lambda^{\frac{1}{2}}(1, r_\pi^2, z)$ and $0 \leq z \leq (1 - r_\pi)^2$.

At order $O(p^6)$ [37], and considering only pole contributions due to the pseudoscalar meson octet [47], the amplitude $D(z)$ vanishes and the amplitudes $A(z, y)$, $B(z)$ and $C(z)$ get the values of Equations 3.3.18, 3.3.18 and 3.3.11, respectively. To obtain the differential decay rate as a function of z , Equation 12.1.1 must be integrated over y .

Following this approach, three free parameters remain, η_1 , η_2 and \hat{c} , which are contained in the loop amplitude A . Neglecting vector meson contributions compared to unitarity correction effects [37, 38], only \hat{c} remains as a free parameter of the theory.

12.1.1 Fit

The $\Delta(\text{BR})$ distribution as a function of z obtained in Section 11.3.4, was fitted to the theoretical differential decay branching ratio resulting from the integration of Equation 12.1.1 over y , multiplied by the factor τ_{K^\pm}/\hbar .

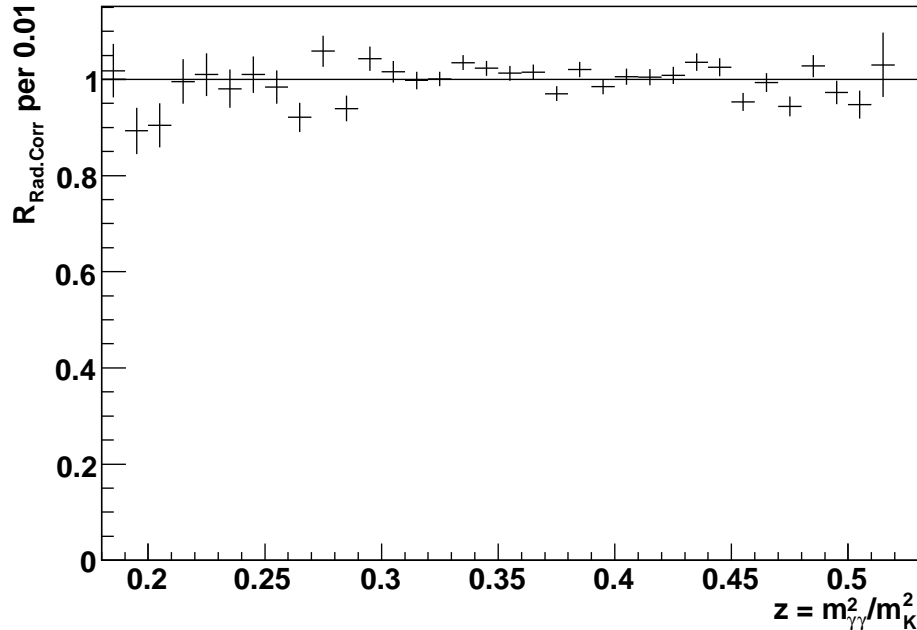


Figure 12.1: Radiative corrections applied to the fit function.

The method used to perform this fit was a χ^2 minimization of the signal data, to the $O(p^6)$ prediction by [37]. Radiative corrections were included in the theory using the ratio

$$R_{\text{Rad.Corr.}} = \frac{N_{\text{Rad.Corr.}}^{\text{gen}}(z^{\text{true}})}{N_{\text{No Rad.Corr.}}^{\text{gen}}(z^{\text{true}})}. \quad (12.1.2)$$

To calculate this ratio, two sets of 100,000 MC $K^\pm \rightarrow \pi^\pm \gamma\gamma$ events with $\hat{c} = 1.74$ were generated (Sec. 7.2.2). One set included radiative corrections at generation level, $N_{\text{Rad.Corr.}}^{\text{gen}}(z^{\text{true}})$, and the other one was generated without them, $N_{\text{No Rad.Corr.}}^{\text{gen}}(z^{\text{true}})$. The results from this ratio are shown in Figure 12.1 and were used to correct the theoretical function, in order to describe the real behavior of the data. The errors were calculated assuming two independent sets of data and computing the error of the ratio for each bin. These errors were also propagated to the fit function.

The result from the one parameter fit to the z spectrum is shown in Figure 12.2. The fit was performed in the region $z = [0.21, 0.50[$, and the result obtained was

$$\hat{c} = 1.54 \pm 0.15 \quad (12.1.3)$$

The quality of the fit was $\chi^2/n_{\text{dof}} = 28.37/28$. The values of the different constants involved in the fit (used without errors) are listed in Table 12.1.

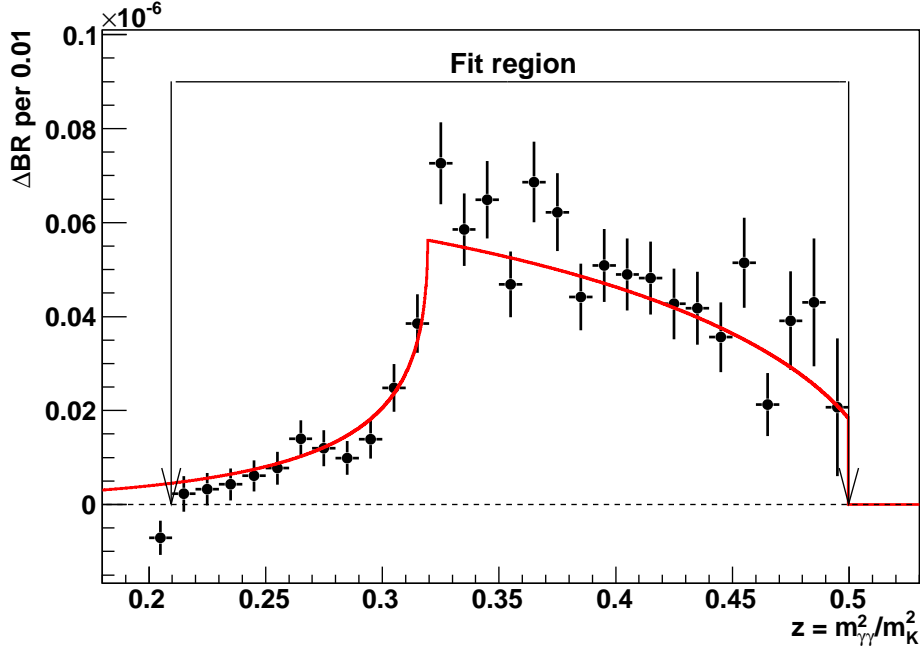


Figure 12.2: Fit of $O(p^6)$ in ChPT [37] (red line) to the experimental data (dots). The red line shows the result of the one parameter fit to \hat{c} , which provided a result of $\hat{c} = 1.54 \pm 0.15$ with $\chi^2/n_{\text{dof}} = 28.37/28$.

$m_\rho = 0.7755 \text{ GeV}/c^2$ [108]	$\alpha_3 = -7.36 \cdot 10^{-8}$ [89]
$m_\eta = 0.54787 \text{ GeV}/c^2$ [3]	$\beta_1 = -25.68 \cdot 10^{-8}$ [89]
$m_{K^\pm} = 0.493677 \text{ GeV}/c^2$ [108]	$\beta_3 = -2.43 \cdot 10^{-8}$ [89]
$G_8 = 0.91 \cdot 10^{-5}$ [60]	$\gamma_3 = 2.26 \cdot 10^{-8}$ [89]
$\Gamma_{\pi^0} = 0.802 \cdot 10^{-8} \text{ GeV}$ [108]	$\zeta_1 = -0.47 \cdot 10^{-8}$ [89]
$m_{\pi^\pm} = 0.139570$ [108] GeV/c^2	$\xi_1 = -1.51 \cdot 10^{-8}$ [89]
$\alpha_1 = 91.71 \cdot 10^{-8}$ [89]	

Table 12.1: Input constants used in the fit to $O(p^6)$ ChPT as in ref. [37].

From the direct comparison between the branching ratio measurement for $z \geq 0.2$, $\text{BR}(z \geq 0.2) = (1.018 \pm 0.038_{\text{stat}}) \cdot 10^{-6}$ (Sect. 11.5), and the prediction of the theory including radiative corrections, $\text{BR}(O(p^6), \hat{c} = 1.54, z \geq 0.2) = 0.957 \cdot 10^{-6}$ (area between arrows in Fig. 12.2), a $1.6\sigma_{\text{stat}}$ deviation was observed. Even though the deviation is small, there is no perfect agreement between the theory and the measurement considering that the same statistics were involved in both the branching ratio measurement and the fit. The deviation is due to the dependence of the spectrum shape on \hat{c} , which means that \hat{c} would then not only be fixed by the branching ratio (purely statistics), but also by the spectrum shape, implying the possible existence of missing contributions in the theory.

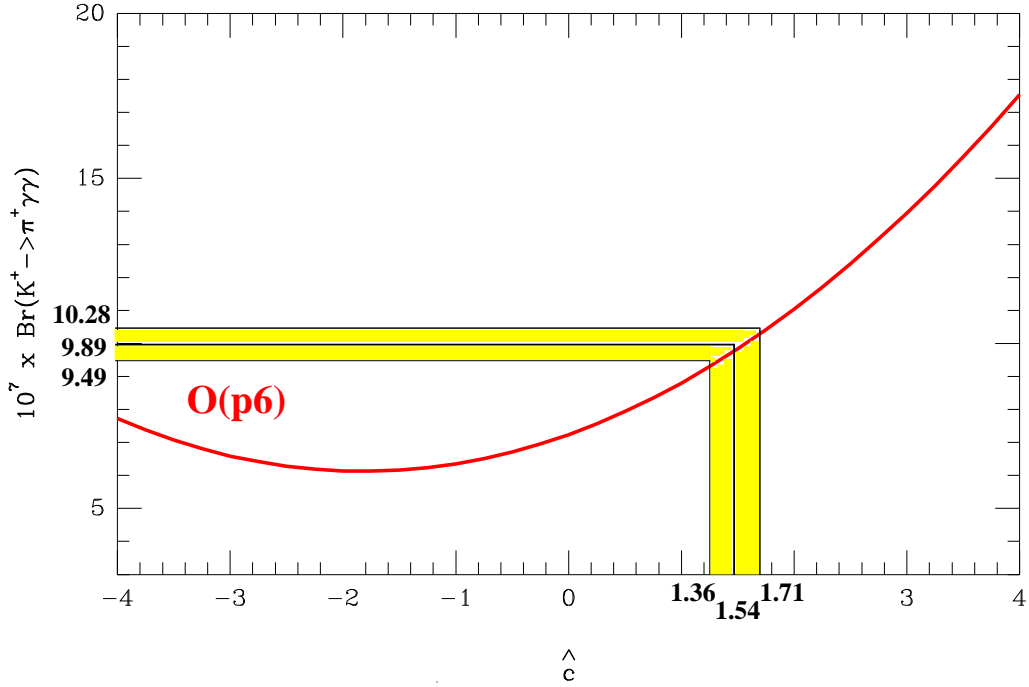


Figure 12.3: Theoretical $O(p^6)$ prediction of the dependence of the branching ratio as a function of \hat{c} [37]. The yellow areas show the one sigma systematic uncertainty regions.

12.1.2 Systematic Uncertainty on \hat{c}

To estimate the systematic uncertainty on the \hat{c} determination, the following procedure was followed.

The branching ratio predicted by the theory for the complete z spectrum was evaluated using the measured value of \hat{c} , $\text{BR}(O(p^6), \hat{c} = 1.54) = 0.9886 \cdot 10^{-6}$. The 4% relative systematic uncertainty of the branching ratio measurement for $z \geq 0.2$ (Eq. 11.5.1) was applied to the predicted total branching ratio, which was varied in $\pm 4\%$. The corresponding \hat{c} values associated to this branching ratio variations were then determined.

The deviation of the new values of \hat{c} with respect to the reference measurement defined the systematic uncertainty associated to \hat{c} , providing a final result of:

$$\hat{c} = 1.54 \pm 0.15_{\text{stat}} \pm 0.18_{\text{syst}} = 1.54 \pm 0.23 \quad (12.1.4)$$

Figure 12.3 shows the predicted relation between the branching ratio and \hat{c} according to [37] and illustrates the procedure followed. The yellow bands correspond to the one sigma relative systematic uncertainties.

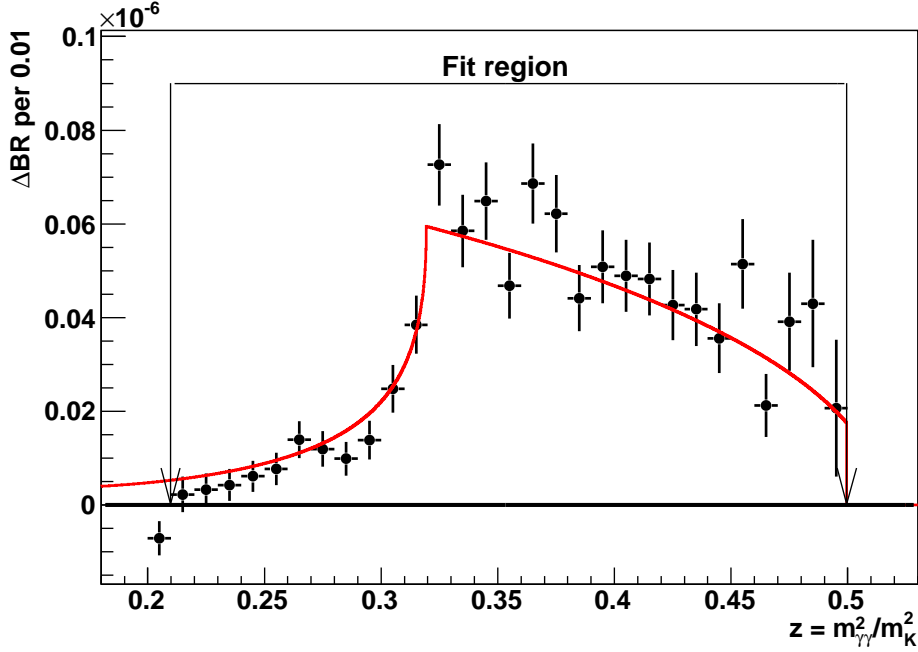


Figure 12.4: Fit of $O(p^6)$ ChPT [37] with $\eta - \eta'$ mixing and G27 contributions in $O(p^4)$ [60] (red line) to the experimental data (dots). The red line shows the result of the two parameters fit to \hat{c} and G_8^s/G_8 , which provided a result of $\hat{c} = 1.53 \pm 0.40$ and $G_8^s/G_8 = 0.03 \pm 0.30$ with $\chi^2/n_{\text{dof}} = 27.45/27$ and $\rho = -0.920$.

12.2 $O(p^6)$ ChPT with $\eta - \eta'$ mixing

As explained in Section 3.3.1, pole contributions due to $\eta - \eta'$ mixing appear at $O(p^4)$, together with non-negligible G_{27} contributions [60]. To consider these contributions in the $O(p^6)$ theory, the amplitude C of Eq. 12.1.1 was substituted by Eq. 3.3.14. As in Section 12.1, Eq. 12.1.1 was then integrated over y , to obtain the differential decay rate as a function of z , which multiplied by the factor τ_{K^\pm}/\hbar provided the corresponding differential branching ratio of the decay. As before, neglecting vector meson contributions compared to unitarity correction effects [37, 38], two free parameters remain in the theory, \hat{c} and G_8^s .

12.2.1 Fit

The $\Delta(\text{BR})$ data distribution, was fitted to the theoretical differential decay branching ratio obtained as described above, leaving both the parameter \hat{c} and the ratio G_8^s/G_8 free in the fit. The result from the two parameter fit to the z spectrum is shown in Figure 12.4.

$m_{\eta'} = 0.95778 \text{ GeV}/c^2$ [108] $\theta = -22$ [58] $G_{27}/G_8 = 0.05824176$ [60]
--

Table 12.2: Additional input constants used in the fit to $O(p^6)$ ChPT including $\eta - \eta'$ mixing and non negligible G_{27} effects in amplitude C [37, 60].

The fit was performed in the region $z = [0.21, 0.50[$, and the result obtained was

$$\begin{aligned}\hat{c} &= 1.53 \pm 0.40 \\ G_8^s/G_8 &= 0.03 \pm 0.30\end{aligned}\tag{12.2.1}$$

The quality of the fit was $\chi^2/n_{\text{dof}} = 27.45/27$ with a correlation coefficient $\rho = -0.920$. Following the procedure explained before, radiative corrections were included in the theory. The values of the additional constants involved in the fit are listed in Table 12.2.

From the direct comparison between the branching ratio measurement $\text{BR}(z \geq 0.2) = (1.018 \pm 0.038_{\text{stat}}) \cdot 10^{-6}$ (Section 11.5), and the prediction of the modified $O(p^6)$ theory for the same range using $\hat{c} = 1.53 \pm 0.40$ and $G_8^s/G_8 = 0.03 \pm 0.30$ as an input and including radiative corrections, $\text{BR}(O(p^6), \hat{c}, G_8^s, z \geq 0.2) = 0.960 \cdot 10^{-6}$ (area between arrows in Fig. 12.4), a $1.5\sigma_{\text{stat}}$ deviation was observed. This small deviation with respect to the theory, might again mean that there are non-negligible missing corrections in the theory of the decay. The large correlation factor between the two parameters explains the large error on \hat{c} , which is still compatible with the result obtained in Section 12.1, $\hat{c} = 1.54 \pm 0.15$. The result obtained for G_8^s/G_8 is compatible with zero.

12.3 Determination of $\text{BR}(K^\pm \rightarrow \pi^\pm \gamma\gamma)$

The total branching ratio for the complete $z = m_{\gamma\gamma}^2/m_K^2$ spectrum was determined by computing the branching ratio for the $z < 0.2$ region according to the $O(p^6)$ ChPT prediction by [37] and adding it to the measured result for $z \geq 0.2$ (Eq. 11.5.1).

The red area in Figure 12.5 shows the branching ratio predicted for $z < 0.2$ using the measured $\hat{c} = 1.54 \pm 0.15$ value. This branching ratio amounts to:

$$\text{BR}(K^\pm \rightarrow \pi^\pm \gamma\gamma, O(p^6), \hat{c} = 1.54, z < 0.2) = (0.037^{+0.003\hat{\sigma}_\hat{c}}_{-0.002\hat{\sigma}_\hat{c}}) \cdot 10^{-6},\tag{12.3.1}$$

where $\sigma_{\hat{c}}$ was calculated by varying \hat{c} within one standard deviation. Adding this result to Eq. 11.5.1, the branching ratio for the complete z spectrum was determined to be:

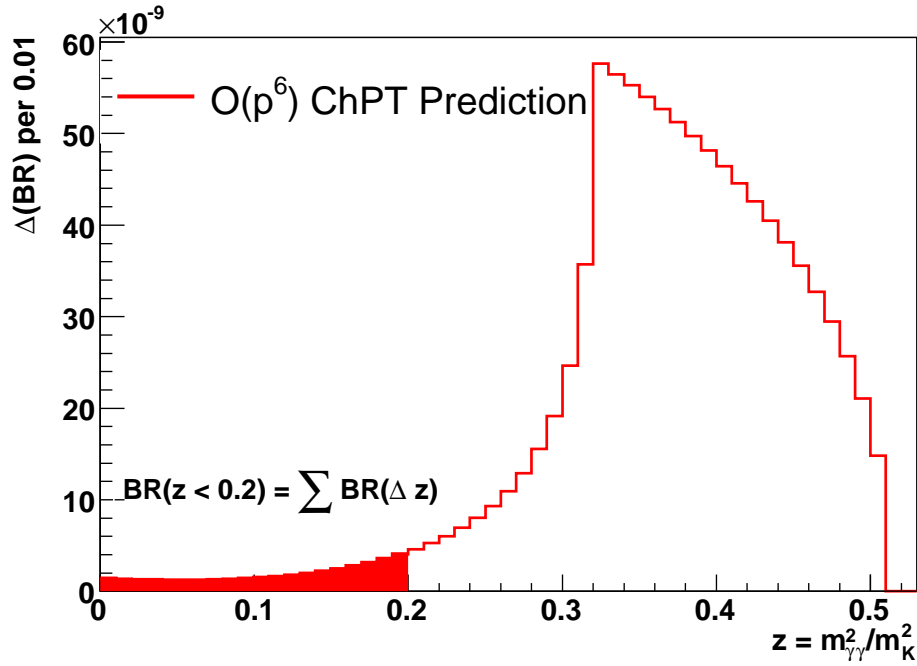


Figure 12.5: $O(p^6)$ ChPT prediction [37] of the z spectrum for $\hat{c} = 1.54$. The red area shows the model dependent branching ratio for $z < 0.2$.

$$BR(K^\pm \rightarrow \pi^\pm \gamma\gamma) = (1.055 \pm 0.038_{\text{stat}} \pm 0.039_{\text{syst}} \pm 0.004_{\text{ext}} \begin{smallmatrix} +0.003_{\hat{c}} \\ -0.002_{\hat{c}} \end{smallmatrix}) \cdot 10^{-6}, \quad (12.3.2)$$

which is to 96% a model independent $BR(K^\pm \rightarrow \pi^\pm \gamma\gamma)$ measurement.

13 Conclusions

13.1 Summary

About 40% of the data collected in the year 2003 by the NA48/2 experiment have been analyzed and 908 $K^\pm \rightarrow \pi^\pm \gamma \gamma$ candidates with about 8% background contamination have been selected in the region with $z = m_{\gamma\gamma}^2/m_K^2 \geq 0.2$. These decays and the normalization channel $K^\pm \rightarrow \pi^\pm \pi^0$ were collected through the NA48/2 neutral trigger chain intended for the collection of $K^\pm \rightarrow \pi^\pm \pi^0 \pi^0$ decays and therefore suffered from a very low trigger efficiency ($\approx 50\%$). Elaborate studies were performed to measure these efficiencies and correct for them.

The measurement of the differential branching ratio of $K^\pm \rightarrow \pi^\pm \gamma \gamma$ provided the following model independent result:

$$\text{BR}(K^\pm \rightarrow \pi^\pm \gamma \gamma, z \geq 0.2) = (1.018 \pm 0.038_{\text{stat}} \pm 0.039_{\text{syst}} \pm 0.004_{\text{ext}}) \cdot 10^{-6}$$

From the measurement of the branching ratio and spectrum, it was possible to determine a model dependent value of \hat{c} by fitting the experimental data to the $O(p^6)$ ChPT theoretical prediction by ref. [37]. The result obtained for \hat{c} was:

$$\hat{c} = 1.54 \pm 0.15_{\text{stat}} \pm 0.18_{\text{syst}}$$

Using the measured \hat{c} value and the $O(p^6)$ ChPT prediction, the branching ratio for $z = m_{\gamma\gamma}^2/m_K^2 < 0.2$ was computed and added to the measured branching ratio for $z \geq 0.2$. The value obtained for the total branching ratio was:

$$\text{BR}(K^\pm \rightarrow \pi^\pm \gamma \gamma) = (1.055 \pm 0.038_{\text{stat}} \pm 0.039_{\text{syst}} \pm 0.004_{\text{ext}} \pm^{+0.003}_{-0.002}_{\hat{c}}) \cdot 10^{-6}$$

This value is to 96% a model independent result obtained from the observed data. It is the most precise $\text{BR}(K^\pm \rightarrow \pi^\pm \gamma \gamma)$ measurement performed up to now, improving the precision of the only existing measurement by about a factor of five. The earlier measurement by the E787 experiment at BNL [82], was based on 31 event candidates with an estimated background of 5.1 ± 3.3 events and obtained a branching ratio of $\text{BR}(K^\pm \rightarrow \pi^\pm \gamma \gamma) = (1.10 \pm 0.32) \cdot 10^{-6}$ and $\hat{c} = 1.8 \pm 0.6$. Both branching ratio and \hat{c} results are compatible within their errors with the measurements presented in this thesis.

A measurement of the \hat{c} parameter was also extracted from the first observation of the $K^\pm \rightarrow \pi^\pm e^+ e^- \gamma$ decay by NA48/2 [22]. This decay is similar to $K^\pm \rightarrow \pi^\pm \gamma \gamma$ with one photon internally converting into a pair of electrons. A value of $\hat{c} = 0.90 \pm 0.45$ was obtained from that measurement, which is about 1.4σ away from the value presented in this thesis. However, given the high quality of the fit to the $K^\pm \rightarrow \pi^\pm e^+ e^- \gamma$ decays, $\chi^2/n_{dof} = 8.1/17$, the χ^2 would be almost equally good for the result of \hat{c} obtained in this thesis, bringing both results in even better agreement.

Considering that the same statistics have been involved both in the branching ratio measurement and in the fit to extract the \hat{c} parameter, a slight disagreement between the $O(p^6)$ ChPT branching ratio prediction as a function of \hat{c} and the measured \hat{c} has been observed. Even though the deviation is small ($1.6\sigma_{\text{stat}}$), it might mean that \hat{c} is not only fixed by the branching ratio (purely statistics), but also by the spectrum shape, which would mean that there is perhaps some non-negligible missing contribution in the theory. Within the scope of this thesis, $\eta - \eta'$ mixing effects appearing in $O(p^4)$ of the ChPT description of $K^\pm \rightarrow \pi^\pm \gamma \gamma$ decays have also been measured, obtaining a result for the ratio of the effective weak-coupling constants G_8^s and G_8 of $G_8^s/G_8 = 0.03 \pm 0.30$. The value of this ratio is not predicted by the theory and must be determined experimentally.

13.2 Outlook

The presented results are based on only about 20% of the available NA48/2 data from the years 2003 and 2004. This reduced data sample contained already about 30 times more $K^\pm \rightarrow \pi^\pm \gamma \gamma$ decays than ever collected. Using all data collected by the NA48/2 would not only reduce the statistical uncertainty of the branching ratio measurement, but also help to reduce the systematic uncertainties arising from the trigger. The use of the full statistics would also provide more sensitivity to test the importance of the pole contributions and $\eta - \eta'$ mixing effects in the theory.

List of Figures

3.1	Octet of pseudoscalar lightest mesons	9
3.2	Loop diagrams contributing to $O(p^4)$ ChPT for $K^\pm \rightarrow \pi^\pm \gamma \gamma$	13
3.3	One-loop function $F(z/r_\pi^2)$	14
3.4	$O(p^4)$ loop contributions to $K^\pm \rightarrow \pi^\pm \gamma \gamma$ differential decay rate	15
3.5	Pole and tadpole contributions	16
3.6	Poles contribution to $K^\pm \rightarrow \pi^\pm \gamma \gamma$ differential decay rate	18
3.7	Effect of $O(p^6)$ ChPT corrections on $K^\pm \rightarrow \pi^\pm \gamma \gamma$ spectrum	21
3.8	Effect of $O(p^6)$ ChPT corrections on $K^\pm \rightarrow \pi^\pm \gamma \gamma$ branching ratio	22
4.1	NA48/2 beam line	24
4.2	NA48 detector	27
4.3	Magnetic spectrometer	29
4.4	Hodoscope for charged particles	31
4.5	Section of liquid krypton calorimeter	32
4.6	Ribbon electrodes of liquid krypton calorimeter	33
4.7	Hodoscope for electromagnetic showers	35
4.8	Hadron calorimeter	36
5.1	Scheme of NA48/2 level 1 and level 2 triggers	42
5.2	Level 2 charged trigger	44
5.3	Neutral trigger	46
6.1	m_{fake} distribution for different Monte Carlo decay channels	52
6.2	m_{fake} vs. $m_{\gamma\gamma}$ for different Monte Carlo decay channels	53
6.3	Variables involved in the m_{fake} calculation by the trigger	54
8.1	Track momentum	64
8.2	E/p distribution	65
8.3	Location of dead cells in LKr calorimeter	66
8.4	Cluster energy vs. cluster distance to pion at LKr	67
8.5	Time difference between pion and photon candidates	68
8.6	Energy of photon candidates	68
8.7	Scheme of COG calculation	70
8.8	Background from $K^\pm \rightarrow \pi^\pm \pi^0 \pi^0$	73
8.9	Background from $K^\pm \rightarrow \pi^\pm \pi^0 \gamma$	73
8.10	COG distribution	74

8.11	Difference between charged and neutral vertex	75
8.12	Shower width at LKr vs. cluster energy	76
8.13	Invariant mass of pre-selected and selected $K^\pm \rightarrow \pi^\pm \gamma \gamma$ events	82
8.14	Invariant mass of pre-selected and selected $K^\pm \rightarrow \pi^\pm \pi^0$ events	83
8.15	Invariant mass of selected $K^\pm \rightarrow \pi^\pm \gamma \gamma$ events	84
8.16	Di-photon invariant mass of selected $K^\pm \rightarrow \pi^\pm \gamma \gamma$ events	84
8.17	Invariant mass of selected $K^\pm \rightarrow \pi^\pm \pi^0$ events	85
8.18	Di-photon invariant mass of selected $K^\pm \rightarrow \pi^\pm \pi^0$ events	85
9.1	Three-cluster event as seen by the NTPEAK trigger	91
9.2	Signal NTPEAK trigger efficiency vs. $\max(d_x^{min}, d_y^{min})$	92
9.3	Signal NTPEAK trigger efficiency vs. d_x^{min}	93
9.4	Signal NTPEAK trigger efficiency vs. pion energy	94
9.5	Signal NTPEAK trigger efficiency vs. $z = m_{\gamma\gamma}^2/m_K^2$	94
9.6	Signal Q1 trigger efficiency vs. pion energy	95
9.7	Signal LKrmbias trigger efficiency vs. photon energy	96
9.8	Signal MFAKE trigger efficiency vs. E_π and z -vertex	98
9.9	Signal MFAKE trigger efficiency vs. r_π^{DCH1} and $z = m_{\gamma\gamma}^2/m_K^2$	99
9.10	Normalization NTPEAK trigger efficiency vs. pion energy	100
10.1	$m_{\pi\gamma\gamma}$ and $m_{\gamma\gamma}$ signal data/MC comparison	104
10.2	E_π and E_γ signal data/MC comparison	105
10.3	z_{vertex} and $d_{\pi-\gamma}$ signal data/MC comparison	106
10.4	$m_{\pi\gamma\gamma}$ and $m_{\gamma\gamma}$ normalization data/MC comparison	107
10.5	E_π and E_γ normalization data/MC comparison	108
10.6	z_{vertex} and $d_{\pi-\gamma}$ normalization data/MC comparison	109
11.1	Remaining $K^\pm \rightarrow \pi^\pm \pi^0 \gamma$ IB background	115
11.2	$m_{\pi\gamma\gamma}$ for signal candidates and remaining background	115
11.3	Signal acceptance as a function of $z = m_{\gamma\gamma}^2/m_K^2$	117
11.4	Signal efficiency as a function of $z = m_{\gamma\gamma}^2/m_K^2$	118
11.5	$z = m_{\gamma\gamma}^2/m_K^2$ for signal candidates and remaining background	119
11.6	$\Delta(\text{BR})$ as a function of $z = m_{\gamma\gamma}^2/m_K^2$	121
11.7	$\text{BR}(K^\pm \rightarrow \pi^\pm \gamma \gamma)$ vs. $d_{\pi-\gamma}^{min}$, $(E/p)^{max}$, z_{vertex}^{max} and E_π^{min}	123
11.8	$\text{BR}(K^\pm \rightarrow \pi^\pm \gamma \gamma)$ vs. E_γ^{min} and LKr energy scale	124
11.9	Systematics from the efficiency measurement	125
12.1	Radiative corrections	130
12.2	Fit of $O(p^6)$ ChPT to data	131
12.3	Systematic uncertainty on \hat{c}	132
12.4	Fit of $O(p^6)$ ChPT with poles to data	133
12.5	$O(p^6)$ ChPT prediction of the $z = m_{\gamma\gamma}^2/m_K^2$ spectrum for $\hat{c} = 1.54$	135

List of Tables

3.1	Quarks of the Standard Model	7
3.2	Leptons of the Standard Model	7
6.1	Data volume collected during 2003	49
6.2	Level 1 trigger supervisor bits in 2003	51
6.3	Level 2 trigger word configuration in 2003	51
8.1	Background channels with a $K^\pm \rightarrow \pi^\pm \gamma \gamma$ -signature	72
8.2	Parameters of the fit to the maximum single shower width	76
8.3	Corrections summary	78
8.4	Selected $K^\pm \rightarrow \pi^\pm \gamma \gamma$ and $K^\pm \rightarrow \pi^\pm \pi^0$ candidates	86
8.5	Summary of selection criteria	86
8.6	$K^\pm \rightarrow \pi^\pm \gamma \gamma$ and $K^\pm \rightarrow \pi^\pm \pi^0$ events after each selection cut	87
8.7	Simulated background events events after each selection cut	88
9.1	Summary of signal trigger efficiencies	101
9.2	Total efficiencies for signal and normalization channels	101
11.1	Flux measurement	112
11.2	Estimated background	114
11.3	$K^\pm \rightarrow \pi^\pm \gamma \gamma$ Branching fraction vs. $z = m_{\gamma\gamma}^2/m_K^2$	121
11.4	MFAKE efficiency for different binnings	126
11.5	Flux measurement with CPRE trigger	126
11.6	Summary of systematic uncertainties	128
11.7	Summary of statistical uncertainties	128
12.1	Constants used for $O(p^6)$ ChPT fit	131
12.2	Additional fit constants	134

Bibliography

- [1] E. Abouzaid *et al.* Final results from the KTeV Experiment on the Decay $K_L \rightarrow \pi^0 \gamma \gamma$. *Phys. Rev. D*, 77:112004, 2008.
- [2] I. V. Ajinenko *et al.* Measurement of the Dalitz plot slope parameters for $K^- \rightarrow \pi^0 \pi^0 \pi^-$ decay using ISTRA+ detector. *Phys. Lett. B*, 567:159, 2003.
- [3] F. Ambrosino *et al.* Measurement of the eta mass at KLOE. *arXiv:0707.4616v1*, 2007.
- [4] F. Ambrosino *et al.* Measurement of the absolute branching ratio of the $K^+ \rightarrow \pi^+ \pi^0 (\gamma)$ decay with the KLOE detector. *arXiv:0804.4577v1*, 2008.
- [5] S. Anvar *et al.* The charged trigger system of NA48 at CERN. *Nucl. Instr. Meth. A*, 419:686, 2003.
- [6] GEANT Application Software Group. Geant, Detector description and simulation tool. *CN Division, CERN*, 1994.
- [7] R. Arcidiacono *et al.* A note on the NA48 Trigger Supervisors and their interconnections. *NA48 Note 97-32*, 1997.
- [8] R. Arcidiacono *et al.* The Level 1 Trigger Supervisor: past, present and future. *NA48 Note 98-11*, 1998.
- [9] A.V. Artamonov *et al.* Search for the decay $K^+ \rightarrow \pi^+ \gamma \gamma$ in the π^+ momentum region $P > 213 \text{ MeV}/c$. *Phys. Lett. B*, 623:192, 2005.
- [10] H. W. Atherton *et al.* Precise measurements of particle production by 400 GeV/c protons on beryllium targets. *CERN 80-07 Super Proton Synchrotron Division*, 1980.
- [11] I. Augustin *et al.* A Reconstruction Program for Charged Decays based on Space Points. *NA48 Note 97-11*, 1997.
- [12] I. Augustin *et al.* The drift chamber electronics and readout for the NA48 experiment at the CERN SPS. *Nucl. Instr. Meth. A*, 403:472, 1998.
- [13] C. Avanzini *et al.* The peaksum processing system for the NA48 experiment. a VLSI based processor. *IEEE Trans. Nucl. Sci.*, 43:1789, 1996.

- [14] G. D. Barr *et al.* A measurement of the decay $K_L \rightarrow \pi^0 \gamma \gamma$. *Phys. Lett. B*, 284:440, 1992.
- [15] G.D. Barr *et al.* A Fully Software-programmable Pipelined Trigger-processing Module. *NA48 Note 95-32*, 1995.
- [16] G.D. Barr *et al.* Performance of an electromagnetic liquid krypton calorimeter based on a ribbon electrode tower structure. *Nucl. Instr. Meth. A*, 370:413, 1996.
- [17] J. R. Batley *et al.* A high sensitivity investigation of K(S) and neutral Hyperon decays using a modified K(S) beam. (Addendum 2 to P253). *CERN-SPSC-P-253-ADD-2*, 1999.
- [18] J. R. Batley *et al.* Precision measurement of charged kaon decay parameters with an extended NA48 setup. (Addendum 3 to proposal P253/CERN/SPSC). *CERN-SPSC-P-253-ADD-3*, 1999.
- [19] J. R. Batley *et al.* A precision measurement of direct CP violation in the decay of neutral kaons into two pions. *Phys. Lett. B*, 544:97, 2002.
- [20] J. R. Batley *et al.* Observation of a cusp-like structure in the $\pi^0 \pi^0$ invariant mass distribution from $K^+ \rightarrow \pi^+ \pi^0 \pi^0$ decay and determination of the $\pi \pi$ scattering lengths. *Phys. Lett. B*, 633:173, 2006.
- [21] J. R. Batley *et al.* Search for direct CP violation in the decays $K^\pm \rightarrow 3\pi^\pm$. *Phys. Lett. B*, 634:474, 2006.
- [22] J. R. Batley *et al.* First Observation and Measurement of the Decay $K^\pm \rightarrow \pi^\pm e^+ e^- \gamma$. *Phys. Lett. B*, 659:493, 2008.
- [23] D. Bederede *et al.* High resolution drift chambers for the NA48 experiment at CERN. *Nucl. Instr. Meth. A*, 367:88, 1995.
- [24] A. Bevan and B. Hay. Efficiency of the Muon Veto System. *NA48 Note 98-17*, 1998.
- [25] C. Biino *et al.* Compact 7.2 user guide. *NA48 Documentation*, 2005.
- [26] C. Bruno and J. Prades. Rare kaon decays in the $1/N_c$ -expansion. *Z Phys. C*, 57:585, 1993.
- [27] L. Cappiello, G. D'Ambrosio, and M. Miragliuolo. Corrections to $K \rightarrow \pi \gamma \gamma$ from $K \rightarrow 3\pi$. *Phys. Lett. B*, 298:423, 1993.
- [28] D. C. Carey. Turtle, A computer program for simulating charged particle beam transport systems. *Fermilab National Accelerator Library*, FERMILAB-NAL-64 2041.000, 1971.

-
- [29] P. Cenci *et al.* The fast logic of charged and neutral hodoscopes. *NA48 Note 97-25*, 1997.
- [30] H.Y. Cheng. Large- N_c higher-order weak chiral lagrangians coupled to external electromagnetic fields: Applications to radiative kaon decays. *Phys. Rev. D*, 42:72, 1990.
- [31] J. B. Chèze. NA48 Spectrometer: Vertex calculation. *NA48 Note 02-02*, 2002.
- [32] N. Christ. Possible CP violation in $K^\pm \rightarrow \pi^\pm \pi^0 \gamma$. *Phys. Rev.*, 159:1292, 1967.
- [33] M. Cirilli. Neutral Trigger System - User'Guide. *NA48 Note 02-04*, 2002.
- [34] A. G. Cohen, G. Ecker, and A. Pich. Unitarity and $K_L \rightarrow \pi^0 \gamma \gamma$. *Phys. Lett. B*, 304:347, 1993.
- [35] NA48 Collaboration. <http://NA48.web.cern.ch/NA48/welcome/images/pictures.html>. 1998.
- [36] NA48 Collaboration. Status report on experiment NA48/2. *CERN-SPSC-2003-033, SPSC-M-707*, 2003.
- [37] G. D'Ambrosio and J. Portolés. Unitarity and vector meson contributions to $K^+ \rightarrow \pi^+ \gamma \gamma$. *Phys. Lett. B*, 386:403, 1996.
- [38] G. D'Ambrosio and J. Portolés. Vector meson exchange contributions to $K \rightarrow \pi \gamma \gamma$ and $K_L \rightarrow \gamma l^+ l^-$. *Nucl. Phys. B*, 492:417, 1997. Erratum *Ibid.* 395:390.
- [39] M. De Beer and F. Derue. NASIM User's Guide. *NA48 Note 00-23*, 2000.
- [40] T. J. Devlin and J. O. Dickey. Weak hadronic decays: $K \rightarrow 2\pi$ and $K \rightarrow 3\pi$. *Rev. Mod. Phys.*, 51:237, 1979.
- [41] L. di Lella. Alignments and corrections to the momenta. NA48 Charged Kaons Meeting, 2003.
- [42] J. F. Donoghue, E. Golowich, and B. R. Holstein. *Dynamics of the Standard Model*. Cambridge Monographs on Particle Physics, Nuclear Physics and Cosmology, 1994.
- [43] G. Ecker. Chiral Perturbation Theory. *Prog. Part. Nucl. Phys.*, 35:1, 1995.
- [44] G. Ecker, J. Kambor, and D. Wyler. Resonances in the weak chiral lagrangian. *Nucl. Phys. B*, 394:101, 1993.

- [45] G. Ecker, A. Pich, and E. de Rafael. $K^0 \rightarrow \pi^0 \gamma \gamma$ decays in chiral perturbation theory. *Phys. Lett. B*, 189:363, 1987.
- [46] G. Ecker, A. Pich, and E. de Rafael. $K \rightarrow \pi l^\pm l^\mp$ decays in the effective chiral lagrangian of the standard model. *Nucl. Phys. B*, 291:692, 1987.
- [47] G. Ecker, A. Pich, and E. de Rafael. Radiative kaon decays and CP Violation in ChPT. *Nucl. Phys. B*, 303:665, 1988.
- [48] G. Ecker, A. Pich, and E. de Rafael. Vector meson exchange in radiative kaon decays and chiral perturbation theory. *Phys. Lett. B*, 237:481, 1990.
- [49] G. Esposito-Farese. Right invariant metrics on SU(3) and one loop divergences in chiral perturbation theory. *Z Phys. C*, 50:255, 1991.
- [50] V. Fanti *et al.* The beam and detector for the NA48 neutral kaon CP violation experiment at CERN. *Nucl. Instr. Meth. A*, 574:433, 2007.
- [51] L. Fiorini. *New precise measurements of the ratio of leptonic decays of K^+ and K^- mesons.* PhD thesis, Pisa, 2005.
- [52] G. Fischer *et al.* A 40-MHz-pipelined trigger for $K^\pm \rightarrow 2\pi^0$ decays for the CERN NA48 experiment. *Nucl. Instr. Meth.*, page 695, 1998.
- [53] H. Fritzsch, M. Gell-Mann, and H. Leutwyler. Advantages of the color octet gluon picture. *Phys. Lett. B*, 47:365, 1973.
- [54] M. K. Gaillard, P. D. Grannis, and F. K. Sciulli. The standard model of particle physics. *Rev. Mod. Phys.*, 71:596, 1999.
- [55] J. Gasser and H. Leutwyler. Chiral perturbation theory: Expansions in the mass of the strange quark. *Nucl. Phys. B*, 250:465, 1984.
- [56] J. Gasser and H. Leutwyler. Chiral perturbation theory to one loop. *Annals Phys.*, 158:142, 1984.
- [57] M. Gell-Mann. A schematic model of baryons and mesons. *Phys. Lett. B*, 8:214, 1964.
- [58] J. M. Gérard and E. Kou. $\eta - \eta'$ masses and mixing: A Large N_c reappraisal. *Nucl. Phys. B*, 616:85, 2005.
- [59] J. M. Gérard, C. Smith, and S. Trine. Private communication.
- [60] J. M. Gérard, C. Smith, and S. Trine. Radiative Kaon Decays and the Penguin Contribution to the Delta I = 1/2 Rule. *Nucl. Phys. B*, 730:1, 2005.

-
- [61] M. Gersabeck. Messung der Verzweigungsverhältnisse und der Formfaktoren im Zerfall $K^\pm \rightarrow \pi^0 \pi^0 e^\pm \nu_e$ mit dem NA48/2-Detektor. Master's thesis, 2006.
- [62] S. L. Glashow. Partial symmetries of weak interactions. *Nucl. Phys.*, 22:579, 1961.
- [63] J. Goldstone. Field theories with superconductor solutions. *Nuovo Cim.*, 19:154, 1961.
- [64] J. Goldstone, A. Salam, and S. Weinberg. Broken symmetries. *Phys. Rev.*, 127:965, 1962.
- [65] P. Golonka and Z. Was. PHOTOS Monte Carlo: A precision tool for QED corrections in Z and W decays. *Eur. Phys. J. C.*, 45:97, 2006.
- [66] S. Goy López. B field in the blue tube. Talk at NA48/2 collaboration meeting. 02.04.2003.
- [67] S. Goy López. *Study of the $K^\pm \rightarrow \pi^\pm \pi^0 \gamma$ decays at the NA48/2 experiment at the CERN SPS*. PhD thesis, Torino University and Paris XI Orsay, 2006.
- [68] D. J. Griffiths. *Introduction to elementary particles*. Wiley, J. and Sons, 1987.
- [69] D. J. Gross and F. Wilczek. Asymptotically free gauge theories. 1. *Phys. Rev. D*, 8:3633, 1973.
- [70] D. J. Gross and F. Wilczek. Asymptotically free gauge theories. 2. *Phys. Rev. D*, 9:980, 1974.
- [71] NA48 Mainz Group. </afs/physik.uni-mainz.de/home/NA48sw/detektor>. 2001.
- [72] NA48 Perugia, Mainz group. A Proposal for a Neutral Hodoscope in NA48. *NA48 Note 94-18*, 1994.
- [73] NA48 Torino group. NA48 Anticounters: Design, Construction, Installation and 93-94 Test Beam. *NA48 Note 96-3*, 1996.
- [74] F. Halzen and A. D. Martin. *Quarks and Leptons*. John Wiley and sons., 1984.
- [75] P. W. Higgs. Broken symmetries and the masses of gauge bosons. *Phys. Rev. Lett.*, 13:508, 1964.
- [76] P. W. Higgs. Broken Symmetries, Massless Particles and Gauge Fields. *Phys. Lett.*, 12:132, 1964.

- [77] F. James. Monte Carlo Phase Space. *CERN 68-15*, 1968.
- [78] M. Jeitler. The NA48 liquid-krypton calorimeter. *Nucl. Instr. Meth. A*, 494:373, 2002.
- [79] A. Kalter. Bau eines Hodoskops aus szintillierenden Fasern für das NA48 Experiment und Messung mit einem Prototypen. Master's thesis, Mainz, 1998.
- [80] J. Kambor, J. Missimer, and D. Wyler. The chiral loop expansion of the nonleptonic weak interactions of mesons. *Nucl. Phys. B*, 346:17, 1990.
- [81] J. Kambor, J. Missimer, and D. Wyler. $K \rightarrow 2\pi$ and $K \rightarrow 3\pi$ Decays in next-to-leading order chiral perturbation theory. *Phys. Lett. B*, 261:496, 1991.
- [82] P. Kitching *et al.* Observation of the decay $K^+ \rightarrow \pi^+ \gamma \gamma$. *Phys. Rev. Lett.*, 79:4079, 1997.
- [83] K. Kleinknecht. *Detektoren für Teilchenstrahlung*. Teubner Stuttgart, 1987.
- [84] A. Lai and L. Musa. Pipeline Memory Board Specs. *NA48 Note 95-5*, 1995.
- [85] A. Lai *et al.* A precise measurement of the direct CP violation parameter $Re\epsilon_c$. *Eur. Phys. J. C*, 22:231, 2001.
- [86] A. Lai *et al.* Precise measurement of the decay $K_L \rightarrow \pi^0 \gamma \gamma$. *Phys. Lett. B*, 536:229, 2002.
- [87] H. Leutwyler. On the foundations of chiral perturbation theory. *Ann. Phys.*, 235:165, 1994.
- [88] P. Lubrano *et al.* A proposal for a neutral hodoscope in NA48. *NA48 Note 94-18*, 1994.
- [89] L. Maiani and N. Paver. *CP conserving nonleptonic $K \rightarrow 3\pi$ decays*, volume 1. The Second DAPHNE physics handbook, 1997.
- [90] A. V. Manohar and H. Georgi. Chiral quarks and the nonrelativistic quark model. *Nucl. Phys. B*, 234:189, 1984.
- [91] V. Papadimitriou *et al.* Measurement of the branching ratio of the decay $K_L \rightarrow \pi^0 \gamma \gamma$. *Phys. Rev. D*, 44:573, 1991.
- [92] D. H. Perkins. *Introduction to High Energy Physics*. Addison-Wesley, Inc., 1987.

-
- [93] E. Peskin and D. V. Schroeder. *An introduction to quantum field theory*. Preseus Books, Cambridge, MA, 1995.
- [94] B. Peyaud. KABES: A novel beam spectrometer for NA48, 2004.
- [95] A. Pich. Chiral Perturbation Theory. *Rept. Prog. Phys.*, 58:563, 1995.
- [96] H. D. Politzer. Asymptotic freedom: An approach to strong interactions. *Phys. Rept.*, 14:129, 1974.
- [97] M. Raggi. Highlights on rare kaon decays. *Nucl. Phys. B*, 167:39, 2007.
- [98] A. Salam and D. C. Ward. Electromagnetic and weak interactions. *Phys. Lett.*, 13:168, 1964.
- [99] S. Scherer. Introduction to Chiral Perturbation Theory. *Adv. Nucl. Phys.*, 27:277, 2003.
- [100] S. Scherer and M. R. Schindler. A chiral perturbation theory primer. *hep-ph/0505265*.
- [101] G. Unal. Neutral reconstruction. *NA48 Note 95-10*, 1995.
- [102] G. Unal. Reconstruction program for the LKr. *NA48 Note 98-1*, 1997.
- [103] S. Weinberg. A model of leptons. *Phys. Rev. Lett.*, 19:1264, 1967.
- [104] S. Weinberg. Phenomenological Lagrangians. *Physics A*, 96:327, 1979.
- [105] J. Wess and B. Zumino. Consequences of anomalous ward identities. *Physics Letters B*, 37:95, 1971.
- [106] E. Witten. Global aspects of current algebra. *Nucl. Phys. B*, 223:422, 1983.
- [107] M. Wittgen *et al.* The NA48 event building PC farm. *IEEE Trans. Nucl. Sci.*, 47:348, 2000.
- [108] W.-M. Yao *et al.* Review of particle physics. *J. Phys. G*, 33:1, 2006.
- [109] C. Zemach. Three pion decays of unstable particles. *Phys. Rev. B*, 133:1201, 1964.
- [110] G. Zweig. An SU(3) model for strong interaction symmetry and its breaking. 2. *CERN-TH 412*, 1964.

